INVESTIGATION OF ACUROS XB RADIOTHERAPY DOSE CALCULATION ALGORITHM

Andrew McGrath

THE UNIVERSITY of ADELAIDE

Thesis submitted for the degree of

Master of Philosophy

School of Physical Sciences

University of Adelaide

Australia

June, 2018

CONTENTS

Abbreviations

AAA Anisotropic Analytical Algorithm

ACDS Australian Clinical Dosimetry Service

CCC Collapsed Cone Convolution

CT Computed Tomography

DBS Directional Bremsstrahlung Splitting

DVH Dose Volume Histogram

FWHM Full-width at Half-Maximum

ICF Inhomogeneity Correction Function

IMRT Intensity Modulated Radiation Therapy

KERMA Kinetic Energy Released per unit Mass

LBTE Linear Boltzmann Transport Equation

MC Monte Carlo

MLC Multi-leaf Collimator

OAR Organ at Risk

PDD Percentage Depth Dose

PTV Planning Target Volume

ROI Region of Interest

RTAR Ratio of Tissue to Air

SBRT Stereotactic Body Radiation Therapy

SSD Source to Surface Distance

TERMA Total Energy Released per unit Mass

TLD Thermoluminescent Dosimeter

TPS Treatment Planning System

VMAT Volumetric Modulated Arc Therapy

Abstract

An important part of the radiotherapy process is the calculation of radiation dose deposition for individual patients. Accurate dose calculation provides a foundation for accurate dose prescription and reporting in radiation therapy. Several classes of radiation dose calculation algorithms exist. Some commonly used superposition-convolution algorithms are Collapsed Cone Convolution (CCC) (Philips Radiation Oncology Systems, Fitchburg, WI) and Anisotropic Analytical Algorithm (AAA) (Varian Medical Systems, Palo Alto, CA, USA). Recently, Varian has introduced a new algorithm, Acuros XB, which solves the Linear Boltzmann Transport Equation (LBTE). This study assesses the accuracy of dose calculations performed with Acuros.

In this study, a Monte Carlo model was created using the EGSnrc family of Monte Carlo code, in order to run Monte Carlo simulations. A Monte Carlo simulation involves simulating particle transport directly and is considered to be the gold standard in radiotherapy dose calculations. The Monte Carlo model is used to assess the accuracy of Acuros XB.

In simple slab geometry, Acuros XB outperforms AAA when compared to Monte Carlo calculations and to measurements. Acuros XB and AAA show a difference of -0.06 $\pm$ 0.13% and +0.6 $\pm$ 0.18% respectively, compared to measured doses distal to lung slabs of various thicknesses.

Tests described in TecDoc 1583 [Vatnitsky and International Atomic Energy Agency, 2008] were used to validate Acuros and AAA calculations on a simple anthropomorphic phantom. Averaged over all TecDoc 1583 test cases and measurement points, AAA calculated dose 0.4 $\pm$ 0.4% higher than measured, while Acuros calculated dose 0.2 $\pm$ 0.2% lower than measured.

Calculations were made with Acuros, AAA and CCC for plans with small fields on Computed Tomography (CT) image sets of SBRT patients. The calculations were compared with Monte Carlo calculated dose. Acuros showed marginally better agreement with Monte Carlo than the other algorithms, for the patient plans and datasets used in this study. For a slice through the target volume of each plan, Acuros, AAA and CCC had a 98.0%, 97.8% and 96.7% gamma metric pass rate compared to Monte Carlo calculated dose, using the 2%, 2 mm gamma criteria.

Declaration

I certify that this work contains no material which has been accepted for the award of any other degree or diploma in my name, in any university or other tertiary institution and, to the best of my knowledge and belief, contains no material previously published or written by another person, except where due reference has been made in the text. In addition, I certify that no part of this work will, in the future, be used in a submission in my name, for any other degree or diploma in any university or other tertiary institution without the prior approval of the University of Adelaide and where applicable, any partner institution responsible for the joint-award of this degree.

I give consent to this copy of my thesis, when deposited in the University Library, being made available for loan and photocopying, subject to the provisions of the Copyright Act 1968.

I also give permission for the digital version of my thesis to be made available on the web, via the University's digital research repository, the Library Search and also through web search engines, unless permission has been granted by the University to restrict access for a period of time.

Andrew McGrath

22/01/18

Acknowledgements

I am extremely grateful for the invaluable assistance, feedback and guidance provided by my project supervisors: Dr. Steven Wallace, Dr. Scott Penfold and Dr. Judith Pollard.

I would like to thank Tim Williams for being an endless source of knowledge and expertise in all things.

Thanks to Bronwyn Hilder at the Royal Hobart Hospital for providing support for the procurement of equipment required in this study.

Finally, I would like to thank my family, especially my wonderful partner Tanikah, for their constant support, thorough proofreading and unwavering patience.

1. INTRODUCTION

The lifetime risk of a person developing cancer is approximately 40% [Lag *et al.*, 1975]. Radiotherapy is an important asset in the management and treatment of many types of cancer; it is utilised in about 50% of all cancer treatments [Baskar *et al.*, 2012]. Radiotherapy is the delivery of one or more beams of radiation to the site of the disease, with the intent of reducing or destroying the disease volume. Radiation destroys cancer cells directly via the interaction of ionising radiation with molecules in DNA, or indirectly by the creation of free radicals, causing DNA damage through subsequent chemical processes. Damage to normal tissue outside of the disease volume is minimised through the careful selection of radiation field shape and size, beam energy, beam angle and attenuators such as a compensator or multi-leaf collimator.

Damage to tissue correlates with radiation dose received by that tissue. Dose is defined as the energy absorbed per unit mass in a medium,

$$D = E_{abs}/m. \tag{1.1}$$

Dose has the units of Gray (Gy), where 1 Gy = 1 J/kg. In radiation therapy photon beams, dose is deposited in a two step process. Photons give energy to charged particles in a medium through the photoelectric effect, Compton scatter or pair production. For photons with energies that are typically used in megavoltage radiation therapy, Compton scatter is by far the most common interaction. The incident energy that is given to charged particles by photons entering the patient is called KERMA (Kinetic Energy Released per unit Mass). The resulting energetic charged particles, primarily electrons, deposit energy through Coulomb interactions. Under electronic equilibrium, where the number of electrons entering a region is the same as the number leaving, the dose is related simply to the KERMA through the equation

$$D = K(1 - g), \tag{1.2}$$

where K is the kerma and g is the fraction of energy lost due to bremsstrahlung production. When electronic equilibrium does not exist, this simple relationship does not apply. Regions where electronic equilibrium does not exist could be in small radiation beams, at the interface between different tissues and in low-density tissue such as lung.

A radiotherapy treatment is a multi-step process. After diagnosis and staging, a planning CT scan is taken and the radiation oncologist delineates the gross target volume (GTV). An expansion of the GTV for sub-clinical spread results in the clinical target volume (CTV). An expansion of the CTV to include geometric and setup uncertainties results in the planning target volume (PTV). A dose prescription is given to PTV by the radiation oncologist, with dose limits for organs at risk (OAR). A plan is then developed for the treatment. The treatment plan describes the arrangement and weighting of all radiation beams to be delivered to the patient. Dose calculation is performed in order to assess the suitability of the treatment and any associated risks, and is reviewed by the radiation oncologist before treatment commences. Treatment is delivered in multiple fractions, over a time period from a few days up to 6-8 weeks. Each treatment delivery is guided by planar or volumetric image matching to ensure that each fraction is delivered as planned.

Dose calculation is a vital part of the radiotherapy treatment process. Van Dyk [1999] summarises this by noting, 'the dose calculation algorithm is the most unique, critical, and complex piece of software in a computerized planning system'. Historically, dose calculation was performed with a manual calculation based on simple geometry or patient contours. As computer hardware and technology advanced, dose calculation shifted to implementation by algorithms run on computers.

An overall accuracy of better than 5% in all stages of treatment delivery is generally desired with achievable accuracy expected to increase as technology advances [Papanikolaou *et al.*, 2004]. Each individual step in the treatment process, including dose calculation, should contribute the smallest possible uncertainty. Increasing the accuracy of dose calculation will result in a few key improvements:

1. Lower uncertainties in clinical trials - fewer patients are required for the same

statistical significance achieved.

2. The therapeutic ratio can be increased by allowing dose escalation, such as in hypofractionated or stereotactic treatment regimes.

Boyer and Schultheiss [1988] calculated that the cure rate of early stage patients increases by 2% for a 1% improvement in dose accuracy. Since optimisation techniques rely heavily on dose calculation, optimisers can be improved through better dose calculation algorithms, hence increasing the therapeutic ratio.

The introduction of a new dose calculation algorithm for clinical use requires careful validation to ensure that the calculated dose matches actual dose under a variety of conditions. The aim of this thesis is to investigate the accuracy of a new type of dose calculation algorithm, Acuros XB, under various conditions, including small fields with heterogeneities.

Chapter 2 reviews dose calculation methods including some of the limitations of current methods. Chapter 2 introduces Acuros XB and presents a review of work already undertaken in the literature to validate its use clinically.

A detailed discussion of Monte Carlo dose calculation is given in Chapter 3, including a review of the codes used in this study and a discussion of the variance reduction techniques used to decrease calculation times. Chapter 3 also details the process of modelling a linear accelerator in BEAMnrc for dose calculation purposes.

Chapter 4 provides a detailed discussion of the commercial dose calculation algorithms that have been compared to Acuros XB. Chapter 4 also describes the process of optimising the beam model for AAA and Acuros XB as well as simple verifications of the beam model.

The accuracy of Acuros XB and the other commercial dose calculation algorithms under various conditions is examined in Chapter 5. The calculations made using these algorithms are compared to Monte Carlo calculations and to measurements.

Chapter 6 presents a discussion of the work undertaken in this thesis.

2. LITERATURE REVIEW

Radiation dose calculation can be performed with a simple equation using measured beam data. In a homogeneous phantom, the dose D to a point at depth d, and at an off-axis position x, is calculated through the equation [Gibbons *et al.*, 2014]

$$D = MU \times D'_0 \times S_c(r_c)S_p(r_{d_0}) \times PDD_N(d, r, SSD) \times WF(d, r_d, x) \times TF \times OAR(d, x) \times \left(\frac{SSD_0 + d_0}{SSD + d_0}\right)^2 \tag{2.1}$$

where D'_0 specifies the output of the machine under reference conditions, MU (Monitor Units) specifies the output of the machine during treatment, $S_c(r_c)$ and $S_p(r_{d_0})$ are the collimator and phantom scatter factors, PDD_N is the percentage depth dose curve, WF is the wedge factor, TF is the tray factor, OAR is the off-axis ratio at position x and the last term is a correction for the source-to-surface distance (SSD) being different from that of the calibration (SSD_0).

The collimator and phantom scatter terms describe the change in scatter conditions due to changing the field size from the reference field size. The Percentage Depth Dose (PDD) curve shows how dose varies with depth for a particular machine and field size. The wedge factor and tray factor account for the reduction of dose when a wedged field or attenuator are used. The off-axis-ratio describes the shape of the radiation field off-axis at depth d and position x.

This method of dose calculation is used as an approximation or verification of other calculation algorithms. For clinical assessment of dose, computational algorithms calculate dose using Computed Tomography (CT) images taken of a patient.

2.1 Heterogeneities

Heterogeneities in the context of radiotherapy dose calculations are materials in a patient or phantom that have significantly different radiological properties to water, such as lung or bone. Heterogeneities in patient geometry can be a source of large

error in dose calculations. Heterogeneities with relatively high or low densities may be handled incorrectly by many simple algorithms.

Low density materials in radiotherapy beams present a challenge for dose calculation methods. In regions distal to a low density material, dose increases relative to the case with no heterogeneities due to a decrease in photon attenuation in the low density material. Proximal to the low density interface (i.e a water-air interface), a decrease in dose occurs due to the loss of backscatter relative to water-only calculations. In low density materials the increase in lateral scatter of electrons increases electronic disequilibrium, complicating the dose calculation near the interface. This effect is exacerbated with small fields and high energy beams. For a dose calculation algorithm that does not accurately take into account this effect, an under-dosing of tissue proximal to the low density material relative to reported dose will occur [Klein *et al.*, 1993].

Methods to account for inhomogeneities are generally either correction-based (also called semi empirical) or model-based. The first calculates dose by assuming the patient is water-like and applies an inhomogeneity correction factor, typically a function $ICF(x, y, z)$. The latter calculates dose from first principles without requiring a calculation in water.

One of the simplest 1D correction methods uses effective attenuation. This method gives the correction function [Papanikolaou *et al.*, 2004] as

$$ICF = e^{\mu'(d-d')}, \tag{2.2}$$

where d' is the equivalent water depth, calculated by summing the depths above the calculation point scaled by the density of the material above it. This does not take into account any scatter variation introduced by different materials. A more accurate 1D calculation method which corrects for some scatter in one dimension is the Ratio of Tissue Air Ratios (RTAR). The Tissue to Air Ratio is defined as the ratio of dose at the isocentre at a depth d in water to the dose at the isocentre in air. The ICF for the RTAR method is given by

$$ICF = \frac{TAR(d', r_d)}{TAR(d, r_d)}, \tag{2.3}$$

where d' is the equivalent water depth as above. This correction method doesn't

take into account the position of the inhomogeneity relative to the correction point. Methods to enhance the accuracy of the RTAR method include the Power Law [Batho, 1964, Sontag, 1977, Young and Gaylord, 1970] and the Equivalent Tissue Air Ratio method.

2.2 Calculation algorithms

2.2.1 Monte Carlo

The 'gold standard'of radiotherapy dose calculation algorithms is the Monte Carlo (MC) method. Monte Carlo methods calculate dose by simulating a large number of particle interactions directly in a medium. Interactions are probabilistic and based on pre-calculated interaction cross-sections for Compton scatter, photoelectric, pair production, etc. By simulating a larger number of particles, the dose calculated by Monte Carlo methods approaches the actual absorbed dose. Increasing the number of particles in the calculation decreases the statistical uncertainty in the final dose. The main disadvantage of Monte Carlo methods is the speed of calculation; simulating such a large number of particles can be extremely time consuming. Methods exist to speed up Monte Carlo calculations at the cost of some loss of accuracy but typically in clinical situations, faster algorithms are used.

2.2.2 Superposition-convolution

Superposition-convolution algorithms are commonly used in modern radiotherapy treatment planning systems. Here the dose calculation is split into the calculation of the Total Energy Released per unit Mass (TERMA) and the scattered dose from the multiple photon interactions and electron transport. The TERMA is the total energy released in interactions of the incident photons with the material. TERMA differs from KERMA in that KERMA involves only the kinetic energy of charged particles in the medium due to interactions of the incident photons. Superposition-convolution algorithms make use of dose kernels which are pre-calculated data that describe scatter in a medium at specific particle energies. Dose kernels are typically calculated by Monte Carlo methods. Dose at a point in the medium is a result of integrating the product of TERMA and the contribution from the dose kernel over

the volume of the medium,

$$D(x,y,z) = \int\int\int T(x',y',z')K(x',y',z';x,y,z)dx'dy'dz' \tag{2.4}$$

where T is the TERMA and K is the contribution from the dose kernel originating at (x', y', z').

Corrections for inhomogeneity are made by scaling both the TERMA and the dose kernel by the density of the material. Implementations of superposition-convolution algorithms differ in their dose kernels, handling of heterogeneities and any approximations or simplifications used. Examples of different algorithms based on superposition-convolution are Varian's Anisotropic Analytical Algorithm (AAA) and Philip's Collapsed Cone Convolution Superposition algorithm (CCC). Many studies have examined the validity of both AAA and CCC in homogeneous and heterogeneous media [Aarup *et al.*, 2009, Bragg and Conway, 2006, Hasenbalg *et al.*, 2007, Rong *et al.*, 2006].

2.2.3 Acuros XB

Recently, an algorithm called Acuros XB (AXB) [Failla *et al.*, 2010, Vassiliev *et al.*, 2010] has been introduced to the Eclipse (Varian Medical Systems, Palo Alto, CA, USA) Treatment Planning System (TPS). AXB solves the Linear Boltzmann Transport Equation (LBTE), a set of equations that describes the macroscopic transport of ionising radiation. Analytical solutions to the LBTE, especially in radiotherapy, are generally not known due to the complexity of conditions. Thus, numerical methods are used to solve the LBTE, discretising in space, angle and energy. A more detailed description of the algorithm is given in Chapter 4.

Fogliata, Nicolini, Clivio, Vanetti, Mancosu and Cozzi [2011] have validated the implementation of Acuros XB in the Eclipse TPS in water for simple geometries. The study was carried out using 6 and 15 MV beams and 6 and 10 MV flattening filter free beams. Comparisons were made between AAA, AXB and measurements. Agreements for all methods were found to be within 1% for the open beams and 2% for beams when using mechanical wedges.

Using ion chamber measurements in a homogeneous phantom, Bush *et al.* [2011] found agreements better than 1.9 % with AXB for field sizes between 4 x 4 and 30

x 30 cm^2 for 6 and 18 MV beams.

Han *et al.* [2011] found agreements between Monte Carlo , AXB, AAA and CCC for PDDs calculated in a homogeneous phantom of within 1.5% for 6 MV and 2.5% for 18 MV. They found agreements between the lateral dose profiles at various depths and field sizes for the same algorithms of better than 2% for 6 MV and similar for 18 MV beams.

AXB is claimed to have similar accuracy in heterogeneous mediums as MC methods. Many studies have examined the accuracy of AXB in heterogeneous phantoms, either real or virtual. Fogliata, Nicolini, Clivio, Vanetti and Cozzi [2011*a*] looked at MC and AXB in heterogeneous phantoms for field sizes of 13 x 13 cm^2 and 2.8 x 13 cm^2 with 6 and 15 MV photon beams, finding differences corresponding to average gamma agreement (3%, 3 mm) of 100%, 86% and 100% for lung, low-density lung and bone, respectively. The gamma metric is described in detail in Appendix C.1. Bush *et al.* [2011] compared MC calculations to AXB and AAA calculations in a heterogeneous phantom simulating lung and low-density lung, finding disagreement between MC and AXB algorithms of better than 2.9% with much larger differences found between AAA and MC. On a phantom containing an air cavity, agreements between AXB and Monte Carlo calculations were found to be between 1.5 and 4.5%.

Han *et al.* [2011] compared the DOSXYZnrc MC program, AXB, AAA and CCC algorithms in a heterogeneous slab phantom made up of bone, lung and soft tissue equivalents. They compared depth doses, lateral dose profiles and overall dose difference with a 3D gamma comparison. AXB was found to have much closer agreement to MC than AAA and CCC especially at the interface regions between differing materials. In the heterogeneous phantom, the average difference in depth dose between the algorithms and Monte Carlo were 1%, 2.9% and 1.8% for AXB, AAA and CCC respectively. Mißlbeck and Kneschaurek [2012] examined PDDs and lateral profiles in two simple phantoms: slab and lung. Comparisons were made between AXB, AAA and the commercial X-ray Voxel Monte Carlo algorithm (XVMC) (Brainlab, Munich, Germany). The study showed that there was better agreement between AXB and XVMC than between AAA and XVMC.

Tsuruta *et al.* [2014] compared PDDs and dose profiles in simple lung equivalent phantoms using AAA, AXB, XVMC and measurements for field sizes from 2 x

2 cm^2 to 10 x 10 cm^2. They found good agreements between AXB, XVMC and measurements. Dose calculated with AAA was higher than measurements in the heterogeneous zone near the boundary of the lung equivalent material.

Rana and Rogers [2013*a*] compared AXB and AAA to measurements made in solid water with a varying air gap before the measurement point of between 2 - 6 cm and field sizes of 3 x 3, 5 x 5 and 10 x 10 cm. They found better agreement to measurements with AXB rather than AAA, with the biggest discrepancy found when measuring the smallest field size with the largest air gap. A repeat of this setup but with two air gaps found similar results [Rana *et al.*, 2013*b*] with both AXB and AAA underestimating dose.

Lloyd and Ansbacher [2013] examined high density implants in a water phantom, finding that AXB gave better agreements than AAA with Monte Carlo and film measurements. They also recalculated a clinical prostate plan with a hip prosthesis present with AAA, AXB and MC, finding similar results: large differences between AAA and Monte Carlo on the upstream medial surface of the prosthesis.

Ojala *et al.* [2014] performed a study comparing measurements in an anthropomorphic phantom with a unilateral hip implant (a Ti6A14V alloy) to AXB, AAA and MC model, finding excellent agreement of AXB and MC with measurements.

Dose calculations in small fields can be particularly inaccurate due to the loss of electronic equilibrium. The effects are heightened in heterogeneous mediums. Stathakis *et al.* [2012] examined the accuracy of AXB, CCC and AAA for field sizes from 1 x 1 cm^2 to 10 x 10 cm^2 in homogeneous and simple heterogeneous virtual phantoms. They found better agreement to MC with AXB and CCC than AAA. Kan *et al.* [2012] used AAA and Acuros to calculate PDDs in a heterogeneous phantom containing air cavities and compared them to measurements and MC calculations. At the air/tissue interfaces AXB overestimated dose by 6% and AAA overestimated dose by 41%.

Intensity Modulated Radiotherapy (IMRT) and Volumetric Modulated Arc Therapy (VMAT) are methods of radiation delivery that modulate each beam with Multileaf Collimators (MLCs). As a result, each field is the summation of typically many smaller fields, presenting a difficulty for dose calculation algorithms. VMAT differs from IMRT in that there are many more discrete beams in each treatment.

Han *et al.* [2012] looked at VMAT and IMRT plans on an anthropomorphic head and neck phantom, comparing AXB and AAA calculations with measured TLD and 2D film readings. The study found good agreement for both algorithms, with AXB performing only slightly better.

Han *et al.* [2013] calculated IMRT/VMAT plans on the Radiological Physics Centre thorax phantom. The study showed that AAA and AXB (dose to water) had gamma pass rates (3%, 3 mm) of 94% and 98% when compared to film measurements. The biggest differences between the AXB and AAA calculations were found at lung/soft tissue interface regions for individual IMRT fields.

Hoffmann *et al.* [2012] tested various patient plans, including IMRT and VMAT on a heterogeneous Computerised Imaging Reference System (CIRS) thorax phantom (CIRS, Norfolk, VA), finding better agreement to measured data with AXB over AAA. Kan *et al.* [2012] assessed AXB for use in nasopharyngeal carcinoma by delivering plans made to treat nasopharyngeal carcinoma to a rectangular phantom with air and bone inserts and an anthropomorphic phantom containing heterogeneous media. Measurements were made with thermoluminescent dosimeters (TLDs) and Gafchromic EBT3 film. Based on the film results, they found that compared to AAA, AXB gave only slightly better agreement with measurements in and near heterogeneous media.

Tsuruta *et al.* [2014] compared 26 lung Stereotactic Body Radiation Therapy (SBRT) plans calculated with XVMC, AAA and AXB. AXB calculation resulted in a slightly lower maximum dose in the ITV and (PTV) but with a similar dose distribution on isocentre planes in axial and sagittal views. Ojala *et al.* [2014] found good agreement in a VMAT plan using AXB and MC calculations in a CT dataset containing a high density implant. AAA was found to have larger discrepancies with MC, especially at the interface between soft tissue and implant. Acuros was successfully able to model the increased backscatter from the high-Z material.

Due to the complex structure of the mammary gland and the presence of lung tissue, inhomogeneity corrections for the treatment of breast cancers can be a difficult problem. Fogliata, Nicolini, Clivio, Vanetti and Cozzi [2011*b*] compared AAA and AXB, noting that AAA predicted, on average, 1.6% higher dose than AXB in muscle tissue. Rana and Rogers [2013*b*] found little difference between AAA and

AXB calculations in plans made on prostate cancer patient CT datasets, with AAA predicting slightly higher doses at most points. Kroon *et al.* [2013] found that, compared to AAA, using AXB resulted in $D_{98\%}$ being significantly higher in stereotactic VMAT lung plans. Liu *et al.* [2014] found no difference between mean dose in PTVs of lung SBRT patients between AXB and AAA, however the conformity of the PTV was lower in AXB than AAA. The difference in PTV conformity between the two algorithms arises from AAA overestimating dose near the edge of the heterogeneity.

Table 2.1 shows a summary of the literature as discussed above. A significant amount of verification of Acuros XB has already been performed, however studies comparing Acuros XB calculations in patient plans to full Monte Carlo (i.e EGSnrc) calculations are limited.

Tab. 2.1: Summary of literature relating to Acuros verification

Authors	Geometry	Fields	Algorithms	Measurement	Results
Fogliata, Nicolini, Clivio, Vanetti, Mancosu and Cozzi [2011]	Simple & homogeneous.	3 x 3 cm to 40 x 40 cm	AAA	Ion chamber	1 % agreement for open beams, 2 % for mechanical wedges.
Bush *et al.* [2011]	Homogeneous, lung, low-density lung, air, bone.	4 x 4 cm to 30 x 30 cm	AAA, EGSnrc	Ion chamber	Acuros agreement to MC within 2% in lung, 2.9% in low-density lung. AAA showed agreements of 10.2% and 17.5% in lung and low-density lung.
Han *et al.* [2011]	Homogeneous phantom, layered slab phantom (soft tissue, bone and lung).	2.5 x 2.5 cm, 5 x 5 cm, 10 x 10 cm	AAA, CCC, EGSnrc	None	AXB, AAA, CCC average PDD differences to MC were 1.1%, 4.4% and 2.2% respectively.
Fogliata, Nicolini, Clivio, Vanetti and Cozzi [2011*a*]	Virtual phantoms (normal lung, light lung, bone, air)	2.8 x 13 cm, 13 x 13 cm	AAA, VMC++	None	AXB & MC gamma greement (3% 3 mm) was 100%, 86% and 100% for lung, light lung and bone. AAA & MC gamma agreement (3% 3 mm) was 86%, 11%, 100%

Authors	Geometry	Fields	Algorithms	Measurement	Results
Mißlbeck and Kneschaurek [2012]	Slab phantom, 3 patient plans (lung, H&N, liver).	2.5 x 2.5 cm, 10 x 10 cm, various.	AAA, XVMC	None	AAA and XVMC showed differences of up to 13% in PDDS in lung. No differences in DVH in clinical cases.
Tsuruta *et al.* [2014]	Heterogeneous water & lung phantom, 26 SBRT lung plans	6 x 6 cm, various.	AAA, XVMC	Ion chamber for heterogeneous phantom	AXB within 3% of XVMC in SBRT plans. AAA agreement worse with the greatest difference being 4.1%.
Lloyd and Ansbacher [2013]	Water phantom with a high density volume, Clinical prostate plan with unilateral hip prosthesis.	10 x 10 cm field in water phantom, clinical prostate plan.	AAA, EGSnrc	Film	AXB performs as well as MC and better than AAA when high density materials are involved.
Rana and Rogers [2013*b*]	Inhomogeneous phantom with air gap(s).	3 x 3, 5 x 5, 10 x 10 cm	AAA	Ion chamber	AXB showed better agreement with measurement at all points, with AAA underestimating dose distal to air gap.

Authors	Geometry	Fields	Algorithms	Measurement	Results
Ojala *et al.* [2014]	Anthropomorphic phantom with Ti6A14V alloy hip implant, patient CT dataset.	8 x 10 cm, VMAT plan	AAA, EGSnrc	Ion chamber, film.	AAA produced larger discrepancies than Acuros compared to MC.
Stathakis *et al.* [2012]	Homogeneous and heterogeneous cases, two VMAT cases.	1 x 1 cm to 5 x 5 cm	AAA, CCC, EGSnrc	None	AXB comparable with MC, with improved accuracy over AAA and CCC.
Kan *et al.* [2012]	Rectangular phantom containing air cavity.	2 x 2 to 5 x 5 cm	AAA, EGSnrc	TLD	AXB overestimated dose at air/-tissue interfaces by 6% and AAA overestimated dose by 41%
Han *et al.* [2012]	Anthropomorphic head and neck phantom.	VMAT and IMRT	AAA	TLD, Film	AXB slightly better than AAA (0.1% to 3.6%) vs (0.2% to 4.6%) compared to TLD measurements
Han *et al.* [2013]	Thorax phantom.	VMAT and IMRT	AAA	TLD, Film	Differences of up to 8% between AXB and AAA were found in lung/soft tissue interface regions. AXB produced better agreement to film than AAA.

Authors	Geometry	Fields	Algorithms	Measurement	Results
Hoffman et al. [2012]	Homogeneous media, thorax phantom.	Various, including VMAT and IMRT	AAA	Film, ion chambers, diamond detector.	Better agreement to measured with AXB vs AAA.
Fogliata, Nicolini, Clivio, Vanetti and Cozzi [2011*b*]	Ten breast patients.	Breast plans	AAA	None	AAA predicted higher dose than Acuros in muscle tissue (lobular breast). Lung doses from AXB and AAA differed by 0.5 % (free breathing) to 1.5% (DIBH).
Rana *et al.* [2013*a*]	CT datasets of prostate patients.	Prostate VMAT plans	AAA	None	AAA & Acuros comparable in prostate cancer VMAT plans (highest dose difference in PTV was 0.43%).
Kroon *et al.* [2013]	CT datasets of lung VMAT patients.	Lung VMAT plans	AAA	None	AAA computed dose up to 12.3% higher in small PTVs than AXb
Liu *et al.* [2014]	77 SBRT lung CT datasets.	Lung SBRT plans	AAA	None	No statistical differences were found for mean PTV dose between the two algorithms.

3. MONTE CARLO MODEL

A typical linear accelerator operates with 2 x 10^{12} electrons per pulse. At a Pulse Repetition Frequency of 250 Hz, there will be approximately 1 x 10^{16} electrons incident on the accelerator target for a typical 2 Gy fraction. Ideal dose calculation algorithms would simulate every particle and every interaction in order to determine total energy deposition in a phantom or patient. Clearly, to fully replicate the physical processes of a linear accelerator an enormous and impractical amount of computing time is required.

Instead of simulating each and every particle interaction, a statistical approach is used; simulating a large number of incident particles can approximate linear accelerator output with good accuracy and increasing precision in a reasonable time period. The statistical approach of simulating real world processes is called the Monte Carlo method.

Monte Carlo particle transport is carried out through computer code which follows each particle through many interactions. Each interaction has a certain probability of occurring. Particle interaction probabilities and interaction results are determined through energy-dependent cross-sections. These cross-sections are well known and have been studied extensively. Thus, realistic physical interactions are simulated in Monte Carlo code.

During each photon step, Monte Carlo code would: [Metcalfe *et al.*, 2007]

1. Calculate the distance the photon moves, based on photon energy and the attenuation coefficient of the medium through which it is travelling
2. Determine which photon interaction takes place
3. Calculate the new energy and direction of travel for the photon
4. Add any particles which are created during photon interaction.

Various techniques are used to decrease statistical uncertainty for a given treat-

ment time. These are discussed in Section 3.3.1 below.

3.1 Monte Carlo codes

There are multiple Monte Carlo codes which are commonly used in radiation therapy simulations: EGSnrc, GEANT4, MCNP and PENELOPE. In this study, EGSnrc is used.

3.1.1 EGSnrc

EGS (Electron Gamma Shower) consists of code for simulating the transport of electrons and photons in various geometries with energies ranging from a few keV to several hundreds of GeV [Kawrakow and Rogers, 2000]. EGSnrc is the code upon which BEAMnrc and DOSXYZnrc are built.

EGSnrc creates particles from a source, simulates their interactions (which may or may not produce more particles) and continues this for the initial and subsequent particles until they leave the geometry, are absorbed, or are until they are culled by variance reduction techniques.

Photon interactions simulated by EGSnrc include photo-electric absorption, Rayleigh scattering, Compton scattering and pair/triplet production.

Electrons undergo a huge number of interactions while slowing down. Most of these interactions transfer no energy or a small amount of energy to the medium and so the condensed history technique [Berger, 1963] is used by EGSnrc to achieve practical computation times. The condensed history technique groups many interactions into a single step by sampling the change of the particle's energy, direction of motion, and position, at the end of the step from appropriate multiple scattering distributions [Kawrakow and Rogers, 2000].

3.1.2 BEAMnrc

BEAMnrc is a system for radiation simulation using radiotherapy sources. It uses EGSnrc for radiation transport. BEAMnrc adds various variance reduction techniques such as range rejection, bremsstrahlung splitting, photon forcing and Russian roulette. It also simplifies defining accelerator geometry by providing specific components such as slabs, cones and flattening filter geometries.

3.1.3 DOSXYZnrc

DOSXYZnrc is a system used for 3-dimensional absorbed dose calculations [Walters *et al.*, 2005]. It allows the user to define a 3-D geometry consisting of voxels of varying materials/densities in which absorbed dose is calculated. DOSXYZnrc uses EGSnrc for photon and electron transport in the volume and can use sources such as parallel or diverging beams, or BEAMnrc simulation results as input.

3.2 Modelling a Linear Accelerator

A Varian (Varian Medical Systems, Palo Alto, CA, USA) Trilogy Linear Accelerator was modelled in BEAMnrc for this study. The process of modelling a linear accelerator involves two main steps; defining the geometry of each component, and modifying the incident electron fluence to match measured beam data [Rogers *et al.*, 2009]. These two steps are described in more detail below.

3.2.1 Components

Linear accelerator components were modelled by using technical drawings from the manufacturer which specify the dimensions and materials of each component. BEAMnrc has a number of components which help to construct linear accelerator models for Monte Carlo calculations. Figure 3.1 shows the geometry of the accelerator used in this study for Monte Carlo calculations. The physical density assigned to each component in BEAMnrc greatly affects calculated dose. Sheikh-Bagheri and Rogers [2002] suggest that the density of the flattening filter and primary collimator should be known to within ± 0.1 g cm^{-3} in order to properly match off-axis ratios.

BEAMnrc has a graphical user interface (GUI) simplifying the process of defining components.

Target

The target was modelled as two thin slabs. The material used for the first slab was tungsten (W700ICRU) and the second slab was a thin slab of copper (CU700ICRU). The slabs can be considered infinite in length compared to the radius of the incident electron beam.

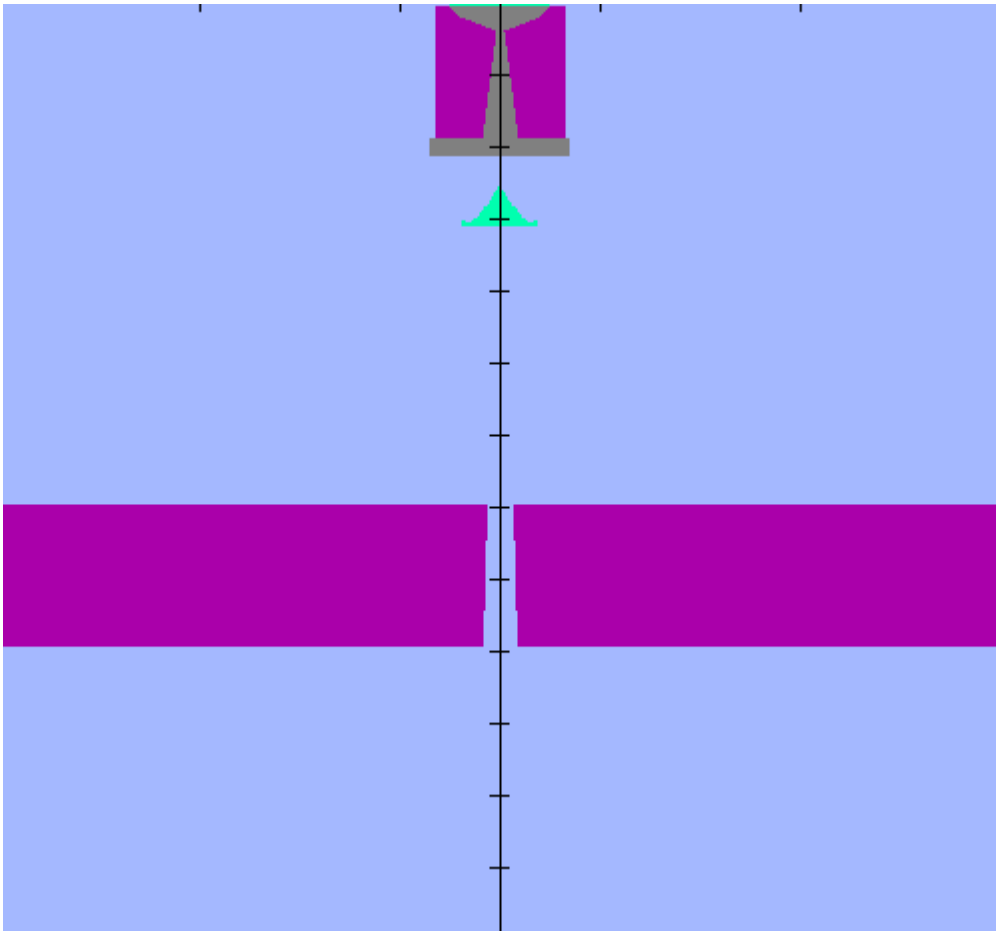

Fig. 3.1: The geometry of the linear accelerator used for Monte Carlo based dose calculations. Note that only one jaw is visible as the figure is viewed in the XY plane.

Primary collimator

The primary collimator was modelled with the CONS3R component which is a stack of truncated cones coded as three regions [Rogers *et al.*, 2009]. The radii of the top and bottom part of the primary collimator were selected to give an opening angle of 13.5 degrees, based on manufacturer drawings. Inside the primary collimator is considered a vacuum region.

Flattening filter

The flattening filter was modelled with the FLATFILT component. The FLATFILT component enabled the entry of the flattening filter geometry as layers of cones with several materials used on each layer. The flattening filter consisted of 20 layers of cones with copper selected as the material.

A linear accelerator flattening filter is designed so that the linear accelerator produces a beam that is flat as possible at 10 cm depth in water. The density of the flattening filter affects the attenuation of the beam across the flattening filter and will change the resulting intensity profile and energy distribution of the beam exiting the flattening filter. Sheikh-Bagheri and Rogers [2002] found that increasing the density of flattening filter material by 1 g cm^{-3} will increase off-axis ratios by 6%. This effect was found during the modelling of the accelerator used in this study and an example of its magnitude is shown in Figure 3.2. The flattening filter density used in this study was 9.5 g cm^{-3}.

3.2.2 Mirror and MU Chamber

The mirror was initially modelled with the BEAMnrc MIRROR component, however the dosimetric impact of including the mirror was small and so the mirror was removed in subsequent dose calculations.

The linear accelerator's MU chamber was modelled with slabs based on Varian specification. Since this thesis is not concerned with absolute dosimetry or calculating output factors, and as the dose difference calculated with and without this component was found to be small, the MU chamber was not used in subsequent dose calculations.

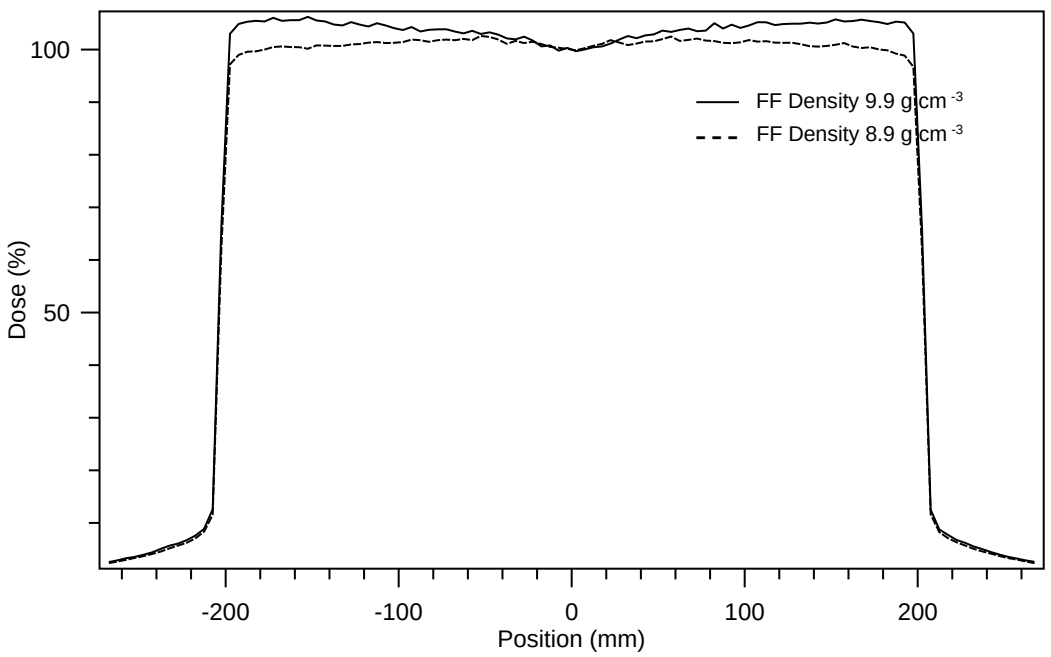

Fig. 3.2: The effect of flattening filter density on off-axis ratios. The solid profile shows the increase in off-axis-ratios for a 40 x 40 cm^2 field when a flattening filter density of 9.9 g cm^{-3} is used instead of the default density of 8.9 g cm^{-3}

The close match of the final Monte Carlo model with measured data is further justification for the removal of these two components.

Secondary collimator (X and Y Jaws)

The X and Y jaws were modelled with the BEAMnrc JAWS component. The thickness in the Z direction was set to 7.7 cm and opening widths were based on the field size for which the calculation was being made. The material used was tungsten (W700ICRU).

3.2.3 Incident electron beam

BEAMnrc allows several different sources of radiation to be used. In this study an elliptical electron beam with Gaussian distributions in X and Y is used. The Full-Width Half-Maximum (FWHM) in both the X and Y directions can be adjusted to change the size of the source. The angular spread (UINC, VINC and WINC) can be adjusted, however makes little difference to dose calculations [Sheikh-Bagheri and Rogers, 2002]. The FWHM of the electron beam has little effect on calculated

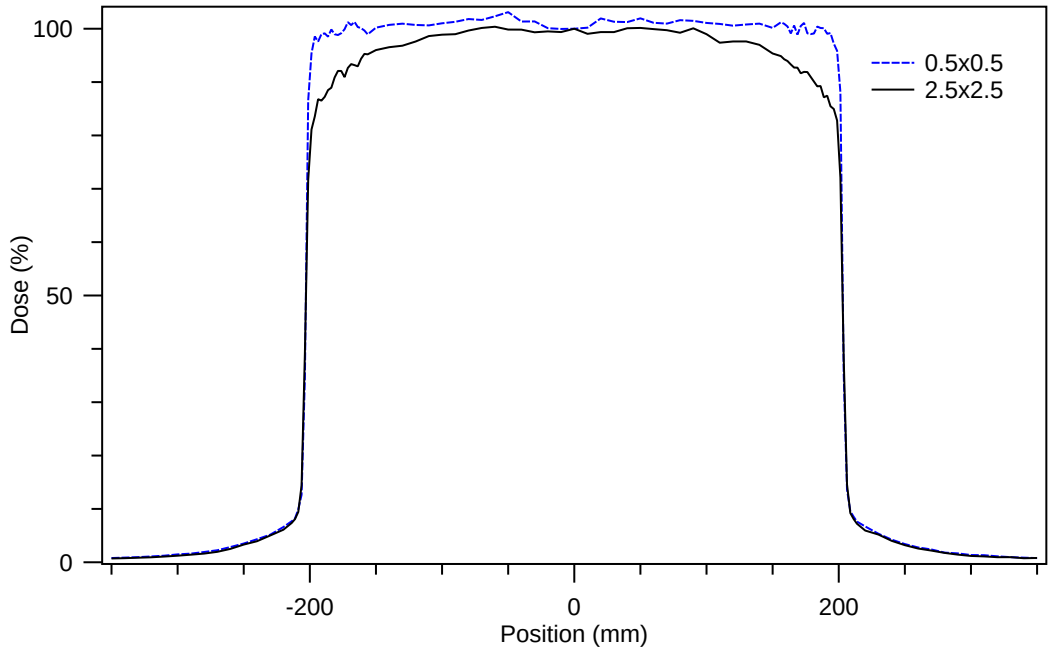

Fig. 3.3: The effect of the size of the incident electron beam on off-axis ratios. The blue, dashed profile shows the increase in off-axis-ratios for a 40 x 40 cm^2 field when a beam size of 0.5 mm is used. The black, solid profile shows the off-axis-ratios for an electron beam size of 2.5 mm. Both calculations used a flattening filter density of 9.5 g cm^{-3}

PDDs for a 10 x 10 cm^2 field, however modifying the FWHM by a few tenths of a mm will result in off-axis-ratio changes of several percent [Sheikh-Bagheri and Rogers, 2002]. Increasing the FWHM of the electron beam results in a relatively more intense photon beam on the central axis [Sheikh-Bagheri and Rogers, 2002]. An example of the effect of the FWHM on off-axis ratios is shown in Figure 3.3.

The energy and FWHM of the incident electron beam were chosen using the method recommended by Sheikh-Bagheri and Rogers [2002]; the energy of the electron beam was set by matching a PDD for a 10 x 10 cm^2 field to measured data. The FWHM of the electron beam was set by matching off-axis-ratios of a 40 x 40 cm^2 field to measured data. As the flattening filter density was not known, and can vary between machines, the density of the flattening filter was another variable modified to match both off-axis-ratios and PDDs of the linear accelerator used in this study. Thus, the modelling was an iterative process involving modifying electron beam energy, electron beam size and density of the flattening filter.

In this study, the incident electron beam is treated as mono-energetic with an energy of 5.95 MeV. The FWHM of the electron beam found to best match measured data was 0.1 x 0.1 cm.

3.3 EGSnrc/BEAMnrc/DOSXYZnrc

3.3.1 Variance reduction techniques

BEAMnrc employs several variance reduction techniques which work to improve the variance of a simulation for a given simulation time or decrease the simulation time for a given variance.

Range rejection

The range rejection method calculates the range of a charged particle and terminates its history (depositing all of its energy at that point) if it cannot leave the current region with energy >ECUTRR. ECUTRR is defined as the range rejection cutoff energy and can be different in each region. To limit the loss of bremsstrahlung photons due to removing electrons that cannot escape the region, an ESAVE value (the maximum energy at which range rejection is considered) of 2 MeV is used

globally. This ensures that range rejection is not considered for electrons with energy greater than 2 MeV. Range rejection is turned off in the target by setting ESAVE to 20 MeV for the tungsten slab representing the target.

Bremsstrahlung splitting

Bremsstrahlung splitting is a variance reduction technique where the creation of bremsstrahlung photons is modified so that for each electron interaction, an arbitrary number of bremsstrahlung photons is produced with their individual weights reduced [Kawrakow and Rogers, 2000]. The energy of the initial electron is reduced by only one of the photon's energies in order to conserve energy loss straggling effects. Therefore for this technique, energy is not conserved in each interaction; energy is conserved on average over many histories [Rogers *et al.*, 2009].

In directional bremsstrahlung splitting (DBS), photons that have been split as described above are removed using a Russian roulette routine if they are not aimed into the field of interest defined by the 'splitting field'[Kawrakow *et al.*, 2004]. The Russian roulette routine compares a random number to a survival threshold of 1/NBRSPL, where NBRSPL is the splitting number. If the random number is less than the threshold, the photon is kept and its weight increased; this photon is now considered a 'fat'(high weight) photon. Otherwise it is removed.

Compton events involving fat photons (those that are not aimed into the splitting field) will result in splitting the Compton event NBRSPL times. The resulting particles are weighted with 1/NBRSPL and Compton scattered photons not directed into the field of interest, as well as secondary electrons, undergo Russian roulette as described above.

For non-fat photons about to undergo a Compton event in a gas, the event proceeds and Russian roulette is run with the resultant Compton scattered photon if it is not pointed towards the field of interest. If the nonfat photon is not in a gas, Russian roulette is run with the photon before the event takes place. If the photon survives, its weight is increased and it becomes a fat photon [Kawrakow *et al.*, 2004].

The result of the above is that only a few fat charged particles reach the phantom surface and so statistics for contamination electrons are poor. To rectify this, BEAMnrc DBS can make use of charged particle splitting whereby electrons crossing

a splitting plane (usually defined at the bottom of the flattening filter) are split NBRSPL times, with a subsequent reduction in weight.

Kawrakow *et al.* [2004] found that DBS increases calculation efficiency by a factor of 500 versus no Bremsstrahlung splitting schemes and a factor of 20 over uniform Bremsstrahlung splitting. The optimum DBS splitting number is found to be 1000 regardless of splitting plane location. Fragoso *et al.* [2009] found between a 53-fold to 115-fold improvement in calculation time when DBS with NBRSPL = 100 and electron splitting was used. Mohammed *et al.* [2016] found an improvement in calculation time of approximately 1130-fold for DBS vs no DBS.

In this work, DBS is used with a splitting number of 1000 and a splitting field radius of 15 cm at 100 cm SSD for a 10x10 cm^2 field and a radius of 45 cm for a 40x40 cm^2 field.

Charged particle splitting is also employed, with the splitting plane at the bottom of the flattening filter (Z = 12.5 cm). A Russian Roulette plane was placed a few mm above the splitting plane (Z = 12.3 cm), still within the flattening filter, as suggested in Rogers *et al.* [2009]. A rejection plane was used with a Z of 75 cm so that it is in-air between the last component of the linear accelerator and the scoring plane.

Photon splitting in DOSXYZnrc

Photon splitting in DOSXYZnrc can be employed to improve the efficiency of photon beam simulations. In this algorithm, photons of weight w_0 entering the DOSXYZnrc phantom are split *nsplit* times and assigned a weight of $w_0/nsplit$. Scattered photons resulting from interactions are culled with a Russian roulette routine whereas charged particles are kept with a reduced weight [Kawrakow and Walters, 2006]. Kawrakow and Walters [2006] found that a splitting number of 40 increased efficiency by a factor of 5 or more. In this study, a splitting number of 40 is used.

3.3.2 Phase space files

Standard BEAMnrc calculations will produce a phase space file for each scoring plane. The phase space file contains data relating to particle position, energy, weight, interactions, etc. for every particle that crosses the scoring plane [Rogers *et al.*,

2009]. For typical accelerator simulations, file sizes range from a few hundred MB to several GB. The phase space files can be used as input to a DOSXYZnrc calculation.

Alternatively, a BEAMnrc treatment head simulation can be used as input to DOSXYZnrc calculations. This uses particles sampled from a BEAMnrc simulation running concurrently with the DOSXYZnrc calculation [Walters *et al.*, 2005]. This method has the advantage of only one simulation being required to run. Kawrakow and Walters [2006] found only a 5-12% efficiency increase when using a phase space file as input, versus using a treatment head simulation as input, as long as DOSXYZnrc photon splitting is used.

In this study the BEAMnrc treatment head simulation was used as input for most DOSXYZnrc calculations.

3.3.3 Other parameters

The boundary crossing algorithm controls the transport of electrons across region boundaries. The boundary crossing algorithm (BCA) EXACT, which is the default BCA, was used as opposed to PRESTA-I. This is due to the overestimation of dose resulting from PRESTA-I [Kim *et al.*, 2012, Walters *et al.*, 2005].

The parameter ECUT helps to reduce calculation time by terminating particles when their energy falls below a user-defined cut-off value. Rogers *et al.* [2009] suggest an electron cut-off energy (ECUT) of 0.7 MeV and photon cut-off energy (PCUT) of 0.01 MeV. Increasing ECUT above 0.511 MeV will result in an increasing uncertainty of surface dose calculations [Kim *et al.*, 2012]. This uncertainty, however, is within 0.1 mm of the surface and is irrelevant for this work, thus ECUT and PCUT values were 0.7 and 0.01 MeV, respectively.

3.4 Comparison with measured data

Measured beam profiles and PDDs were compared with Monte Carlo calculated beam profiles and PDDs. Measured data was collected as discussed in Chapter 4 and was made available by the clinic for use this study. Measured data was in RFA300 Beam Data format. DOSXYZnrc calculations generated .3ddose files, which are described in Walters *et al.* [2005]. A computer program was written in

MATLAB in order to read measured beam data, as well as DOSXYZnrc output, for comparisons.

Output from DOSXYZnrc is in terms of Gy/number of incident particles. In order to compare the output with measured data, the output was normalised. Profiles were normalised using an average of three points; the output on the CAX and the output 2 mm either side of the CAX. PDDs were normalised by the dose at a depth of 10 cm. Linear interpolation between data points was used if the normalisation points did not exist. Software was written to perform one-dimensional gamma analysis between two profiles. The gamma metric is described in Appendix C.1.

Initial model validation was performed by matching a calculated 10 x 10 cm PDD to a measured PDD. A gamma comparison (tolerance 1%, 1 mm) between the measured profile and the calculated profile resulted in 100% of points with a gamma value less than 1.0. The mean γ value was 0.280 and the median γ value was 0.236. This comparison is shown in Figure 3.4. A 3 x 3 cm PDD is shown in Figure 3.5.

Secondary validation was performed by matching a calculated 40 x 40 cm profile to a measured profile at 1.5 cm depth. This comparison is shown in Figure 3.6. The penumbra is sharper in the calculated dose distribution as the voxel size used in the calculation is smaller than the width of the chamber used for data collection. The gamma metric is above 2.0 for the umbra region, however the gamma calculation uses a local difference metric rather than a global; thus the difference in absolute terms is small and is expected to make little difference on subsequent calculations.

The final Monte Carlo model agrees well with measured data.

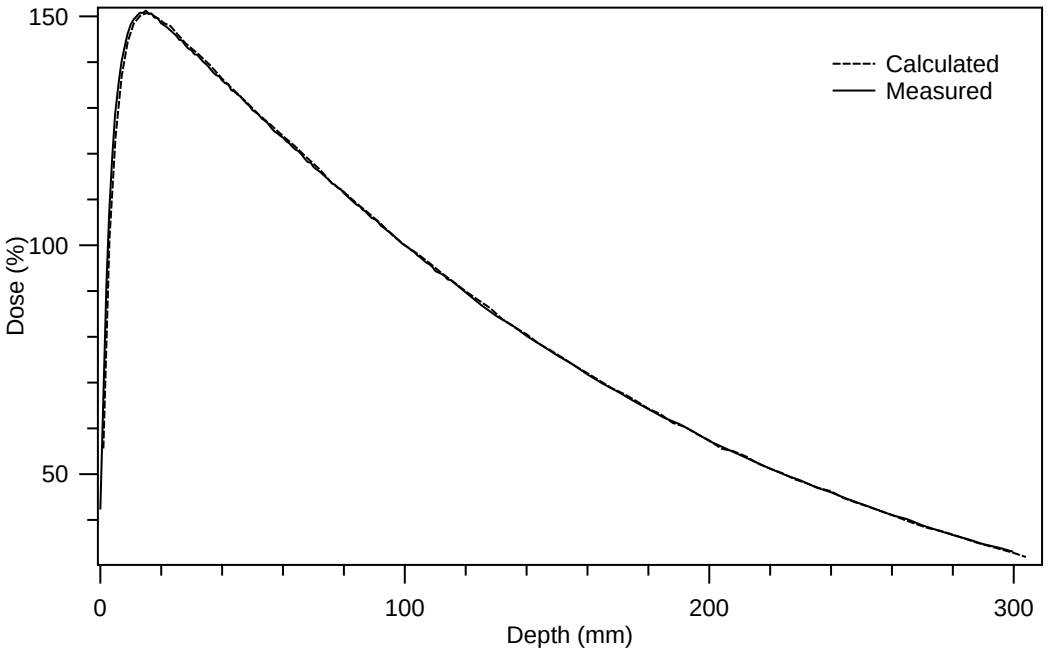

(a) 10 x 10 PDDs

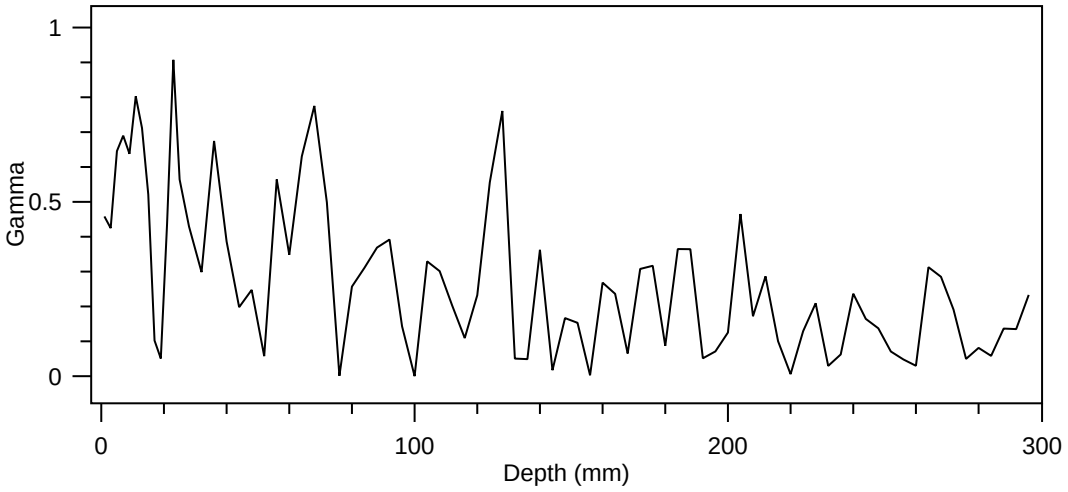

(b) Gamma comparison

Fig. 3.4: A comparison of a 10 x 10 cm PDD curve calculated with EGS/BEAMnrc (Energy = 5.95 MeV, FWHM = 0.1 x 0.1 cm), with the corresponding gamma comparison (1%, 1 mm).

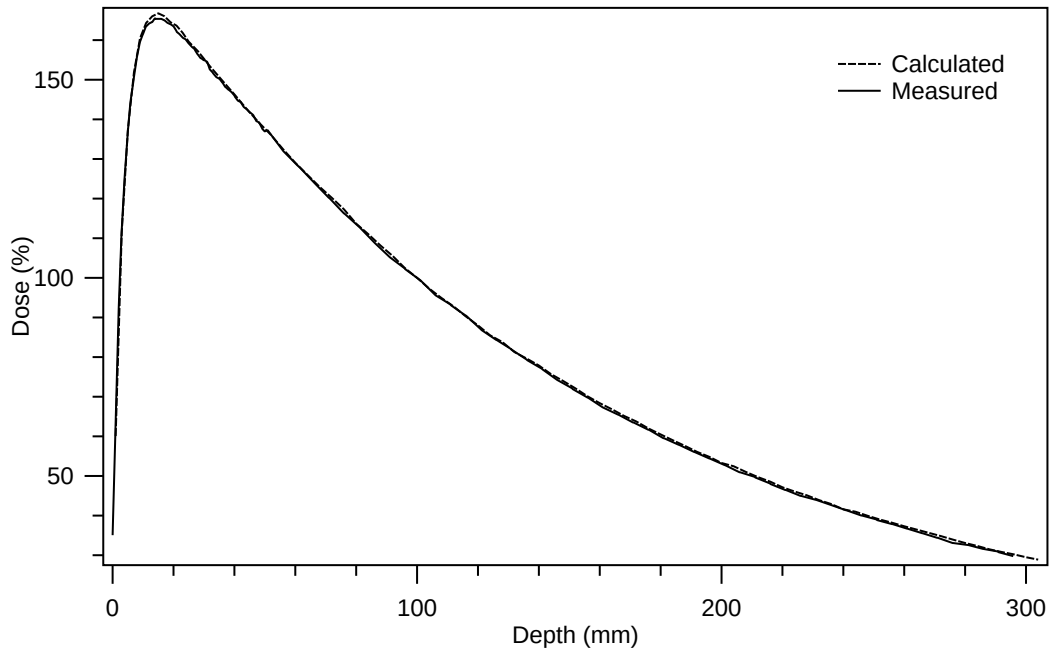

(a) 3 x 3 PDDs

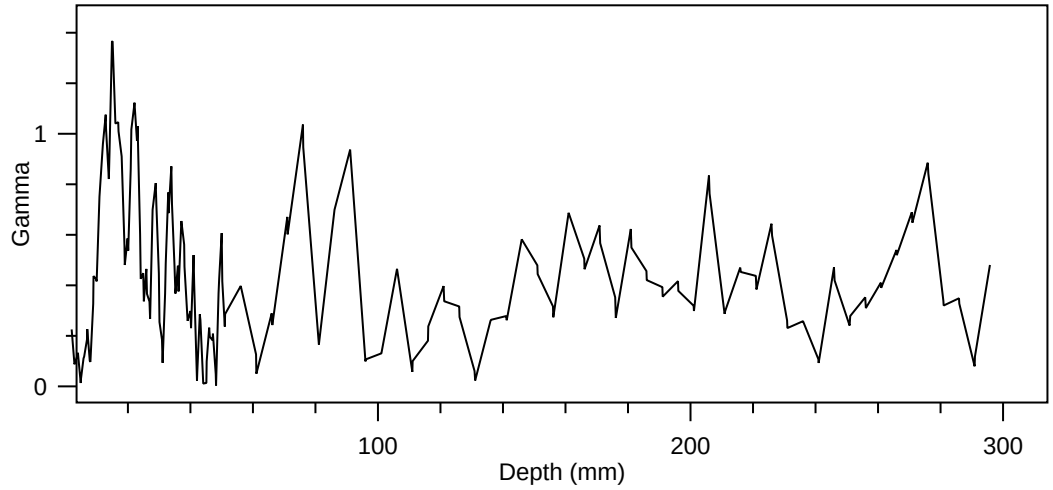

(b) Gamma comparison

.

Fig. 3.5: A comparison of a 3 x 3 cm PDD curve calculated with EGS/BEAMnrc (Energy = 5.95 MeV, FWHM = 0.1 x 0.1 cm), with the corresponding gamma comparison (1%, 1 mm).

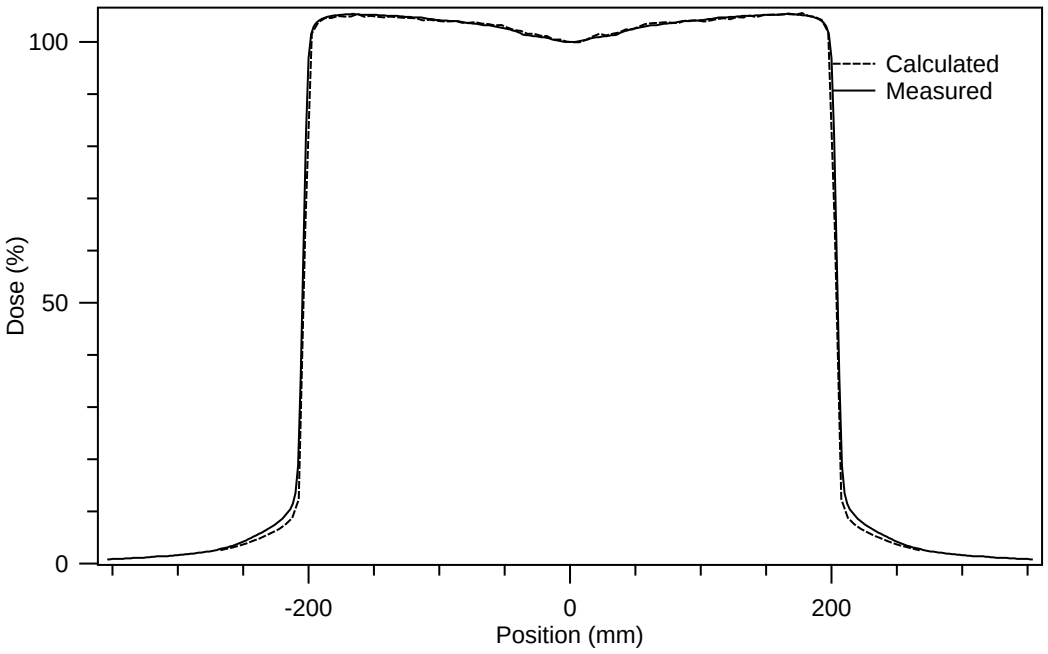

(a) 40 x 40 profiles

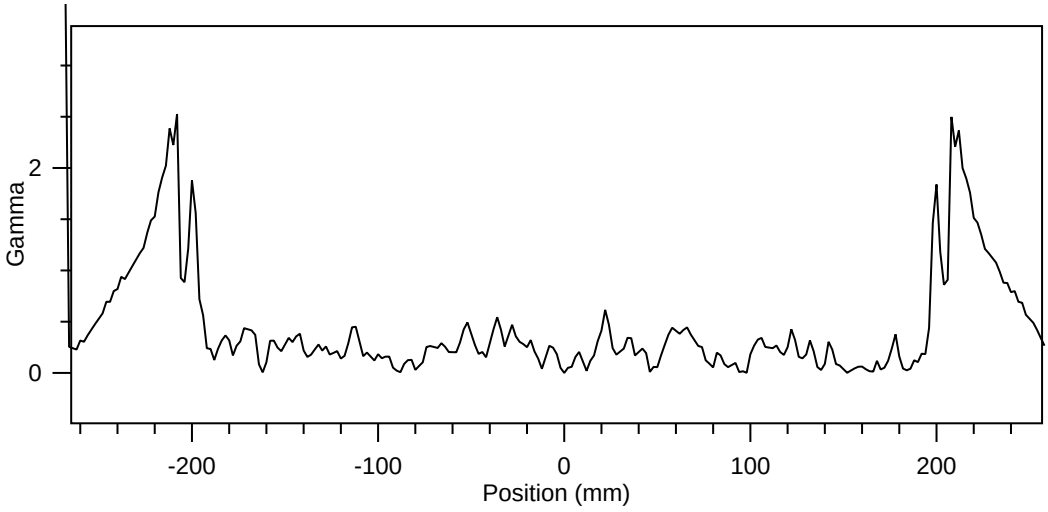

(b) Gamma comparison.

Fig. 3.6: A comparison of a 40 x 40 cm profile (1.5 cm depth) calculated with EGS/BEAMnrc (Energy = 5.95 MeV, FWHM = 0.1 x 0.1 cm), with the corresponding gamma comparison (1%, 1 mm)

4. DOSE CALCULATION MODELS

Dose calculation in external beam radiotherapy has evolved from correction-based algorithms to more advanced model-based algorithms, such as superposition convolution. As part of the commissioning process, linear accelerator beam data is measured and used to tune the dose calculation algorithm or verify an existing model. In this thesis, Acuros and AAA models were created and parameters modified in order to create the best fit with measured data. AAA version 13.7.16 and Acuros version 13.7.16 were used in this work.

4.1 Beam data

4.1.1 Dosimeters

CC13 Ionisation chamber

The Wellhofer (Scanditronix-Wellhofer, Schwarzenbruck, Germany) CC13 ionisation chamber was utilised in many beam data measurements. It has an active volume of 0.13 cm^3. This chamber is small enough to avoid volume averaging effects in most radiation fields but has a large enough volume to obtain a good signal during measurements. For field sizes of around 3 x 3 cm^2 and lower the chamber begins to have some limitations.

IBA SFD Stereotactic diode

The IBA (IBA Dosimetry, Schwarzenbruck, Germany) SFD Stereotactic diode was used for measurements of profiles, PDDs and output factors for small radiation fields. It was used to verify penumbral dose modelling of all fields. The diode has a sensitive volume of 0.017 mm^3. The diode is unshielded which reduces any perturbation effects. Diodes typically show an over-response to lower energy radiation and so may over-estimate the umbra region of larger fields. The advantage of using the

diode in small fields is that it minimises the volume averaging present with larger dosimeters.

4.1.2 Measurement process

Most of the beam data required for commissioning Eclipse had already been measured prior to this project, as it had been used to commission the Pinnacle TPS.

PDDs for field sizes less than 5 x 5 cm^2 were measured with the stereotactic diode. PDDs for field sizes greater than 5 x 5 cm^2 were measured with the CC13 chamber and the stereotactic diode; the diode measurements were combined with the CC13 chamber to provide a higher resolution measurement of the buildup region. Some PDDs had final depths shallower than the 30 cm required by Eclipse, so a small extrapolation to 30 cm was used for those PDDs.

Profiles for field sizes less than 5 x 5 cm^2 were measured with the stereotactic diode. Profiles for field sizes greater than and equal to 5 x 5 cm^2 were measured with the CC13 ionisation chamber. A CC13 chamber was used as a reference dosimeter to remove linear accelerator output variations during measurements. Profiles were measured at depths 1.5, 5, 10, 20 and 30 cm.

Diagonal profiles for the largest field size (40 x 40 cm^2) were not part of the initial beam data set and so had to be measured. Diagonal profiles were measured with the CC13 chamber at depths of 1.5, 5, 10, 20 and 30 cm.

Output factors in the existing beam dataset were measured with a 100 cm SSD and a depth of 10 cm. Eclipse documentation suggests that output factors are measured isocentrically and so were re-measured with a 95 cm SSD and a depth of 5 cm.

Eclipse beam configuration software requires data in the w2CAD format. Our installation of OmniPro did not have the ability to export in this format so some software was written to perform this conversion.

4.2 Collapsed Cone Convolution Superposition

Collapsed Cone Convolution Superposition (CCCs) is used in the Pinnacle TPS (Philips Radiation Oncology Systems, Fitchburg, WI) which is currently the main TPS used in this clinic. CCCs is a superposition convolution algorithm. A general

description of superposition-convolution algorithms is given in Section 2.2.2. Heterogeneity scaling is accounted for by using a radiological distance in the TERMA calculation and when adding contributions from dose kernels.

The CCC algorithm discretises the dose kernels so that each represents a cone where all energy is collapsed to the centre of the cone. Thus for a single interaction point, the energy deposited from the point spread kernel emanates along certain directions. This greatly reduces computation time, since the number of directions that energy is scattered from each interaction point is reduced considerably. Scaling of the kernels due to inhomogeneities is implicitly handled by considering radiological distances.

The CCCs model utilised in this study had been in clinical use for some time and had previously been commissioned.

4.3 Anisotropic Analytical Algorithm

AAA is a superposition convolution algorithm. AAA has four sources used for primary dose deposition: primary source, second source, electron contamination and photon scatter from wedges.

The primary source is a point source which models the bremsstrahlung photons created in the target. The beam spectrum after exiting the target is based on BEAMnrc calculations. The finite size of the source is modelled with the effective target spot size parameters (X and Y directions). Adjusting these parameters changes the size of the penumbra and has a significant effect on the absolute dose level in small fields [Varian, 2014]. The energy fluence across the field is modelled by a radially varying intensity profile curve. Beam hardening in the flattening filter is modelled by attenuating the spectrum with a radially varying amount of flattening filter material, or for a flattening filter free beam, the energy spectrum for each beamlet across the beam is adjusted via the mean energy curve, which decreases smoothly as the radius increases.

The second source models the photons that arise from interactions outside the target: in the flattening filter, primary collimator and secondary jaws. The source is a Gaussian plane at the bottom of the flattening filter. Adjusting the second source parameters, such as the secondary source spot size, mean energy and relative

intensity, has a large effect outside of the primary beam.

The electron contamination source models dose deposited by contamination electrons in the beam. This dose is deposited mainly in the build-up region of the beam.

Eclipse accounts for phantom scatter and head scatter effects via the dose calculation algorithm and the photon beam source. Collimator Back Scatter Factors (CBSF) are calculated by Eclipse to account for the remaining change in output factors not modelled by the algorithm and photon beam source. Physically, they are supposed to represent the collimator backscatter into the monitor chamber. CBSFs are calculated from measured output factors via the equation

$$CBSF(X,Y) = \frac{OF_{ref}}{OF(X,Y)} \times \frac{D'(X,Y)}{D'_{ref}} \tag{4.1}$$

with the following parameters:

X, Y The collimator settings;

OF_{ref} The output factor for the reference field size;

$OF(X,Y)$ The measured output factor for field size X,Y;

$D'(X,Y)$ The reference point calculated by the algorithm for the field size X,Y and the reference geometry, when ignoring the effect of the collimator backscatter;

D'_{ref} The dose calculated by the algorithm for reference conditions in the reference geometry, when ignoring the effect of the collimator backscatter.

The wedge scatter source models scatter originating from each point in a physical wedge.

The primary beam source model describes the beam entering the patient and is divided into finite-sized beamlets. AAA calculates dose in a divergent dose matrix which is aligned along the coordinate system within the beam fanlines [Varian, 2015].

4.3.1 AAA Volumetric Dose Calculation

As mentioned above, AAA divides the clinical beam into finite-size beamlets, represented by the symbol β. The beamlets emerge from the focal spot of each source, which is different for the primary, extra-focal and wedge-scattered photons.

The dose to an arbitrary point is calculated by summing up the dose contributions from all of the individual beamlets.

A depth z is defined along the central fanline of each beamlet. AAA divides scatter calculations into two directions: in the direction of the central fanline and in the lateral direction [Varian, 2015].

Depth direction In the depth direction, an energy deposition density function $I_\beta(z, Q)$ is obtained from a poly-energetic pencil beam kernel which is pre-calculated and derived from Monte Carlo simulations. Q is the average electron density of the voxel. Electron density in each voxel is calculated from the user-defined HU to electron density curve.

Practically, $I_\beta(z, Q)$ is calculated by integrating over the sphere surface of the pencil beam for the radiological depth z:

$$I_\beta(z) = \int\int h'_\beta(t, v, z)dtdv \tag{4.2}$$

where $h_\beta(t, v, z)$ is the pencil beam kernel.

To account for tissue heterogeneity in the depth direction, $I_\beta(z, \rho)$ is obtained by

$$I_\beta(z, \rho) = I_\beta(z') \times \frac{\rho(0, 0, z)}{\rho_{water}}, \tag{4.3}$$

where z' is the radiological depth, and is defined as

$$z' = \int_0^z \frac{\rho(0, 0, t)}{\rho_{water}}dt \tag{4.4}$$

A one-dimensional scatter kernel $k_z(z)$ is convolved with the energy function of the beamlet (after lateral scatter is included) in order to account for gradual changes of scatter conditions after heterogeneity borders. To correct for the effect that this convolution has on the depth of calculated dose, the pencil beam kernel $h_\beta(t, v, z)$ in Equation 4.2 is replaced by $h'_\beta(t, v, z)$, where $h'_\beta(t, v, z)$ is $h_\beta(t, v, z)$ convolved with the deconvolution kernel derived from $k_z(z)$.

Lateral direction Lateral photon scatter is modelled with a scatter kernel $K_\beta(x, y, z)$. Practically, the scatter kernel is the weighted sum of six exponential functions with

parameters derived by fitting the functions to the Monte Carlo-derived scatter kernels.

Lateral density scaling of the scatter kernel is handled by dividing the calculation into a finite number (16) of rays diverging from the origin. The radiological scaling used by the scatter kernels is performed independently in four lateral directions [Sievinen *et al.*, 2005].

The anisotropic term in the algorithm name comes from the anisotropic density scaling of the scatter kernel in the four lateral directions. The analytic term in the algorithm name is due to the convolution of the scatter kernel being performed analytically.

The calculated energy deposited at each point is converted to dose by multiplying by the ratio of water electron density and electron density at the point, and by a scaling factor that converts between J m^{-3} to Gy.

4.3.2 AAA beam modelling

Eclipse has an automated optimisation procedure in which the program attempts to fit parameters of the beam model in order to produce the best match between measured and calculated beam profiles and PDDs. The optimiser, in general, did a good job of producing a close fit between measured and calculated data, however some modifications were made post-optimisation to produce a better fit. The main parameters that were changed related to the secondary source, namely its size, relative intensity and mean energy. These parameters had a significant effect on the out of field dose and the shape of the outer area of the interumbra. The target spot size of the primary source was set to 0 mm in the Y direction and 1.0 mm in the X direction.

Figures 4.1 to 4.6 show the final agreement between measured and calculated data for AAA. The AAA model showed some discrepancies in the maximum dose region of the PDD (when normalised at a depth of 10 cm) for the 5 x 5 cm field. The interumbra of larger fields showed some disagreement with measurement, with the disagreement becoming smaller at depth. Some compromises were made to match the penumbra of the open fields, this meant that the penumbra as calculated by AAA in the smaller fields showed differences to measured.

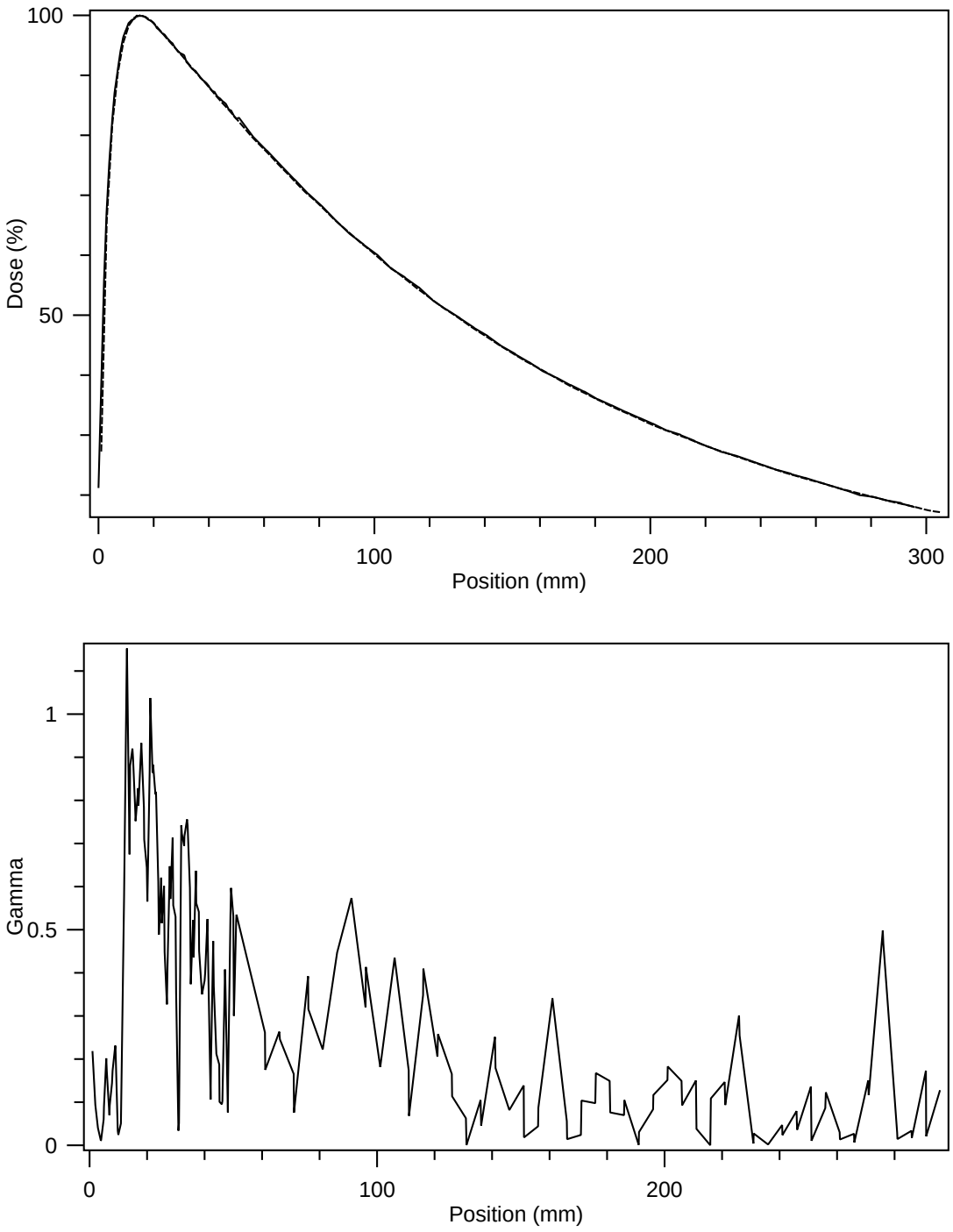

Fig. 4.1: A comparison of a 3 x 3 cm PDD (top) calculated with AAA, with 1% 1 mm gamma comparisons (bottom). Dashed lines show the calculated PDDs, while solid lines show the measured PDDs.

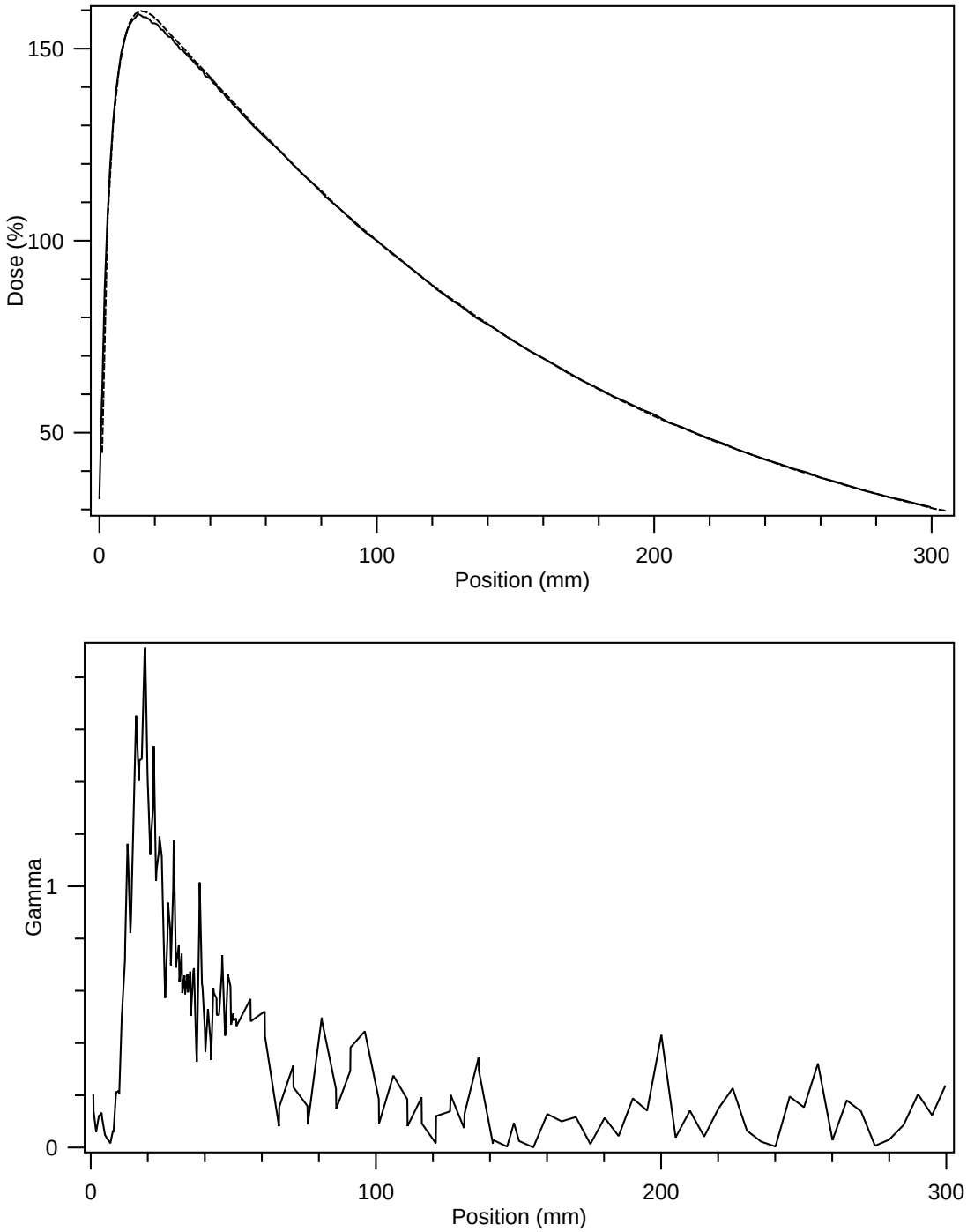

Fig. 4.2: A comparison of a 5 x 5 cm PDD (top) calculated with AAA, with 1% 1 mm gamma comparisons (bottom). Dashed lines show the calculated PDDs, while solid lines show the measured PDDs.

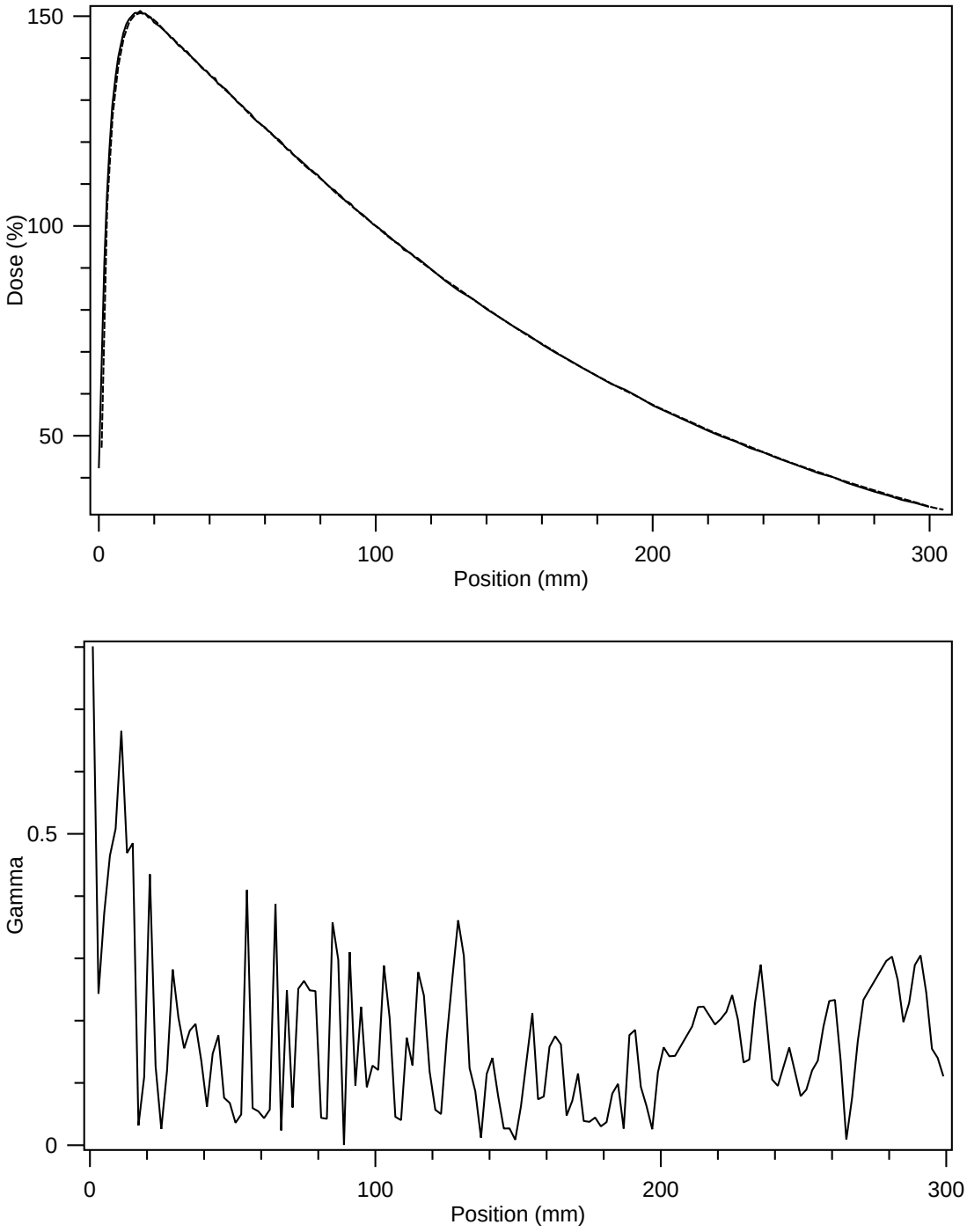

Fig. 4.3: A comparison of a 10 x 10 cm PDD (top) calculated with AAA, with 1% 1 mm gamma comparisons (bottom). Dashed lines show the calculated PDDs, while solid lines show the measured PDDs.

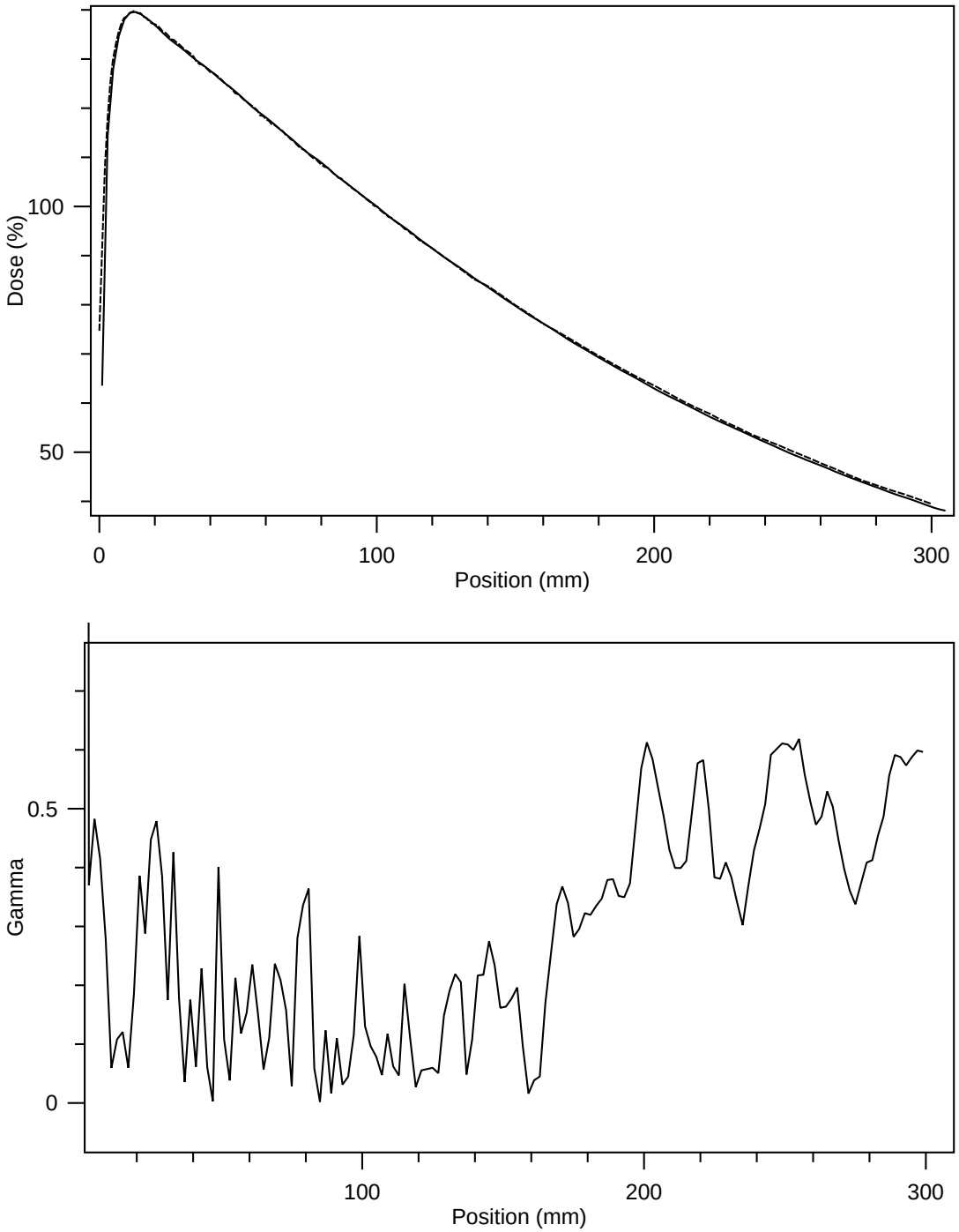

Fig. 4.4: A comparison of a 40 x 40 cm PDD (top) calculated with AAA, with 1% 1 mm gamma comparisons (bottom). Dashed lines show the calculated PDDs, while solid lines show the measured PDDs.

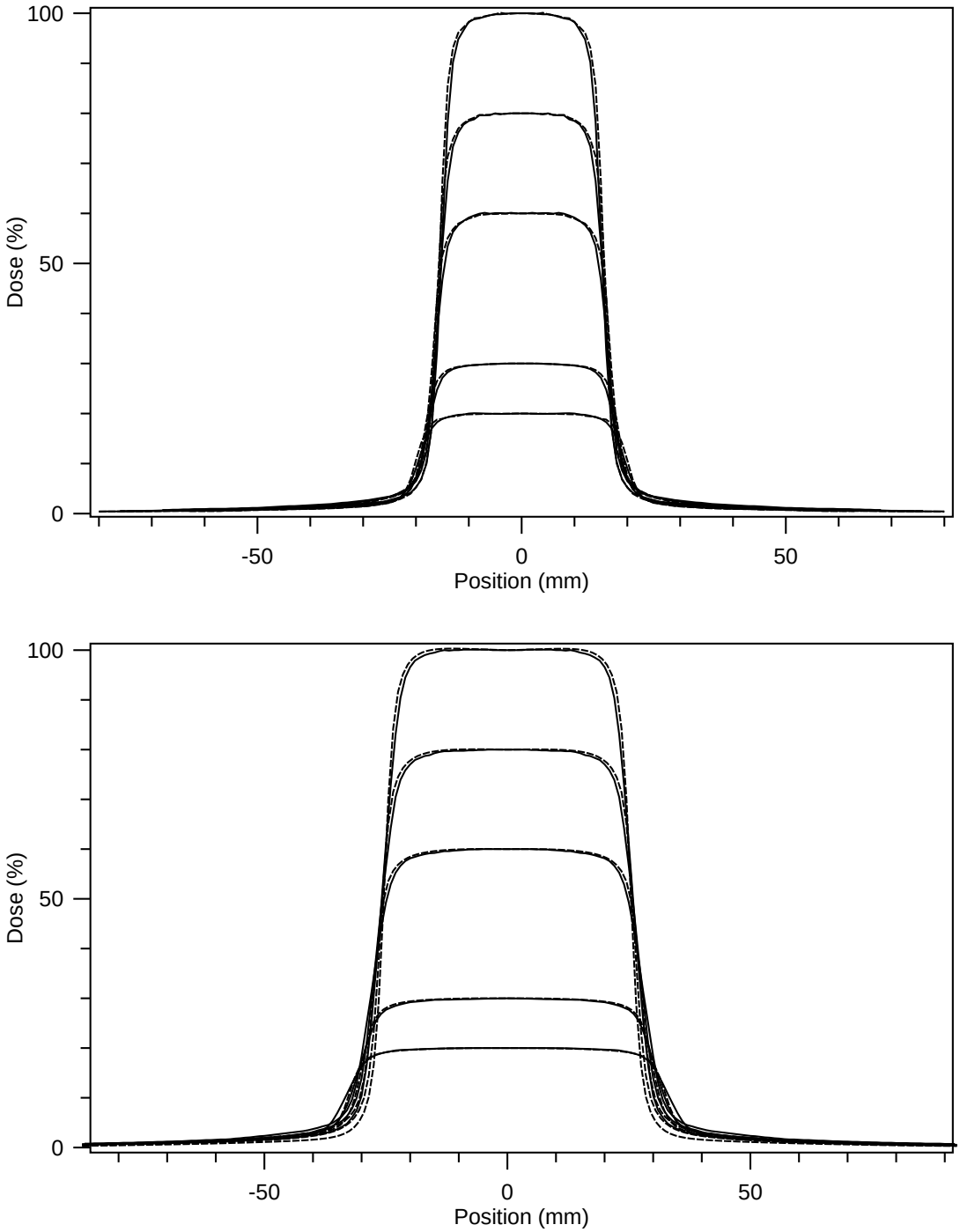

Fig. 4.5: A comparison of 3 x 3 cm (top) and 5 x 5 cm (bottom) profiles calculated with AAA. Profiles shown are at 1.5, 5, 10, 20 and 30 cm depths. Dashed lines show the calculated profiles, while solid lines show the measured profiles.

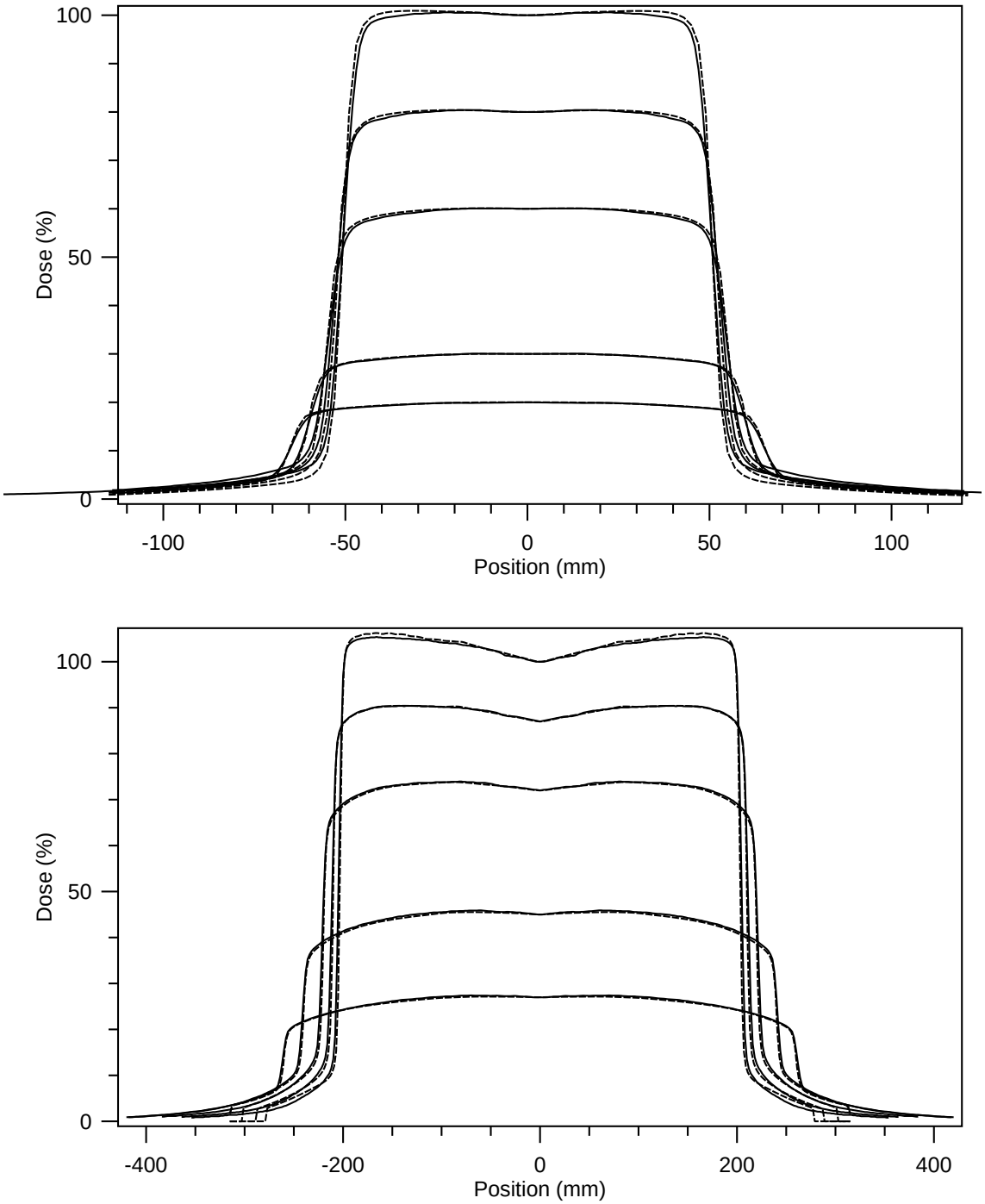

Fig. 4.6: A comparison of 10 x 10 cm (top) and 40 x 40 cm (bottom) profiles calculated with AAA. Profiles shown are at 1.5, 5, 10, 20 and 30 cm depths. Dashed lines show the calculated profiles, while solid lines show the measured profiles.

4.4 Acuros XB

Acuros XB solves the time-independent three-dimensional system of coupled Linear Boltzmann Transport Equations (LBTE). The LBTE describes the macroscopic transport of particles. For brevity, the equations solved by Acuros are not presented in this thesis. The LBTE and the implementation of Acuros are described in detail by Failla *et al.* [2010].

Acuros uses the same source model as AAA. The model consists of primary, extra focal, electron contamination and wedge scatter. The difference is in the calculation of dose once the primary and secondary sources are transported into the patient.

The steps taken by Acuros dose calculation are as follows:

1. Transport of source model fluence into patient
2. Calculation of scattered photon fluence in patient
3. Calculation of scattered electron fluence in patient
4. Dose calculation.

Step 1 is repeated for each beam and involves ray tracing to calculate the uncollided photon and electron fluence distributions for each source [Failla *et al.*, 2010]. Once step 1 is performed for all beams, steps 2 to 4 are performed once for the calculation.

Because Acuros uses physical properties of materials rather than solely the density or electron density, the algorithm must know the material of each voxel. This is achieved with a library of materials, where a lookup of mass density will give the material. Mass density is determined from the Hounsfield Unit of the voxel.

To reduce computation time, the computational grid used for the transport of scattered photons and electrons is of a variable size, with a higher spatial resolution inside the beam fields and a lower spatial resolution in lower dose, lower gradient regions outside the beam penumbra [Failla *et al.*, 2010]. Energy discretisation is also performed so that the Acuros XB cross section library includes 25 photon energy groups and 49 electron energy groups [Failla *et al.*, 2010]. The discrete ordinates method is used to discretise in angle, which is a standard method used to discretise

angles when solving particle transport equations. The angular discretisation varies with particle type and energy.

Acuros XB has a cutoff kinetic energy for electrons of 500 keV and a cutoff for photons below 1 keV. When a particle has an energy below the cutoff energy, any subsequent interactions are assumed to happen only in that voxel [Failla *et al.*, 2010]. These parameters are non-adjustable but are equivalent to typical values used in Monte Carlo techniques.

Simplifications are made to speed up calculation time, such as that pair production is assumed to be electron + electron and not electron + positron. It is assumed that no bremsstrahlung radiation is produced in the patient/phantom.

These two simplifications are unlikely to have a significant effect on overall calculation accuracy. Berger and Seltzer [1982] shows that the ratio of restricted stopping powers between positrons and electrons is 1.00 ($\Delta = 1$ keV).

The second simplification, that no bremsstrahlung radiation is produced in the patient, has a small but insignificant effect on the dose calculation. Electrons with energies between 0.5 - 6 MeV have bremsstrahlung fractions between 0.2% and 2% in water [Johns and Cunningham, 1983].

Acuros and Monte Carlo approach dose calculation in similar ways: by simulating or solving particle transport equations. They differ in cross-section data, variance reduction techniques and approximations. Monte Carlo calculations discretise with the number of particles in a simulation. Acuros discretises with energy, angle and spatial resolution. As the number of particles in Monte Carlo simulations increases and the size of the grid in Acuros decreases, the two methods will converge on the same result.

4.4.1 Dose to water vs dose to medium

There are two quantities reported in dose calculation algorithms; dose to water or dose to medium. Most algorithms compute and report dose to water. Many radiotherapy treatment regimes are based on results using prescriptions of dose to water. Beam data measurements are typically made in water and current absolute dosimetry protocols recommend calibrating to absorbed dose in water [Andreo *et al.*, 2001]. Monte Carlo simulations calculate dose to medium by default. For soft tissue,

the difference is less than 1% but it can exceed 10% in material such as corticol bone [Siebers *et al.*, 2000].

Acuros can calculate either dose to water or dose to medium. Once Acuros has solved for electron angular fluence, the dose in any voxel is given by integrating over energy and solid angles and multiplying the electron fluence by $\frac{\sigma^e_{ED}(\vec{r},E)}{\rho}$, which is the macroscopic electron energy deposition cross section, in units of MeV/cm divided by the mass density of the material [Failla *et al.*, 2010]. If calculating dose to water, σ^e_{ED} and ρ are based on water. If calculating dose to medium, they are based on the material properties in the voxel.

4.4.2 Acuros XB beam modelling

Similarly to AAA, the automated optimisation procedure was run using the imported beam data in order to set the required parameters. The beam model required significantly more tweaking that did AAA. Results are shown in Figures 4.7 to 4.12. Disagreements between calculated and measured PDDs were similar to those for AAA. The interumbra region of the shallower profiles calculated by Acuros showed disagreement near the penumbra.

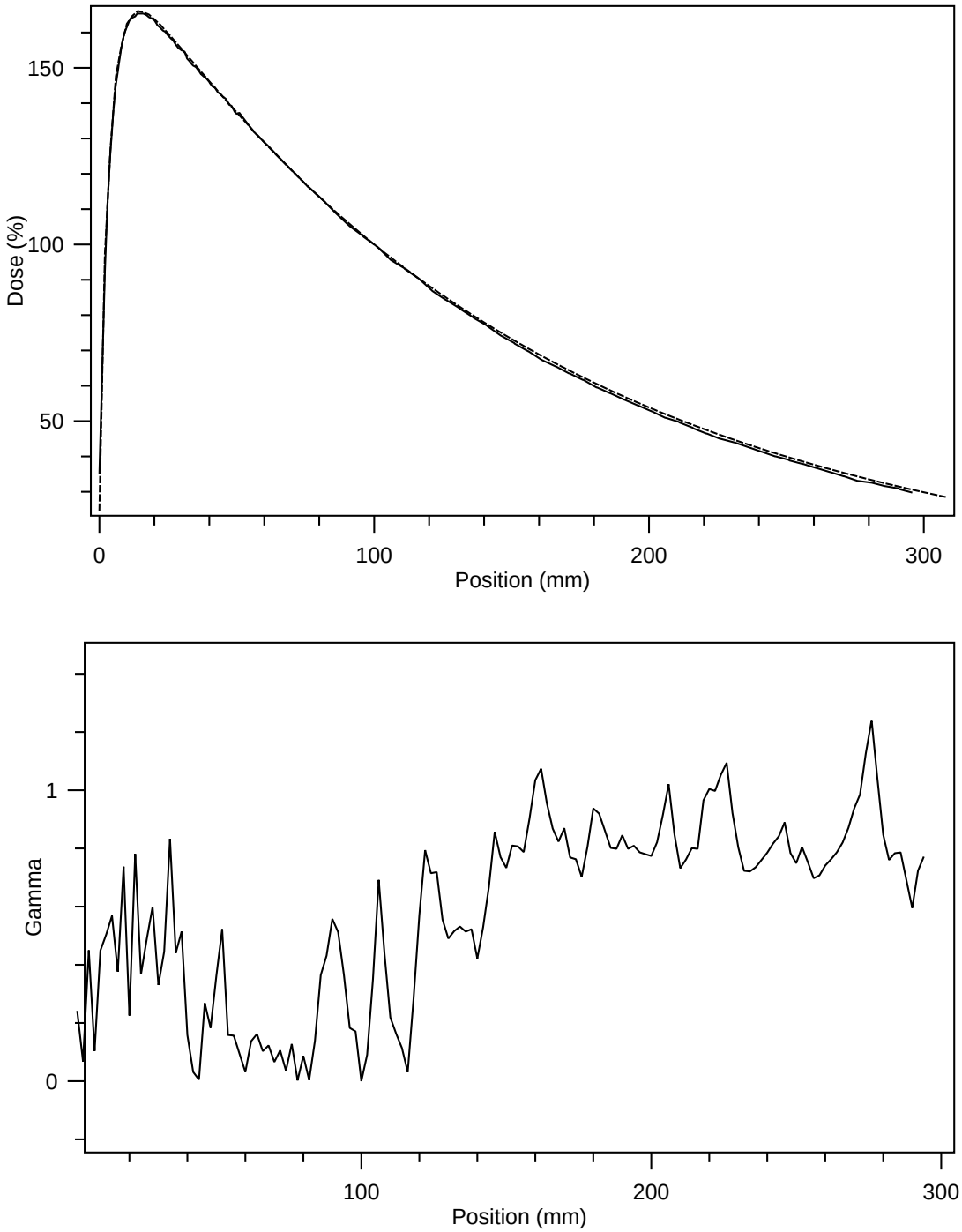

Fig. 4.7: A comparison of a 3 x 3 cm PDD (top) calculated with Acuros, with 1% 1 mm gamma comparisons (bottom). Dashed lines show the calculated PDDs, while solid lines show the measured PDDs.

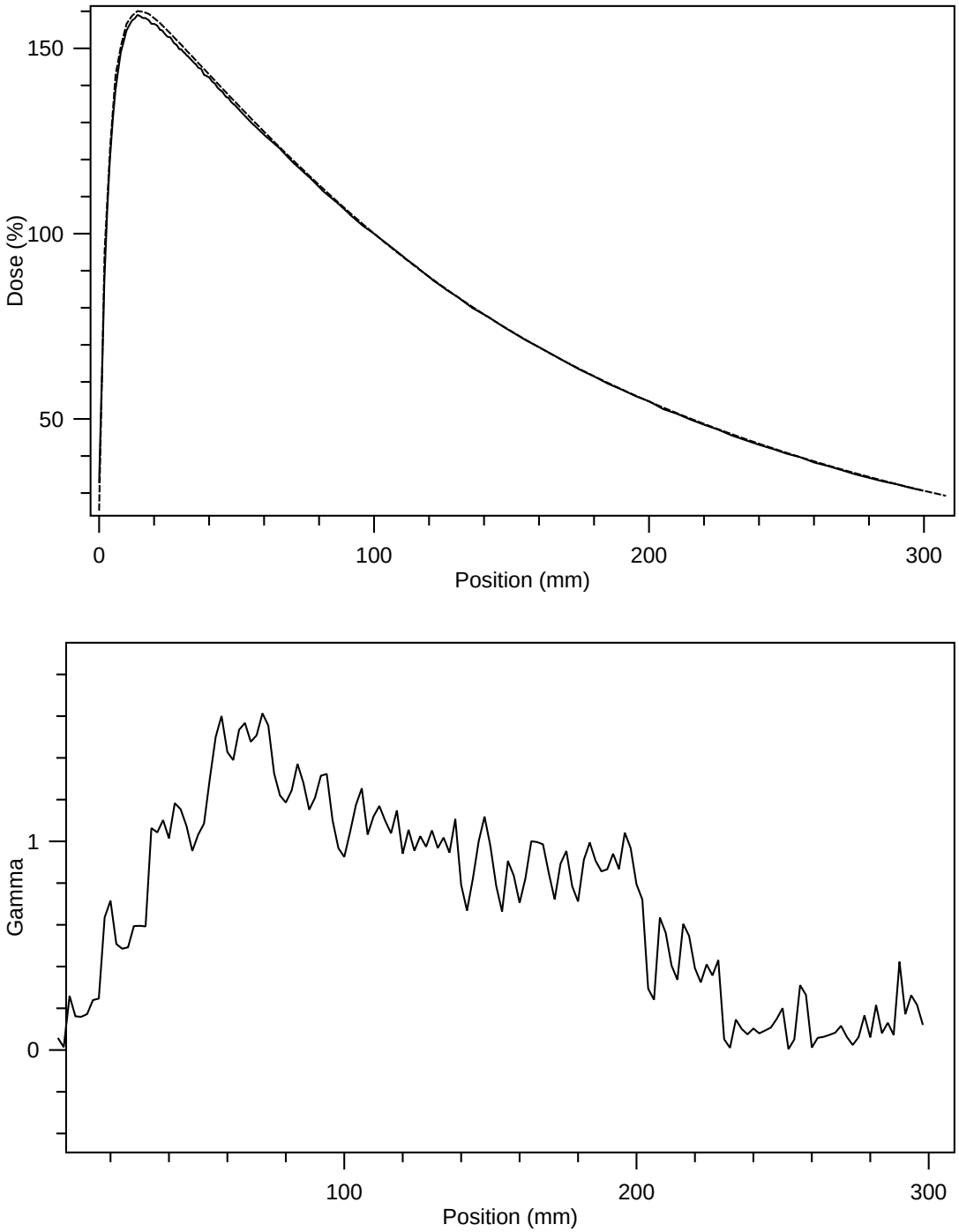

Fig. 4.8: A comparison of a 5 x 5 cm PDD (top) calculated with Acuros, with 1% 1 mm gamma comparisons (bottom). Dashed lines show the calculated PDDs, while solid lines show the measured PDDs.

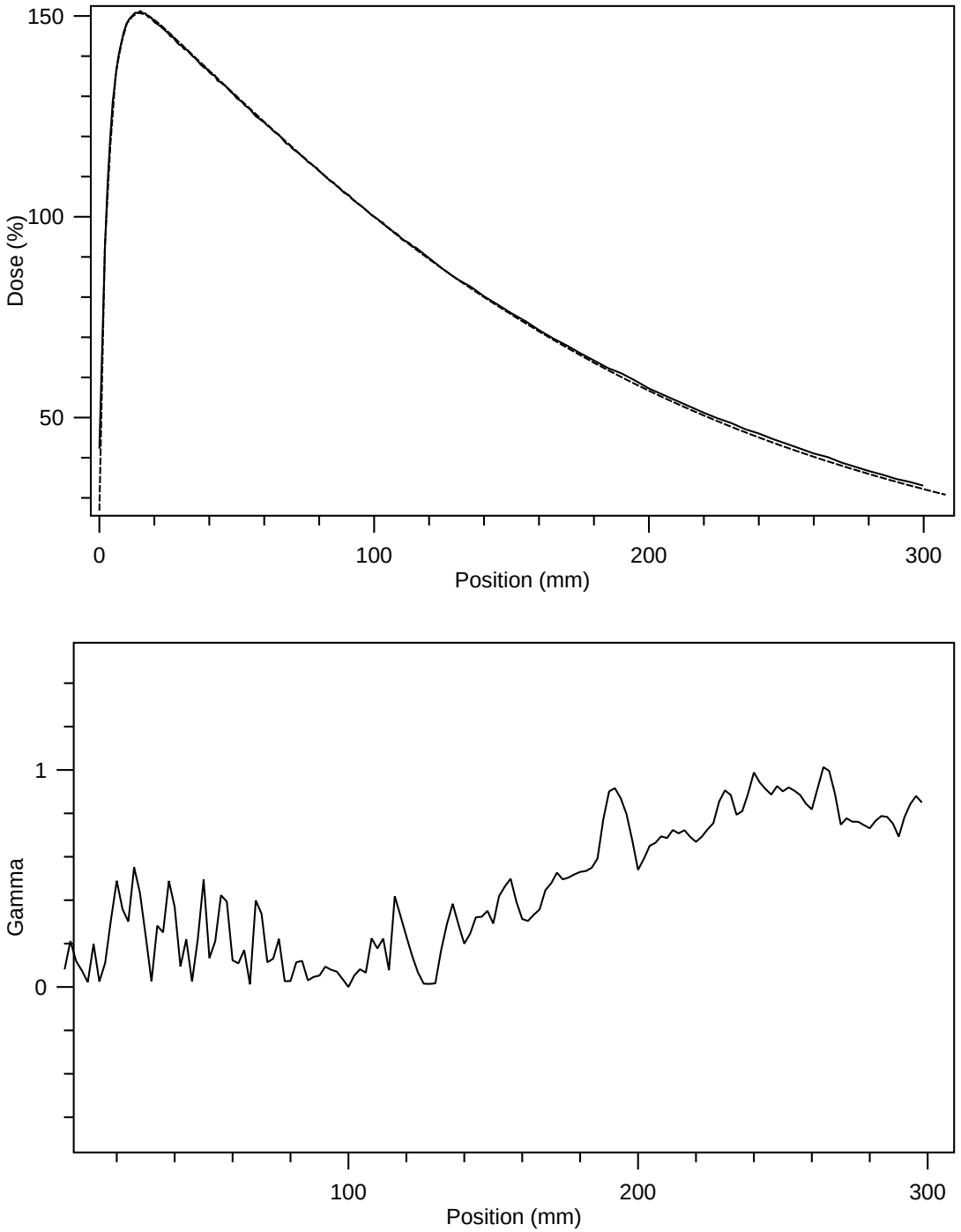

Fig. 4.9: A comparison of a 10 x 10 cm PDD (top) calculated with Acuros, with 1% 1 mm gamma comparisons (bottom). Dashed lines show the calculated PDDs, while solid lines show the measured PDDs.

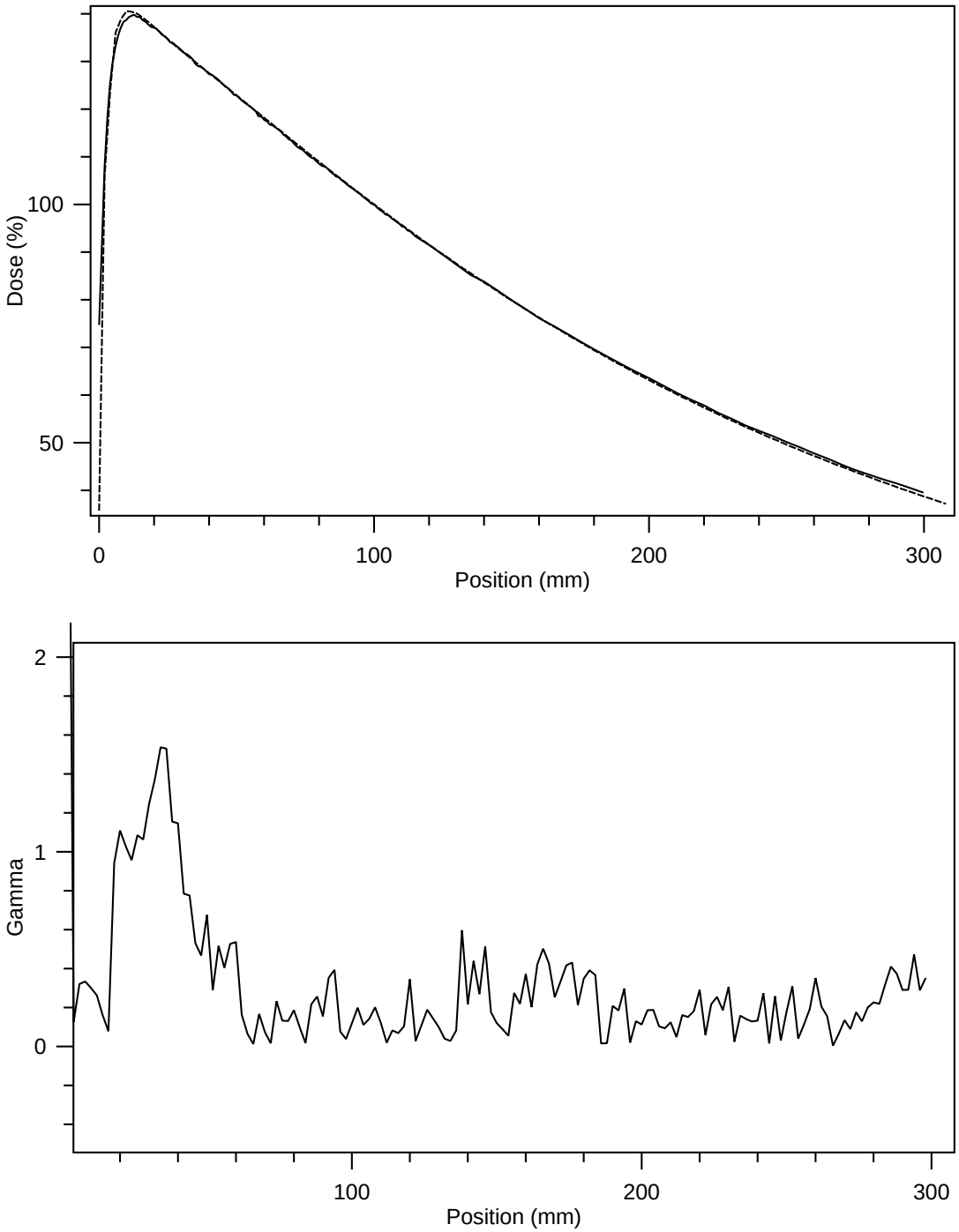

Fig. 4.10: A comparison of a 40 x 40 cm PDD (top) calculated with Acuros, with 1% 1 mm gamma comparisons (bottom). Dashed lines show the calculated PDDs, while solid lines show the measured PDDs.

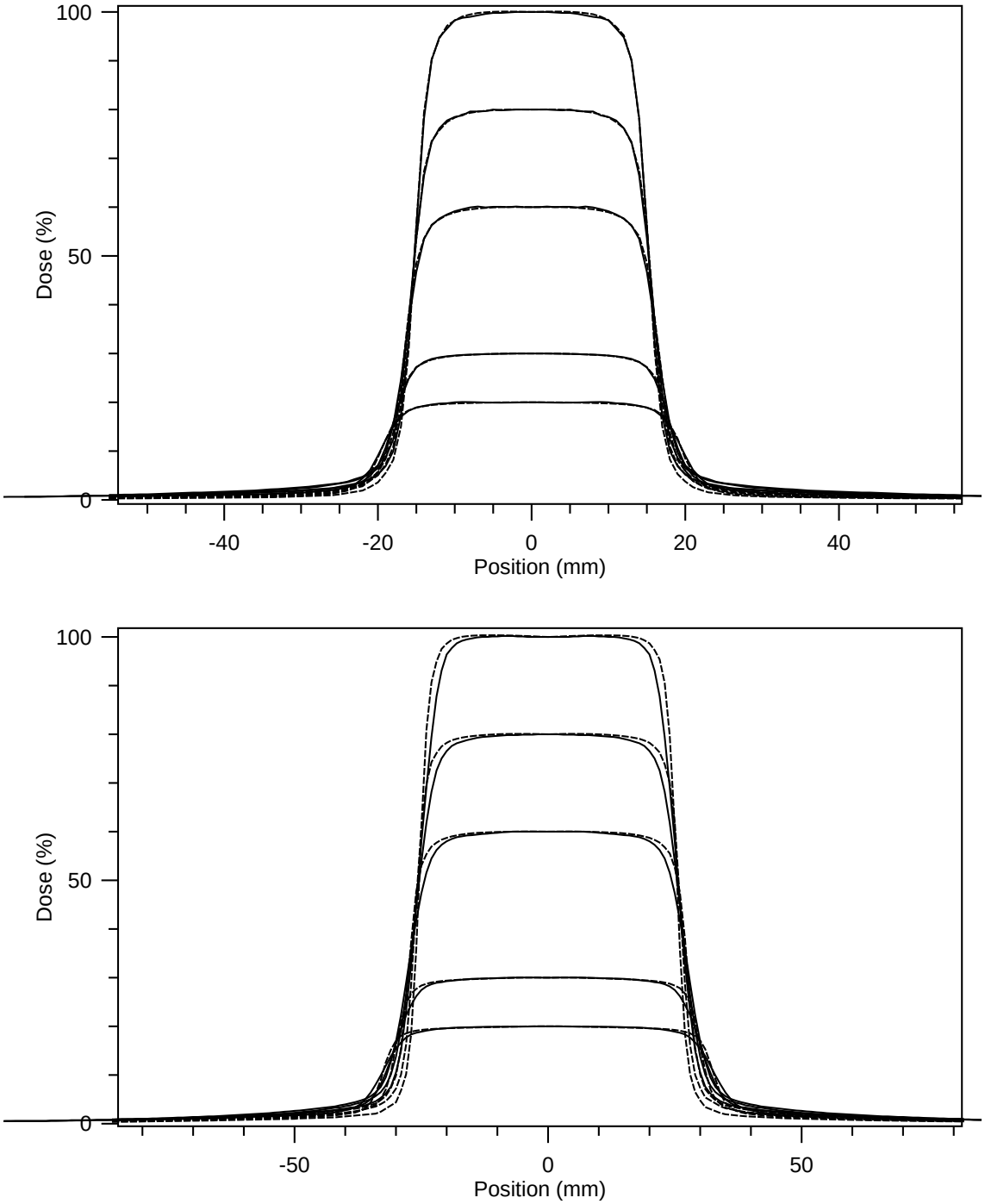

Fig. 4.11: A comparison of 3 x 3 cm (top) and 5 x 5 cm (bottom) profiles calculated with Acuros. Profiles shown are at 1.5, 5, 10, 20 and 30 cm depths. Dashed lines show the calculated profiles, while solid lines show the measured profiles.

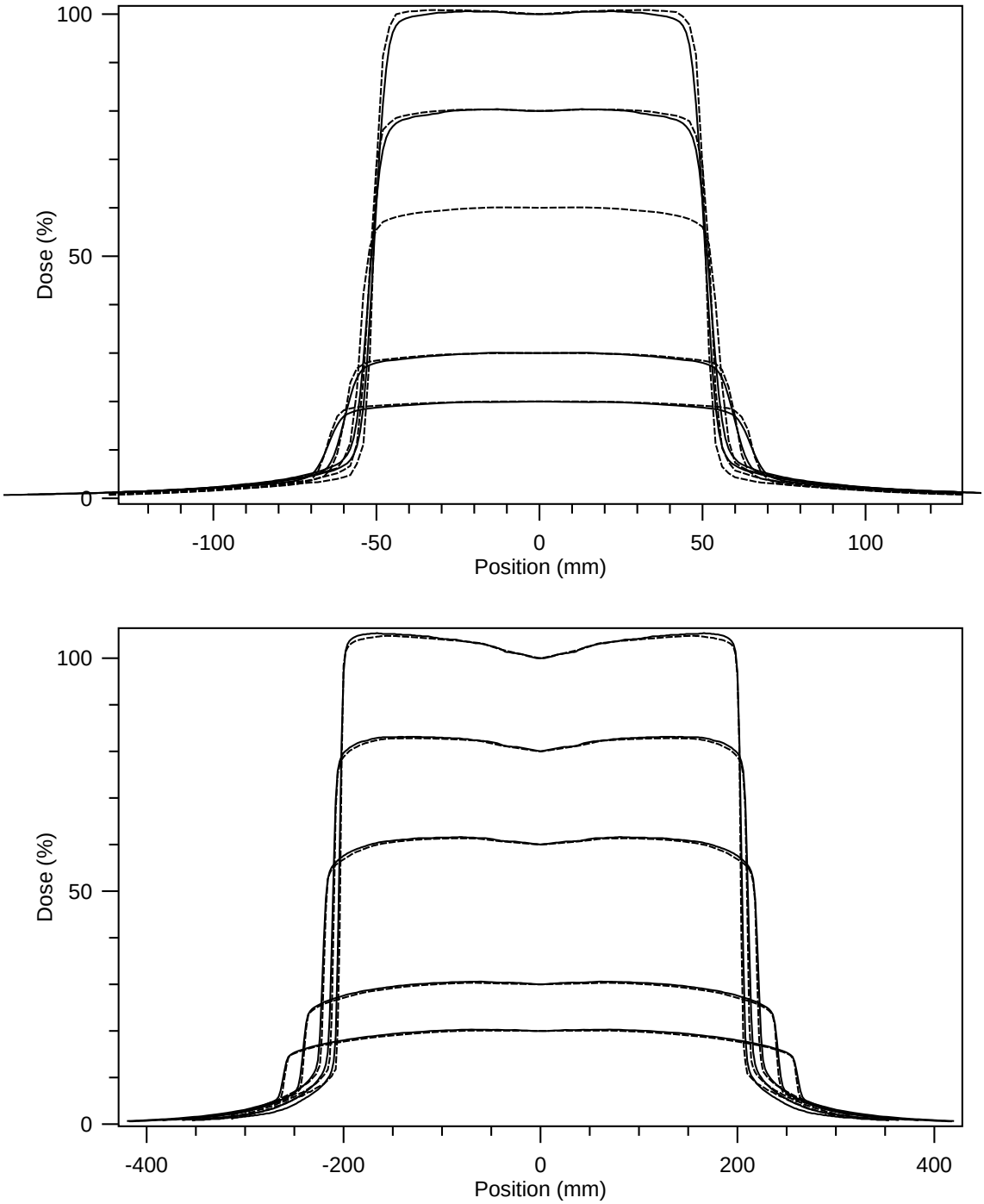

Fig. 4.12: A comparison of 10 x 10 cm (top) and 40 x 40 cm (bottom) profiles calculated with Acuros. Profiles shown are at 1.5, 5, 10, 20 and 30 cm depths. Dashed lines show the calculated profiles, while solid lines show the measured profiles.

5. ALGORITHM ACCURACY

The agreement of the Acuros and AAA models to measured beam data was presented in Chapter 4. In this chapter, measurements and Monte Carlo calculations are used to investigate algorithm performance in geometry of increasing complexity.

5.1 Equipment

5.1.1 Tissue-equivalent material

CIRS tissue equivalent slabs were used in this thesis. The slabs have approximately the same material composition as common inhomogeneities such as bone, lung and water. Slabs representing average-lung are used in this thesis. The lung slabs have mass densities of 0.3346 g/cm^3.

5.1.2 Chambers

The 31010 ionisation chamber (PTW, Freiburg, Germany) is a miniature thimble chamber. This chamber has a measurement volume of 0.125 cm^3 and a length of 6.5 mm. The PTW 31010 was used for point dose measurements. The effective point of measurement of 1.65 mm towards the source was taken into account for all measurements.

5.2 Algorithm accuracy in slab geometry

Measurements were made in slab geometry to assess the ability of each algorithm to calculate dose before and after heterogeneities.

CIRS slab geometry was used in order to create the various set-ups. In each set-up, 4 cm of water equivalent material in the form of two 2 cm slabs was placed on top of the inhomogeneity slab. The inhomogeneity slab was followed by 15 cm of water-equivalent material. The set-up is shown in Figures 5.1 and Figure 5.2.

The top of the phantom was placed at 100 cm SSD and the linac gantry and collimator were set to zero degrees. The solid water slab containing the ion chamber slot was moved to the various slab positions to measure dose at depth. Each time the slab was moved the alignment of the linac cross-hairs was checked against the alignment markings on the top of the slab.

Each measurement was normalised to the ion chamber reading in slab 2 of the inhomogeneous set-up. Calculated dose profiles were also normalised at a depth of 2.84 cm, which corresponds to the position of the effective point of measurement of the chamber.

The measurement geometry was reproduced in the treatment planning system by creating regions of interests based on the size of the slabs. The ROIs were manually assigned densities. For Acuros, the ROIs were assigned to the appropriate material.

Acuros calculations were calculated with dose to water. Monte Carlo calculations were scaled in lung and bone from dose to the medium to dose to water. This was performed by multiplying the PDD by the average water-to-medium stopping power ratios as calculated by Siebers *et al.* [2000]. For lung, the stopping power ratio was 0.999, while for bone the ratio was 1.117. Since the density of bone affects the stopping power ratios, there is some uncertainty in using an externally calculated stopping power ratio. It is expected that this uncertainty is less than 1% for the dose in bone. For an 18 MV beam in cortical bone, Siebers *et al.* [2000] show a variation in stopping power ratio of approximately 1% between densities of 1.5 and 2.0 g/cm^3.

The slab geometry measurements show that, distal to lung, AAA overestimates the dose relative to Acuros and Monte Carlo calculations. In the lung inhomogeneity, AAA calculates lower dose than both Acuros and Monte Carlo. Figures 5.3 to 5.5 show examples of the slab geometry calculations for 6 cm of lung, while the rest of the profiles are shown in Appendix A.

Figure 5.6 shows that the agreement to measurements generally improves as the thickness of the lung slab decreases. It also shows that Monte Carlo and Acuros are in close agreement for all configurations.

Figure 5.7 shows that, for AAA, calculations with the 3 x 3 cm field agree better than the larger field sizes. A discussion of this particular result is presented in

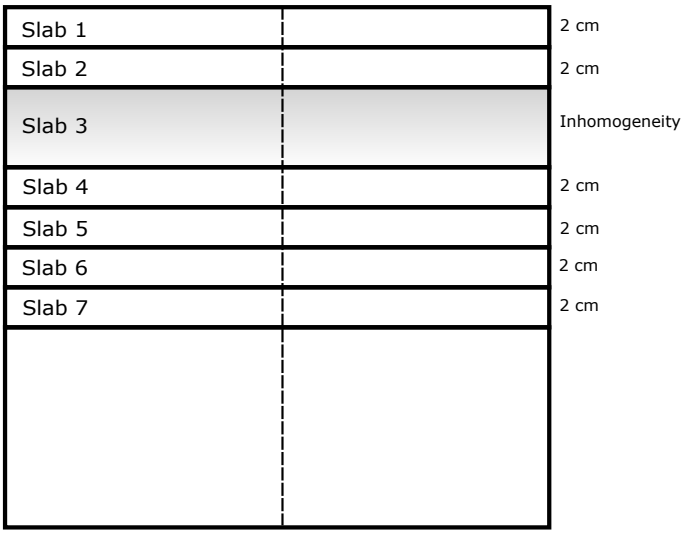

Fig. 5.1: The slab geometry set-up used to assess each algorithm's ability to predict dose after an inhomogeneity.

Chapter 6.

In summary, Acuros, Monte Carlo and AAA have an average difference of -0.06 $\pm$ 0.13%, -0.09 $\pm$ 0.12% and +0.6 $\pm$ 0.18% respectively compared to measured doses distal to the lung slab.

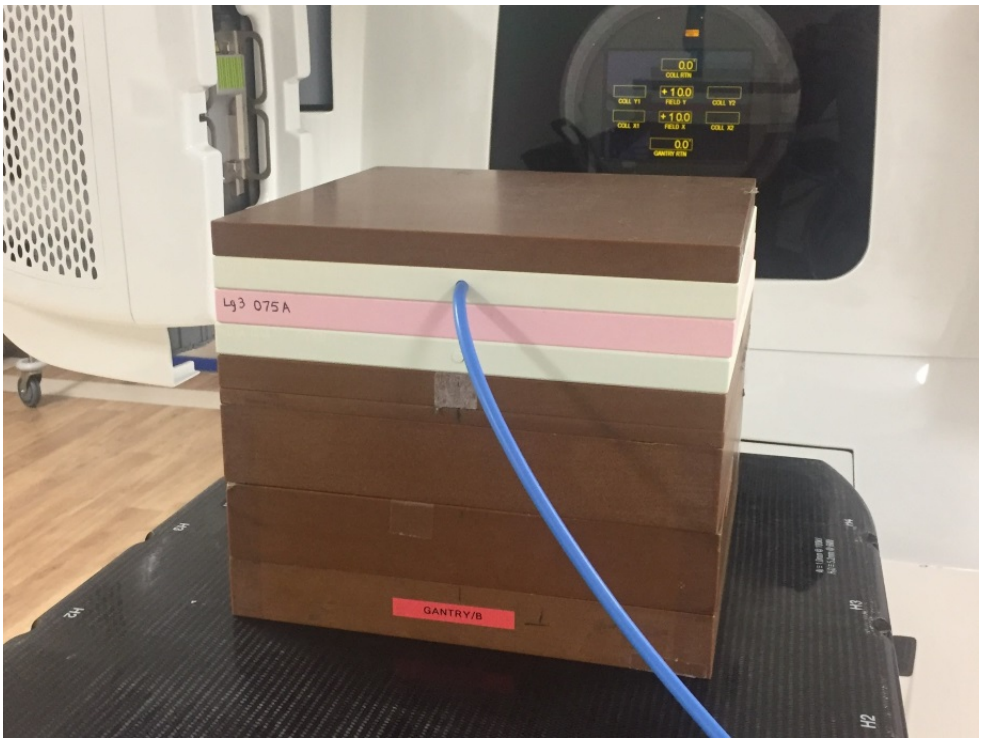

Fig. 5.2: The slab geometry set up with a 2 cm lung slab in slab 3.

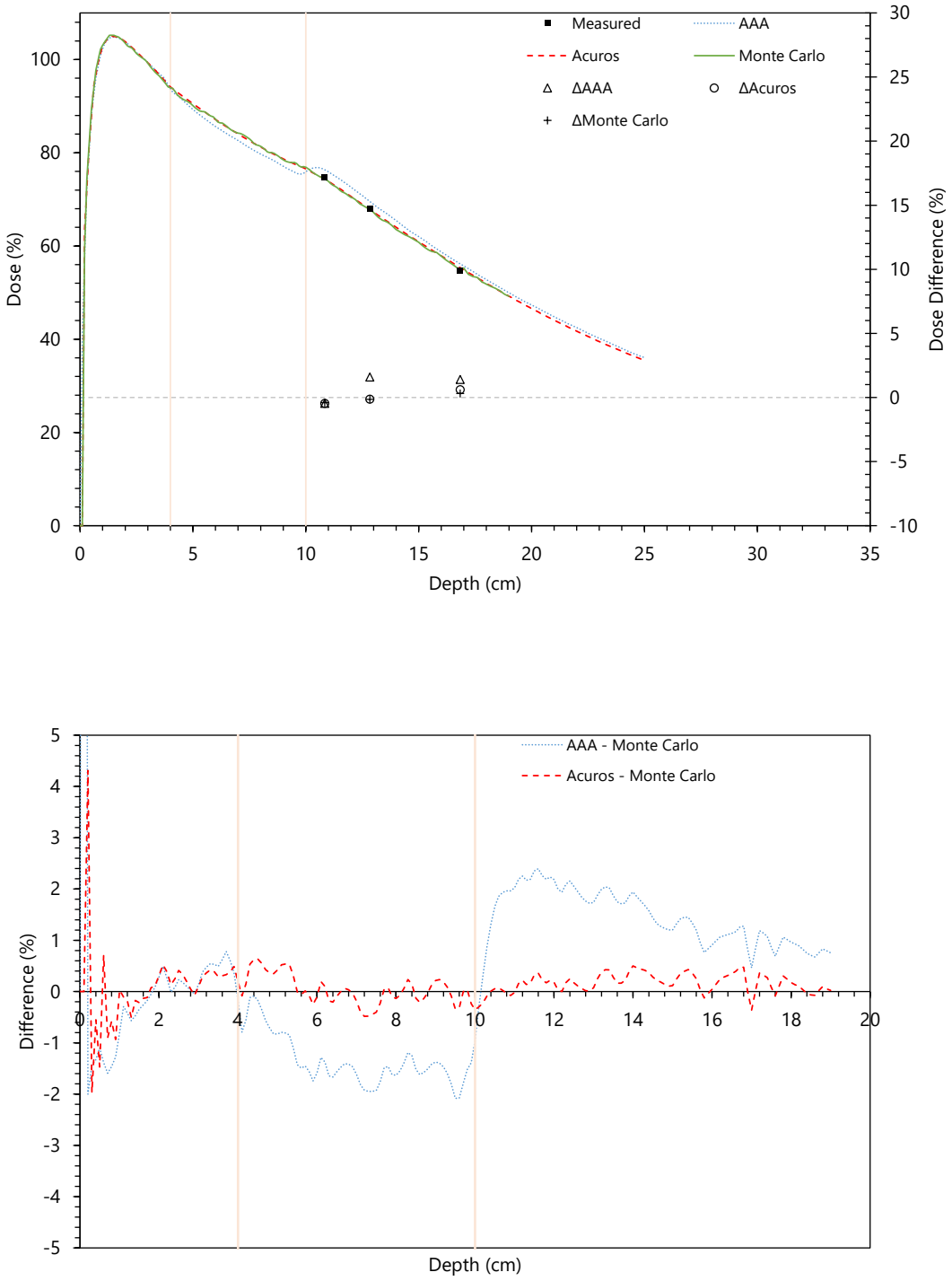

Fig. 5.3: Slab geometry tests with a 10 x 10 cm field involving a 6 cm slab of lung.

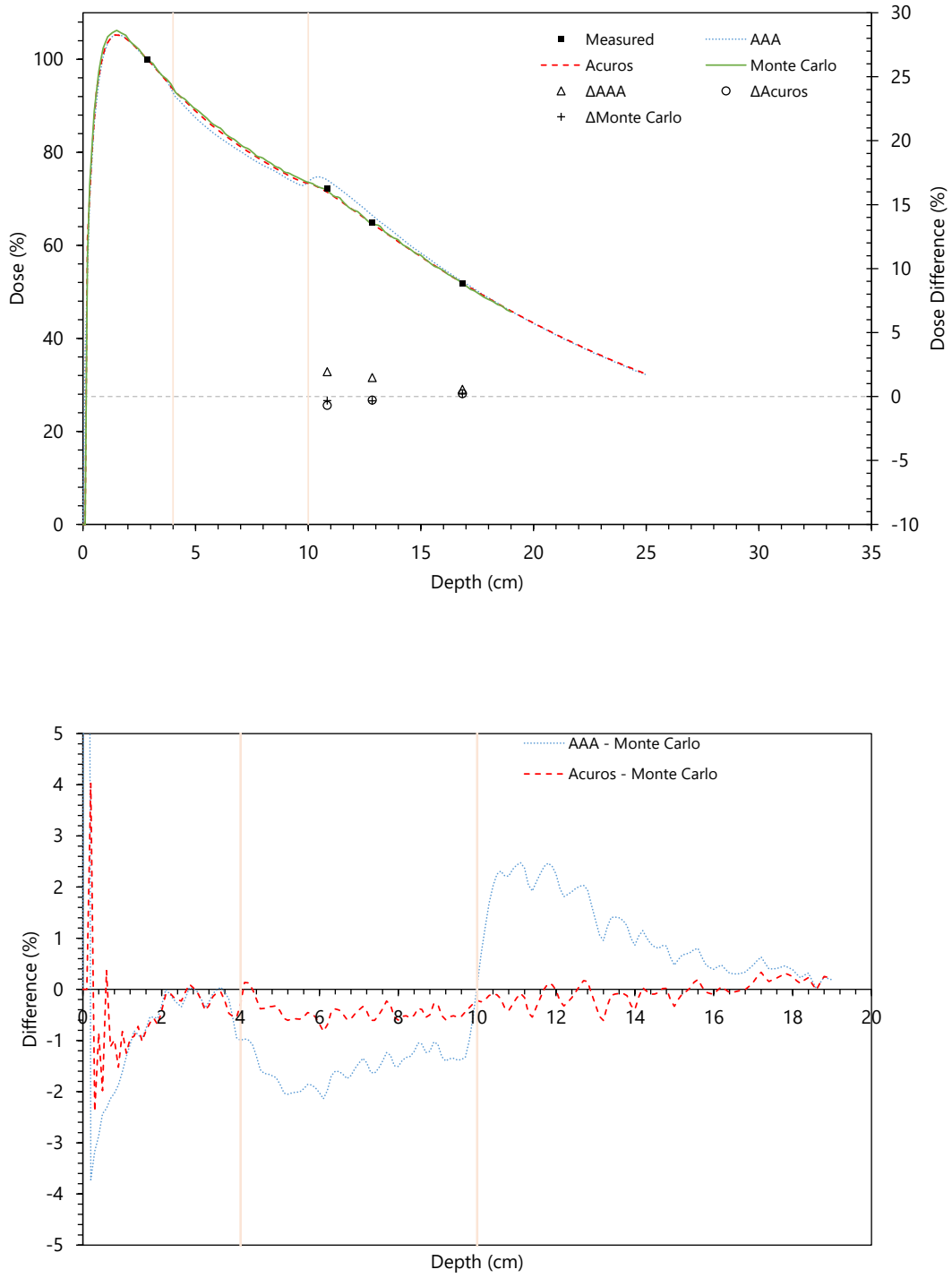

Fig. 5.4: Slab geometry tests with a 5 x 5 cm field involving a 6 cm slab of lung.

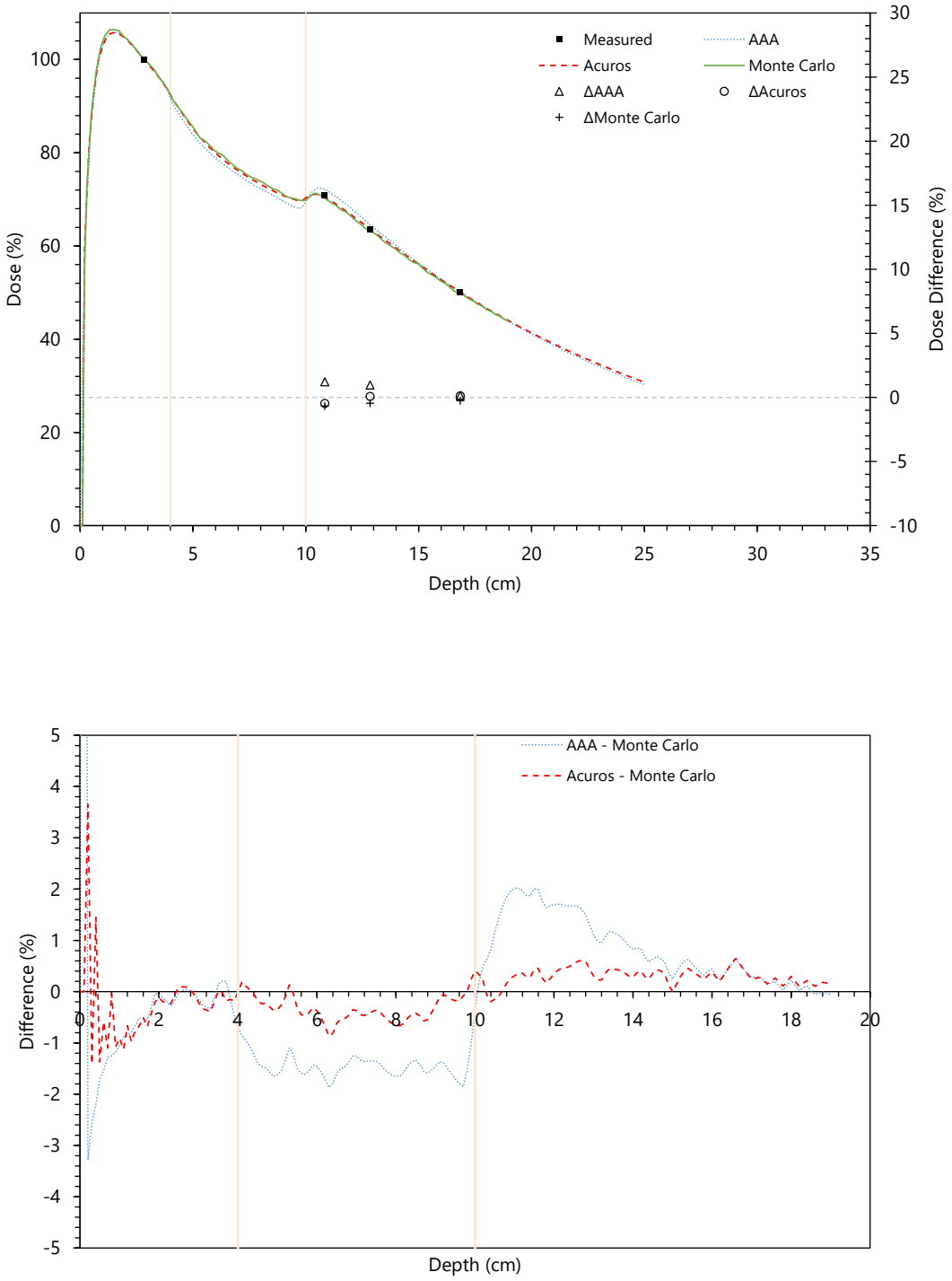

Fig. 5.5: Slab geometry tests with a 3 x 3 cm field involving a 6 cm slab of lung.

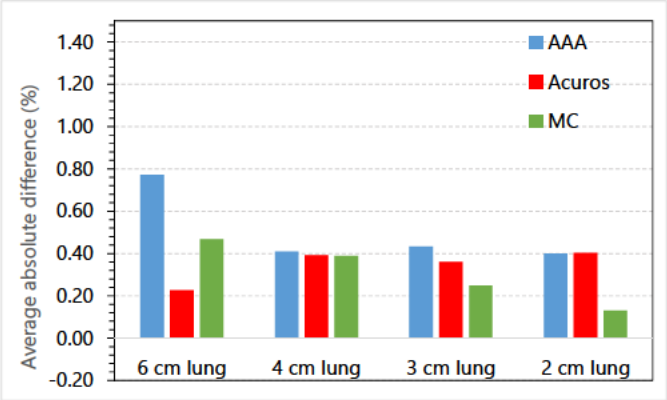

(a) 3 x 3 cm

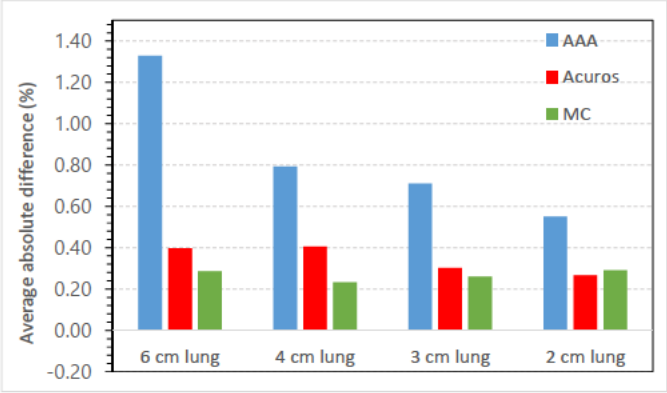

(b) 5 x 5 cm

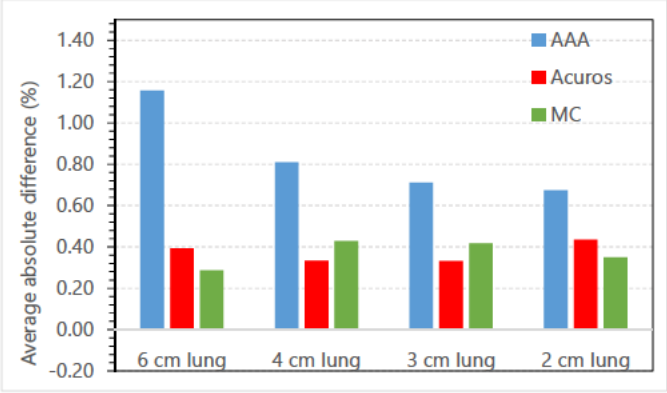

(c) 10 x 10 cm

Fig. 5.6: Average absolute differences from point dose measurements, distal to lung, for each algorithm with each figure averaged over a different field size. From top to bottom, the field sizes are 3 x 3 cm, 5 x 5 cm and 10 x 10 cm.

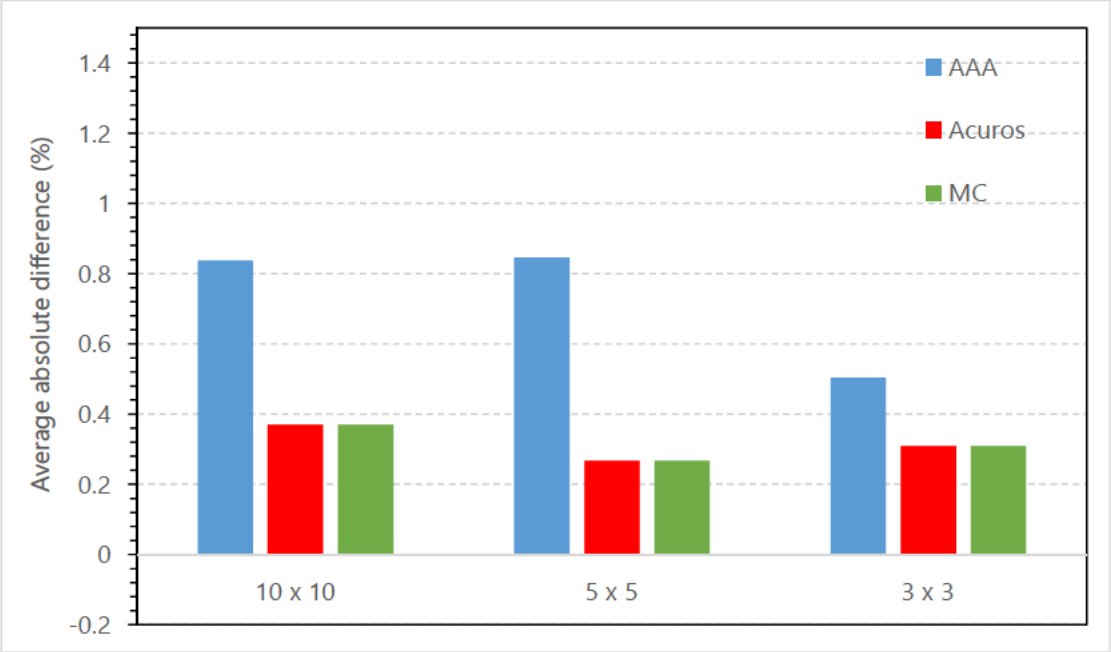

Fig. 5.7: Average absolute differences from point dose measurements, distal to lung, for each algorithm, averaged over all thicknesses of lung.

5.3 TecDoc 1583 tests

TecDoc 1583 [Vatnitsky and International Atomic Energy Agency, 2008] was used as a guide for constructing plans on the CIRS thorax phantom to determine Acuros and AAA accuracy in phantom geometry for various treatment fields. Point doses were measured with the PTW TW31010 ion chamber and the PTW Unidos electrometer. The chamber was exposed to a calibration dose of 250 cGy in solid water to determine cGy/nC on the day of measurement. Temperature and pressure were observed during the measurement period and found to be stable.

The eight cases are described in detail by Vatnitsky and International Atomic Energy Agency [2008] and are summarised here:

Case 1 10 x 10 cm field at gantry and collimator zero with 100 cm source-to-phantom distance.

Case 2 15 x 15 cm field with a 60 degree enhanced-dynamic-wedge and gantry and collimator at 90 degrees.

Case 3 15 x 10 cm field at gantry and collimator zero, collimated by MLCs.

Case 4 Four rectangular, jaw-defined fields incident at gantry angles 0, 90, 180 and 270 degrees.

Case 5 MLC defined field incident at gantry zero, collimator zero.

Case 6 MLC defined L-shape, with gantry at 45 degrees and collimator at 90 degrees.

Case 7 Four fields at gantry angles 0, 90, 180 and 270 degrees, with lateral 30 degree enhanced dynamic wedge fields.

Case 8 Two lateral rectangular fields with a non-coplanar beam at couch 270 degrees and gantry 30 degrees.

AAA calculations agreed well with all measurement points except for one case. The particular disagreement was with Case 2, which involved measuring at a point distal to a beam passing through lung. AAA calculated a dose at point 1 that was 4.2% higher than measured. This reflects a finding made by the Australian

Clinical Dosimetric Service (ACDS) during a national audit of radiotherapy clinics. The ACDS found that AAA calculated dose, on average, $2.9 \pm 1.2\%$ higher than measured in regions distal from lung-tissue [Dunn *et al.*, 2015]. The audit did not find a significant systematic offset in any other algorithms that were tested.

Acuros calculations agreed well with all measurement points except for Case 1 point 10. This point is inside the bone inhomogeneity. All doses were calculated as dose to water, and this discrepancy is likely due to the scaling of dose to medium to dose to water, in order to compare to measured data.

Averaged over all cases and all measurement points, AAA calculated dose 0.4 $\pm$ 0.4% higher than measured, while Acuros calculated dose 0.2 $\pm$ 0.2% lower than measured. Detailed results are shown in Appendix A.

5.4 Algorithm verifications on CT datasets

CT images were taken using a Philips Big Bore CT and the images were exported as DICOM files. The images were converted to a phantom through the ctcreate program that is distributed with DOSXYZnrc. The ctcreate program takes several inputs:

1. The format of the CT data, which was set to DICOM.
2. A text file that contains a list of all the DICOM images, one per line, in ascending Z order.
3. The x, y, z boundaries of the phantom that is created.
4. The voxel sizes of the phantom (set to 0.2 cm for each dimension).
5. A ramp definition which converts CT number to mass density and material. This was entered based on a scan of a CIRS electron density phantom and so matches the CT number to mass density ramp entered into Eclipse.

The CT ramp used for Acuros and Monte Carlo calculations is shown in Figure 5.8. When Acuros determines a material, if two density ranges overlap for two materials, Acuros will use an average material for the subsequent calculation [Varian, 2015]. For the most part, the materials overlap for Acuros and Monte Carlo calculations, however this is an additional source of uncertainty.

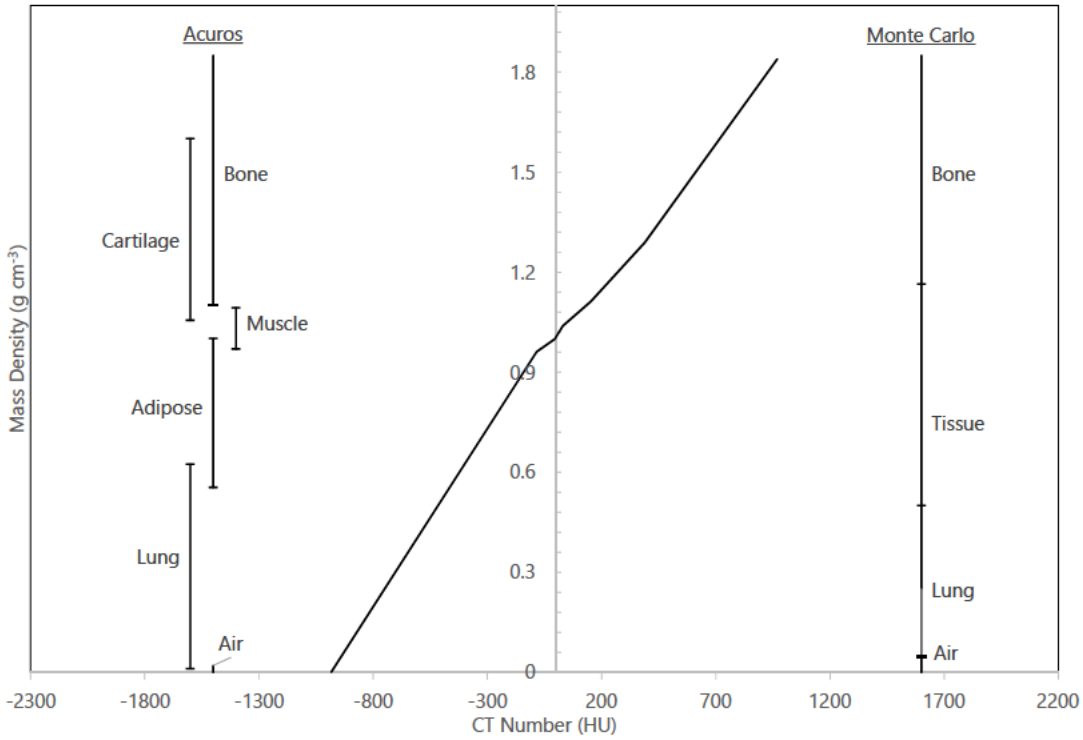

Fig. 5.8: CT Number to mass density conversion function used in both Acuros and Monte Carlo. The material bins for both Monte Carlo and Acuros are shown.

The program ctcreate reads the DICOM images and creates a .EGSPHANT file which can be read by DOSXYZnrc in order to perform the simulation.

In order to allow the creation of a large phantom, the file dosxyznrc_user_macros_mortan was modified to make $ IMAX, $ JMAX and $ KMAX larger and both DOSXYZnrc and ctcreate were recompiled.

Treatment plan parameters were converted from the DICOM coordinate system to the DOSXYZnrc coordinate system as per Schmitz *et al.* [2014].

For the conversion, the following rotation matrices are used:

$$R_x(\theta) = \begin{bmatrix} 1 & 0 & 0 \\ 0 & \cos(\theta) & -\sin(\theta) \\ 0 & \sin(\theta) & cos(\theta) \end{bmatrix} \tag{5.1}$$

$$R_y(\theta) = \begin{bmatrix} \cos(\theta) & 0 & sin(\theta) \\ 0 & 1 & 0 \\ -sin(\theta) & 0 & \cos(\theta) \end{bmatrix} \tag{5.2}$$

$$R_z(\theta) = \begin{bmatrix} \cos(\theta) & -\sin(\theta) & 0 \\ \sin(\theta) & \cos(\theta) & 0 \\ 0 & 0 & 1 \end{bmatrix} \tag{5.3}$$

The rotation of the DOSXYZnrc coordinates is then performed by the matrix T, where T is

$$T = R_y(\theta_T)Rz(\theta_G)R_y(\pi/2 - \theta_C)R_x(\pi/2) \tag{5.4}$$

where θ_G is the beam gantry angle, θ_T is the linac table rotation angle and θ_C is the linac collimator angle.

DOSXYZnrc source positions are defined using a polar coordinate system centred on the isocentre. To obtain the polar coordinates used in DOSXYZnrc, the initial beam vector (0, 0, -1) is transformed by T:

$$\vec{V} = \begin{bmatrix} X \\ Y \\ Z \end{bmatrix} = T \begin{bmatrix} 0 \\ 0 \\ -1 \end{bmatrix}. \tag{5.5}$$

The angles in the polar coordinate system are then

$$\theta = \arccos(-Z) \tag{5.6}$$

$$\phi = \arctan\left(\frac{-Y}{-X}\right) \tag{5.7}$$

$$\phi_{coll} = \frac{3\pi}{2} - \theta_C - \arctan\left(\frac{-\sin(\theta_T)\cos(\theta_G)}{\cos(\theta_T)}\right). \tag{5.8}$$

θ, ϕ and ϕ_{coll} are the angles defining the source position in the DOSXYZnrc polar coordinate system and the BEAMnrc collimator angle. Verification of the transformation matrices are shown in Appendix C.3.

For computing treatment plans in EGSnrc, the SYNCJAWS component was used in the BEAMnrc linac definition. This component enables the user to input jaw settings which change over the course of the simulation. The contribution from each jaw setting is determined from the index, which ranges from 0 to 1. The index is related to the number of monitor units for each beam. The index is cumulative so

that the first jaw definition has an index equal to its proportion of 'beam on' time and the last jaw setting has an index equal to 1.0.

Jaw opening positions of the BEAMnrc jaw component were calculated by $x = \frac{z}{SAD}X$, where z is the distance from the source to the jaw opening, SAD is the source-to-axis distance of the linear accelerator, and X is the size of the jaw opening projected down to the isocentre of the linac.

For treatment plan calculations, DOSXYZnrc source 21 was used. This source allows a compiled BEAMnrc shared library to be used as a source from multiple angles in a single computation. The angles, isocentre and distance from the source are defined for each treatment beam. The $muIndex(i)$ for each control point, which represents the fraction of the total number of incident primary histories delivered up to control point i, synchronises with the BEAMnrc SYNCJAWS component [Walters *et al.*, 2005]. A computer program was written in order to convert treatment plans in the DICOM format to the required input files for Monte Carlo calculations.

Similarly to the slab geometry tests above, Monte Carlo calculated dose was scaled from dose to medium to dose to water by multiplying the dose in each voxel by the stopping power ratio (medium to water) of the material in the image in the same voxel.

5.4.1 CIRS thorax dataset calculations

A 3 cm diameter PTV was drawn in the left lung in Eclipse. A program was written to convert the Eclipse regions of interests (ROIs) into a DICOM image dataset, which could then be used as input for a Monte Carlo calculation A plan was calculated with AAA, Acuros and DOSXYZnrc involving a right-left 4 x 4 cm field and an anterior-posterior 4 x 4 cm field, with their isocentres at the centre of the PTV.

Profiles and dose-volume-histograms were calculated with DicomViewer (Appendix C.2). The Acuros profile is in better agreement with the Monte Carlo profile through the central slice of the PTV (Figures 5.9 and 5.10). In both the left lung and the PTV, Acuros dose-volume-histograms were closer to the Monte Carlo dose-volume-histograms than AAA (Figures 5.11 and 5.12).

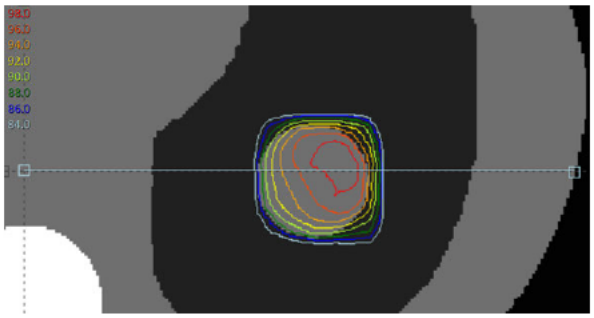

Fig. 5.9: The CIRS thorax phantom dataset, shown with Monte Carlo calculated dose. The blue line shows the location of the profiles seen in Figure 5.10, below.

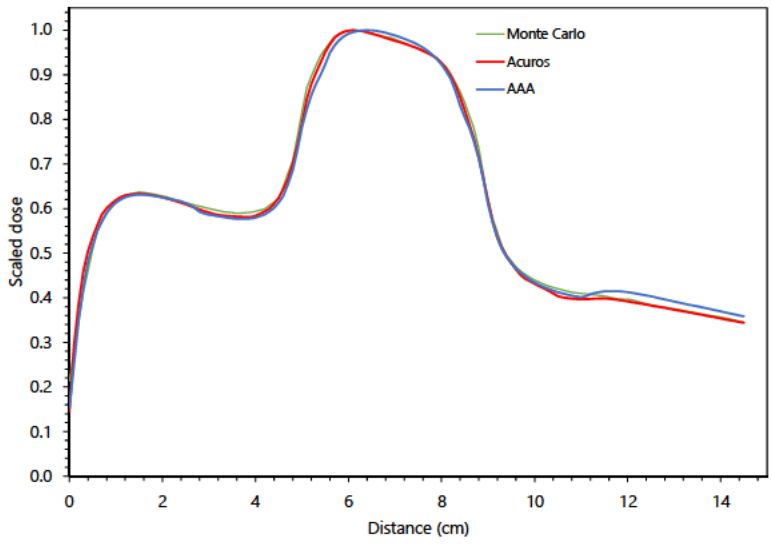

Fig. 5.10: A dose profile from right to left through the PTV in the CIRS thorax phantom.

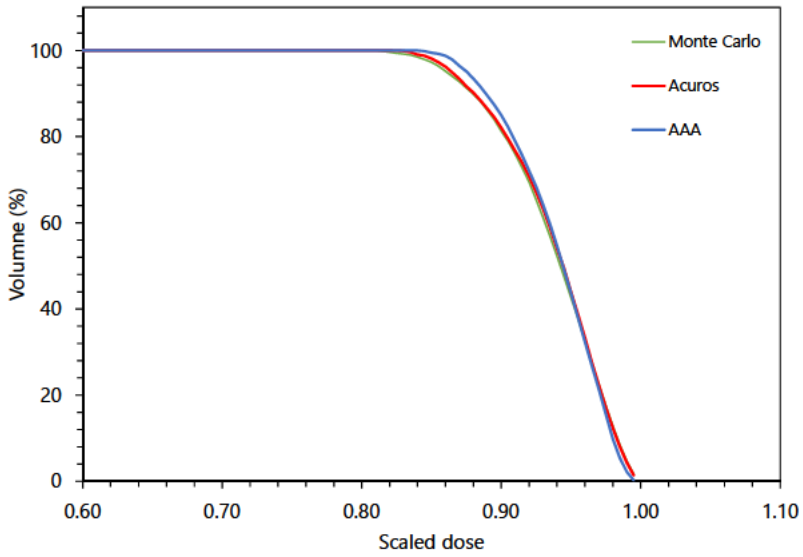

Fig. 5.11: Dose-volume-histograms in the PTV of the CIRS thorax phantom for AAA, Acuros and Monte Carlo calculated dose distributions.

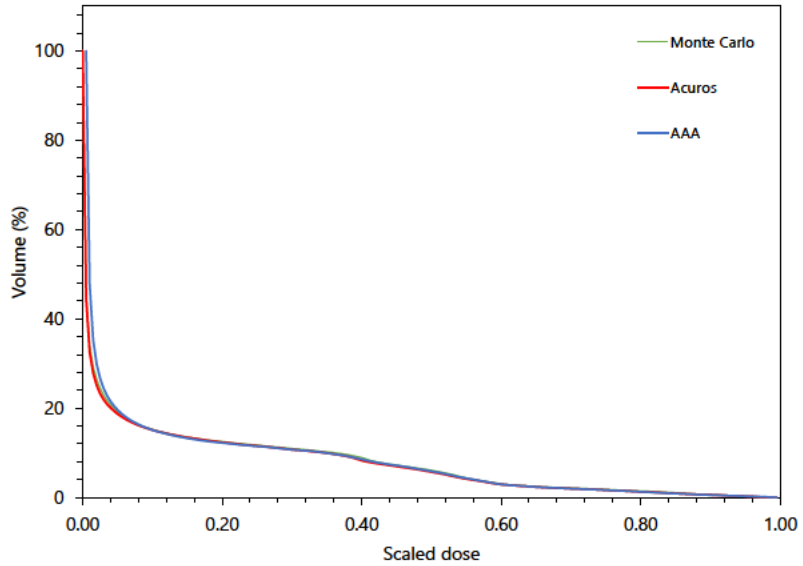

Fig. 5.12: Dose-volume-histograms in the left lung of the CIRS thorax phantom for AAA, Acuros and Monte Carlo calculated dose distributions.

5.4.2 Patient dataset calculations

SBRT lung patients were chosen for calculations due to the prevalence of reasonably small fields and due to the presence of low density material, which has typically been a difficult scenario for dose calculation.

Previous clinical plans were chosen and patient CT datasets converted to an .EGSPHANTOM file. MLCs were removed in the plan, since the MLCs were not commissioned for the Monte Carlo model created for this study. The plan was exported and input into DOSXYZnrc in the appropriate format, using the BEAMnrc component SYNCJAWS. Monte Carlo calculations were compared to AAA, Acuros and CCC for three plans. Gamma analysis was performed with the software SNC Patient (Sun Nuclear, Melbourne FL). The gamma analysis was performed with a threshold of 20%. The effect of the 20% threshold, as implemented in SNC Patient, is to remove dose points from the analysis when they are less than 20% of the normalisation dose, except for points inside a complex or bifurcated field. All dose distributions were normalised to the maximum dose.

The CT datasets used in this section are shown in Figure 5.13.

Plan 1

Plan 1 was a 12 field SBRT lung plan with multiple non-coplanar beams. A comparison for an axial plane through the PTV was made (Figures 5.14 - 5.16). The gamma agreements to Monte Carlo (2%, 2 mm) for Acuros, AAA and CCC were 100.0%, 98.8% and 99.5% respectively. Both AAA and CCC underestimated the dose in a section of the PTV relative to Monte Carlo. CCC appears to underestimate the dose in the PTV. Calculations with heterogeneity corrections turned off agree well between Acuros, AAA and CCC (100% gamma pass rate with the criteria 2%, 2 mm). This suggests that any disagreements between the algorithms are due to the algorithm implementation and radiation transport in low density mediums.

Plan 2

Plan 2 was a 10 field SBRT plan with multiple non-coplanar beams. A comparison for an axial plane through the PTV was made (Figures 5.17 - 5.19). The gamma agreements to Monte Carlo (2%, 2 mm) for Acuros, AAA and CCC were 98.3%,

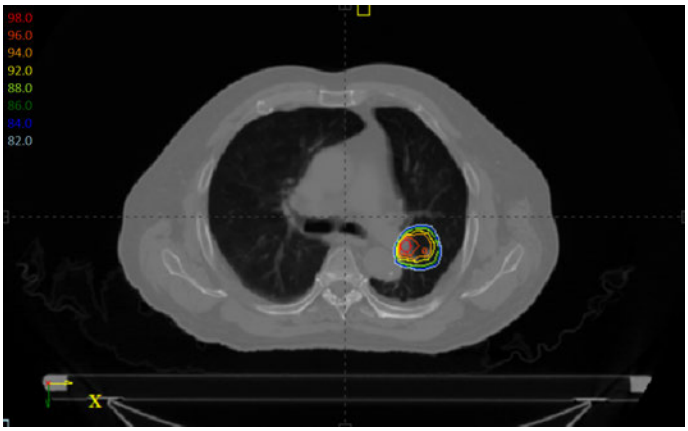

(a) Plan 1 CT Dataset and normalised dose distribution.

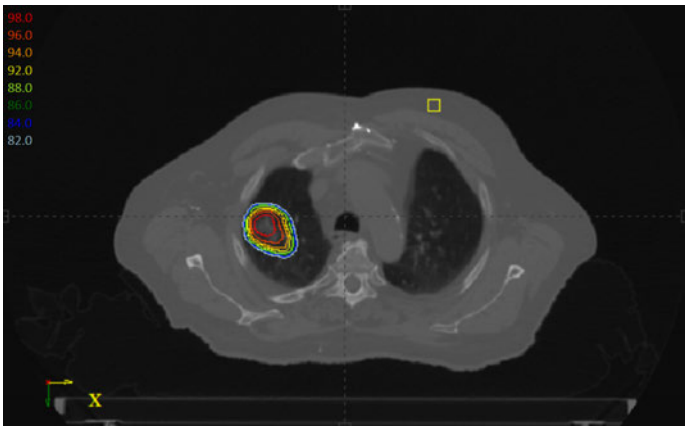

(b) Plan 2 CT Dataset and normalised dose distribution.

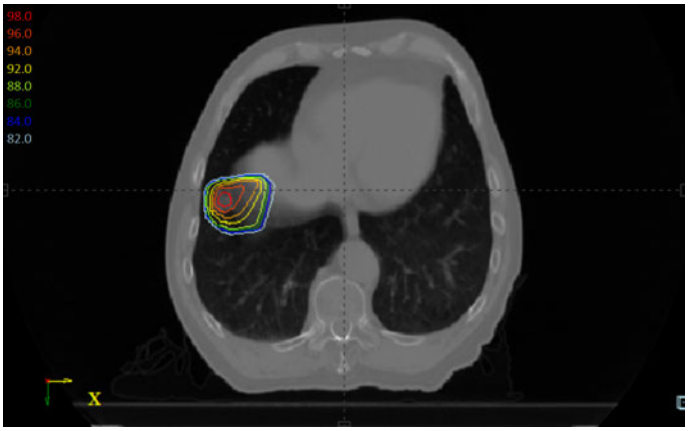

(c) Plan 3 CT Dataset and normalised dose distribution.

Fig. 5.13: The CT Datasets used in this section, with the calculated dose distribution shown

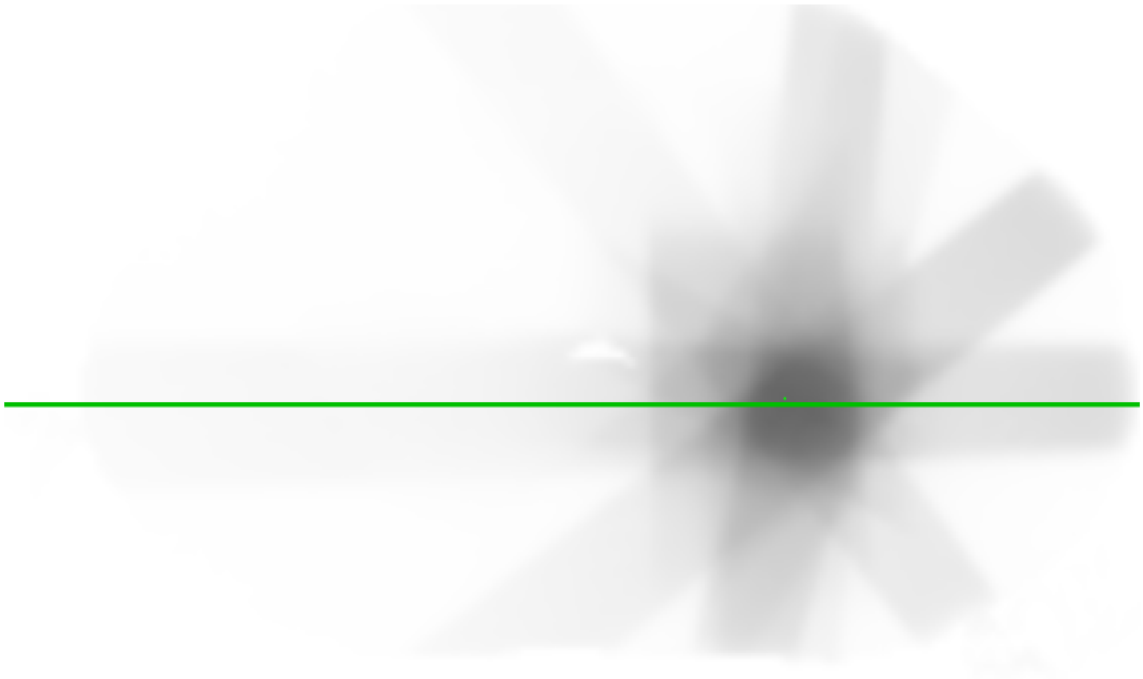

(a) A plane through the PTV in plan 1.

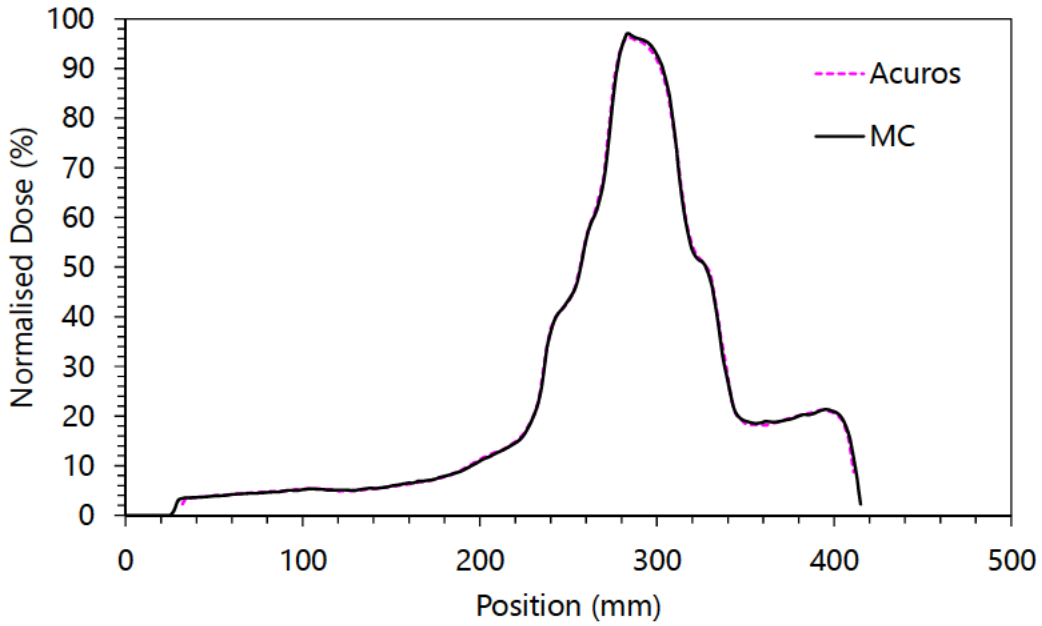

(b) A dose profile through the PTV in plan 1. The pink profile shows dose calculated by Acuros. The black profile shows dose calculated by Monte Carlo.

Fig. 5.14: Acuros vs Monte Carlo calculated dose for plan 1.

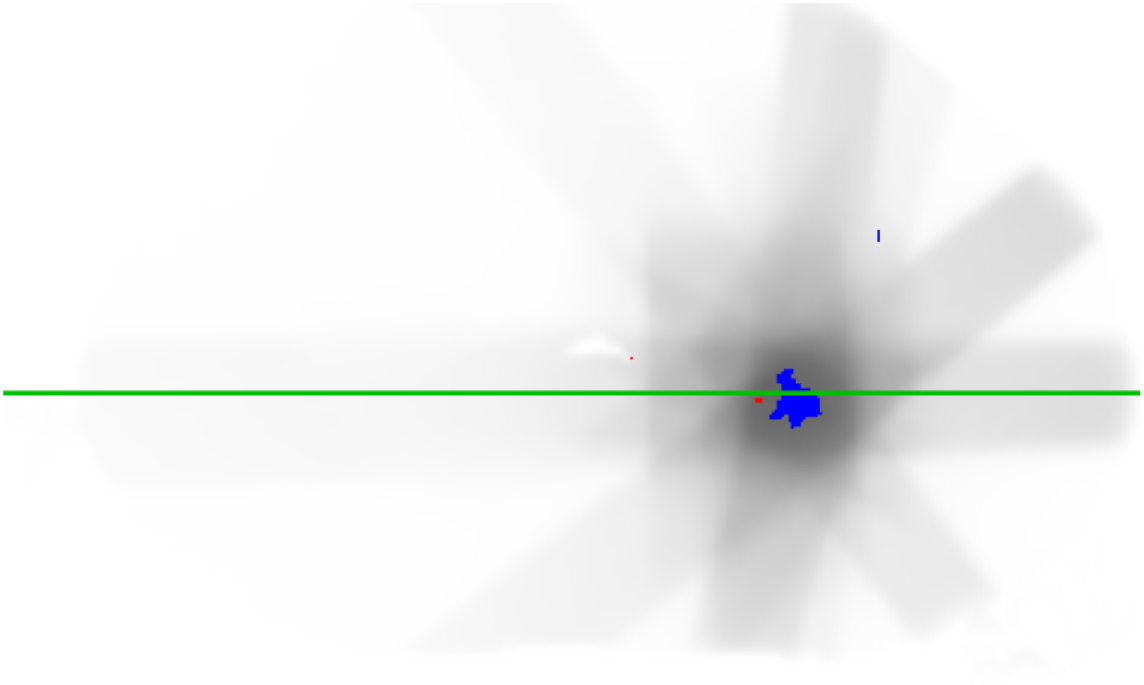

(a) A plane through the PTV in plan 1. The red and blue areas show regions where gamma is greater than 1, with the red showing calculated dose higher relative to Monte Carlo, and blue showing calculated dose lower relative to Monte Carlo.

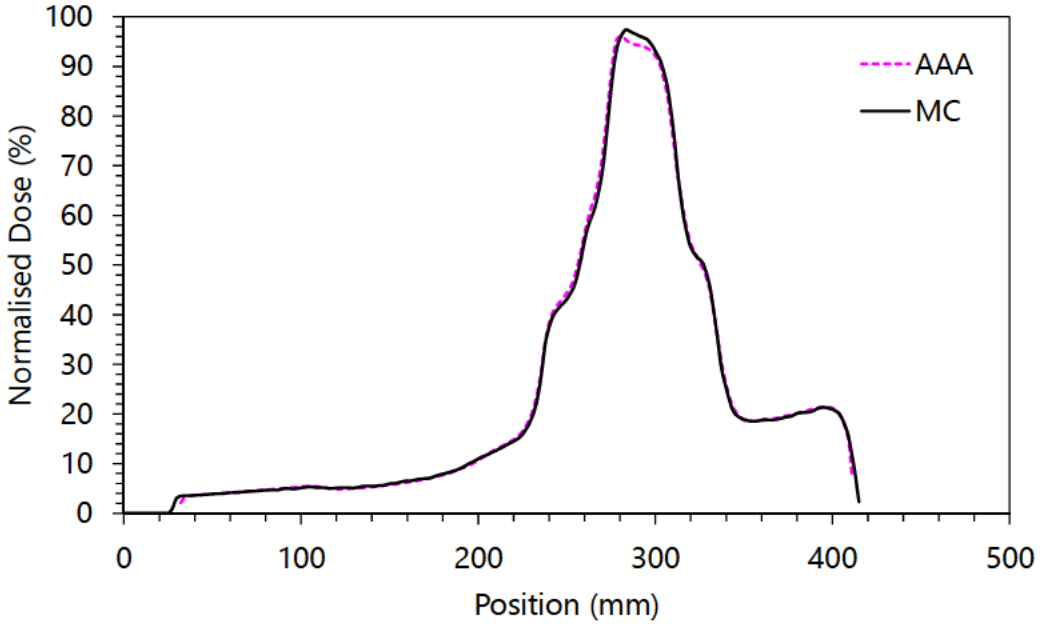

(b) A dose profile through the PTV in plan 1. The pink profile shows dose calculated by AAA. The black profile shows dose calculated by Monte Carlo.

Fig. 5.15: AAA vs Monte Carlo calculated dose for plan 1.

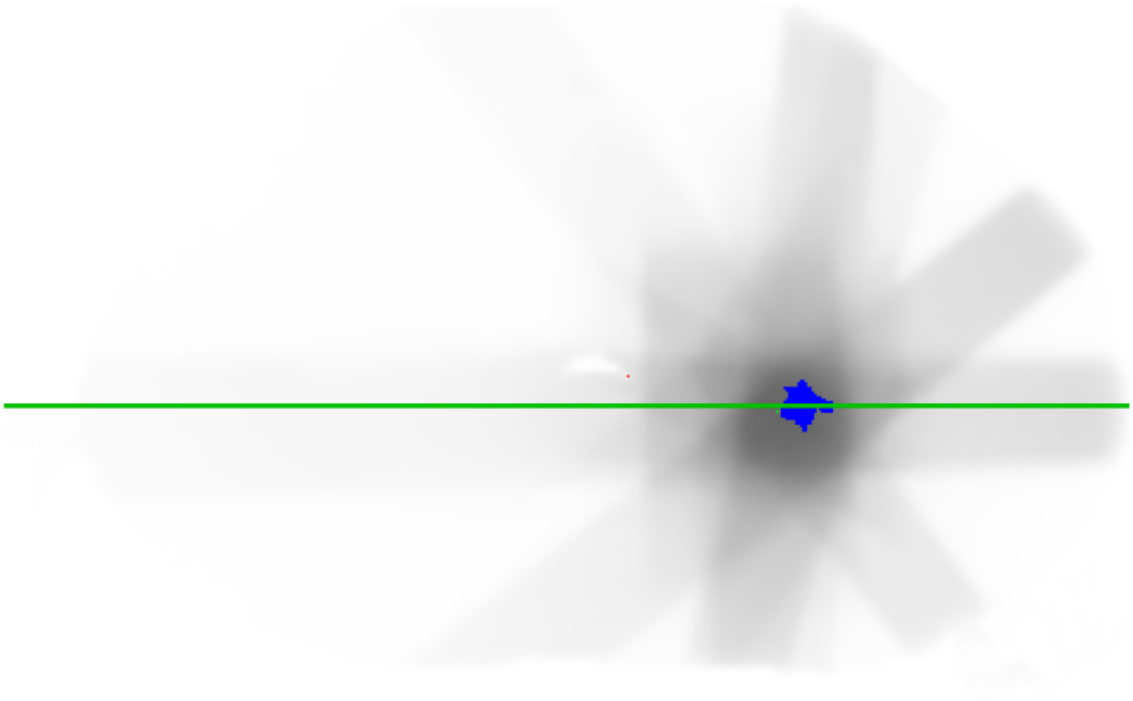

(a) A plane through the PTV in plan 1. The blue areas show regions where gamma is greater than 1 and the calculated dose is lower relative to Monte Carlo.

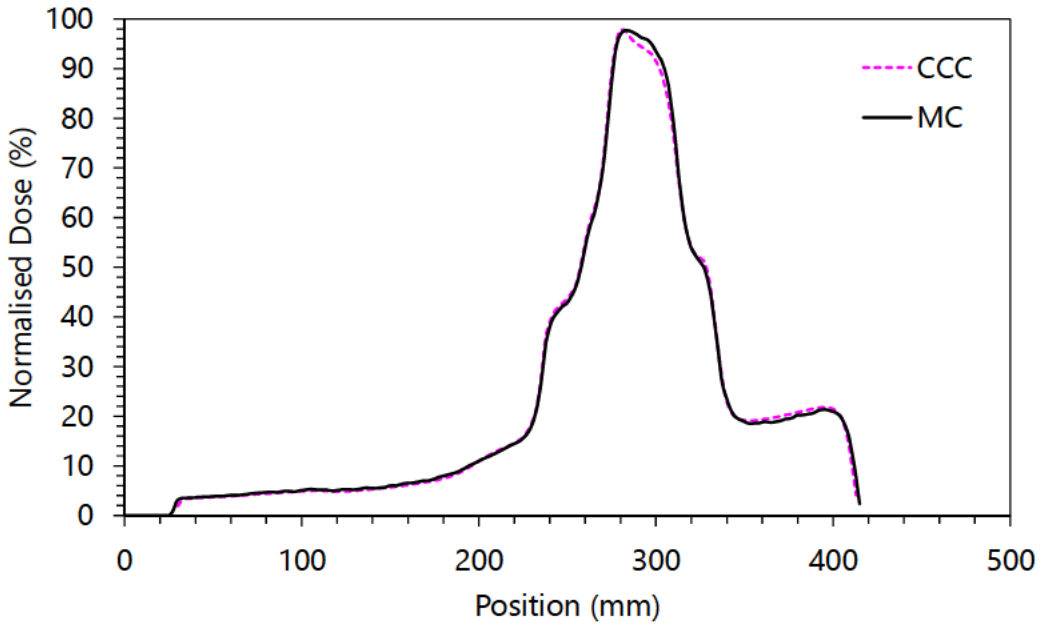

(b) A dose profile through the PTV in plan 1. The pink profile shows dose calculated by CCC. The black profile shows dose calculated by Monte Carlo.

Fig. 5.16: CCC vs Monte Carlo calculated dose for plan 1.

97.8% and 98.1% respectively. In this case the air dose was not zeroed in Monte Carlo calculations. This resulted in some disagreements outside of the body contour. Agreement in the PTV was good in all cases. As the dose was not zeroed outside the body contour in the Monte Carlo calculations, the gamma pass rate of CCC is somewhat misleading, as CCC has excellent agreement with Monte Carlo inside the body.

Plan 3

Plan 3 was a 10 field SBRT plan with multiple non-coplanar beams. A comparison for an axial plane through the PTV was made (Figures 5.20 - 5.22). The gamma agreements to Monte Carlo (2%, 2 mm) for Acuros, AAA and CCC were 95.8%, 96.8% and 92.5% respectively. As in plan 2, the air dose was not zeroed in Monte Carlo calculations, resulting in some disagreements outside of the body contour. Agreement in the PTV was good for all algorithms.

The average gamma pass rates (2%, 2 mm) in the three plans for Acuros, AAA and CCC are 98.0%, 97.8% and 96.7% respectively.

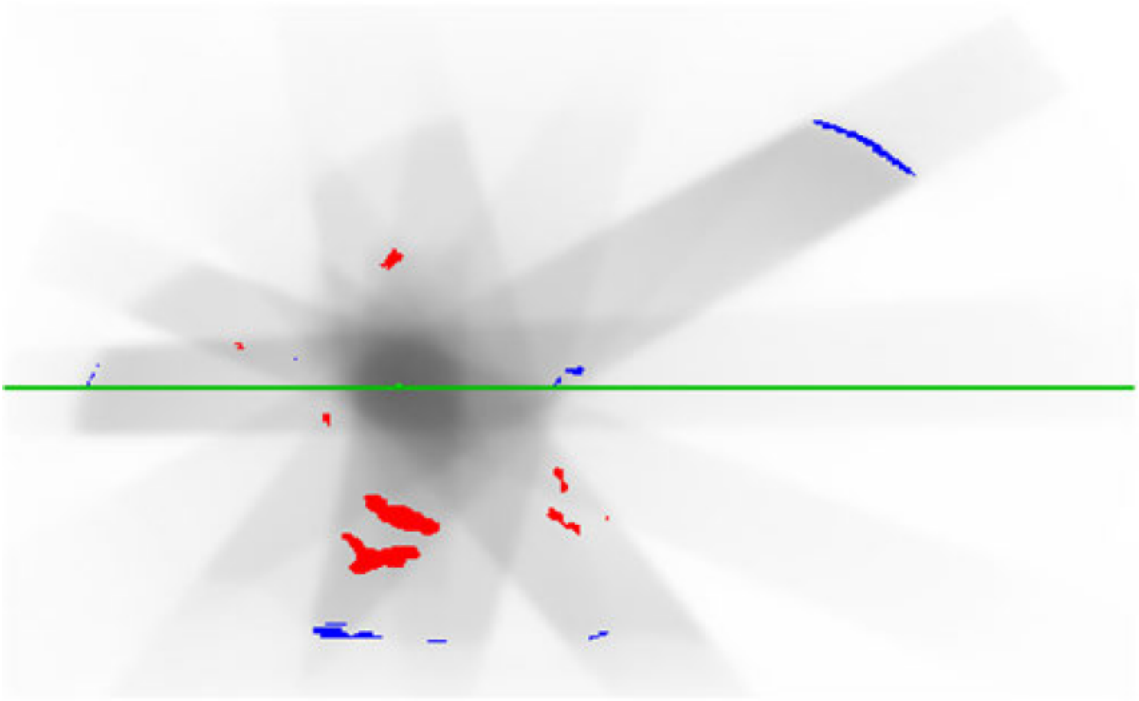

(a) A plane through the PTV in plan 2. The red and blue areas show regions where gamma is greater than 1, with the red showing calculated dose higher relative to Monte Carlo, and blue showing calculated dose lower relative to Monte Carlo.

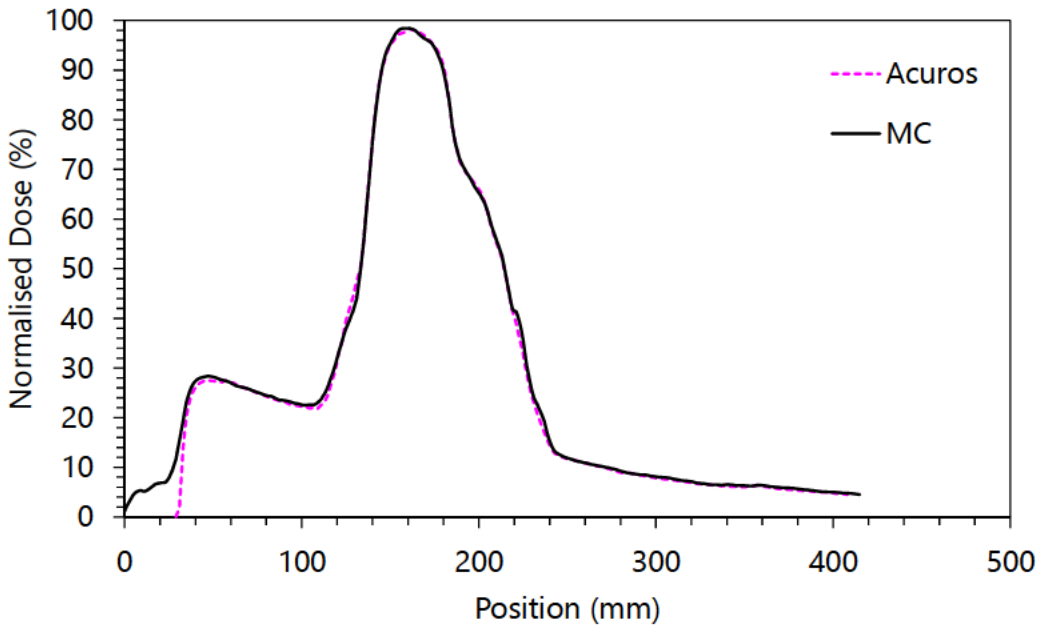

(b) A dose profile through the PTV in plan 2. The pink profile shows dose calculated by Acuros. The black profile shows dose calculated by Monte Carlo.

Fig. 5.17: Acuros vs Monte Carlo calculated dose for plan 2.

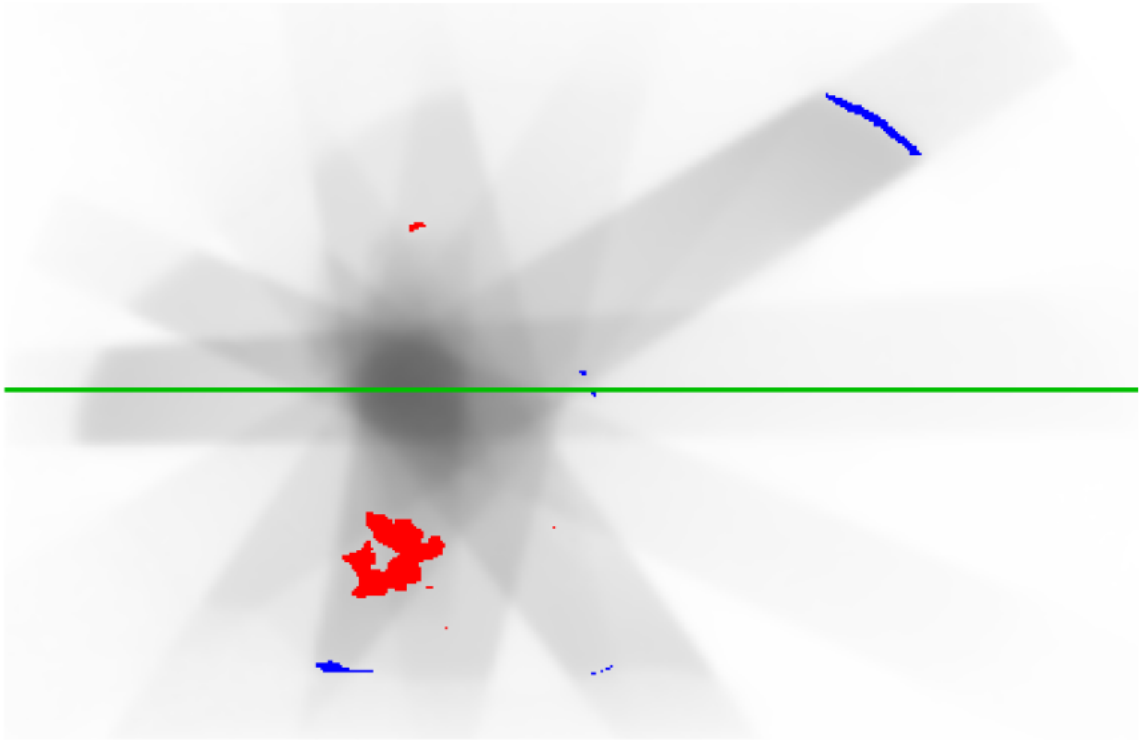

(a) A plane through the PTV in plan 2. The red and blue areas show regions where gamma is greater than 1, with the red showing calculated dose higher relative to Monte Carlo, and blue showing calculated dose lower relative to Monte Carlo.

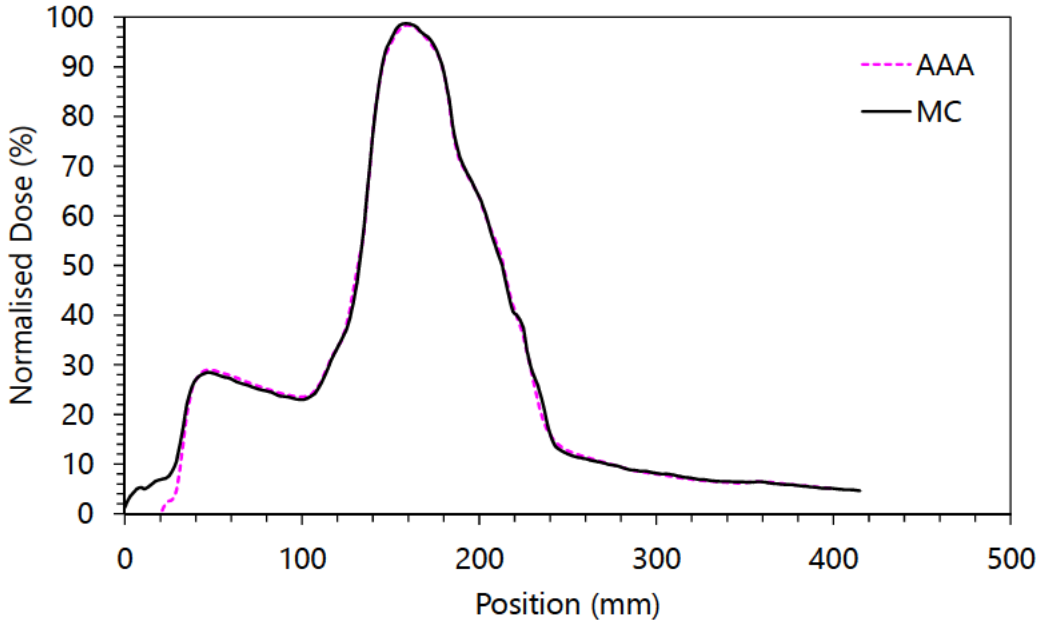

(b) A dose profile through the PTV in plan 2. The pink profile shows dose calculated by AAA. The black profile shows dose calculated by Monte Carlo.

Fig. 5.18: AAA vs Monte Carlo calculated dose for plan 2.

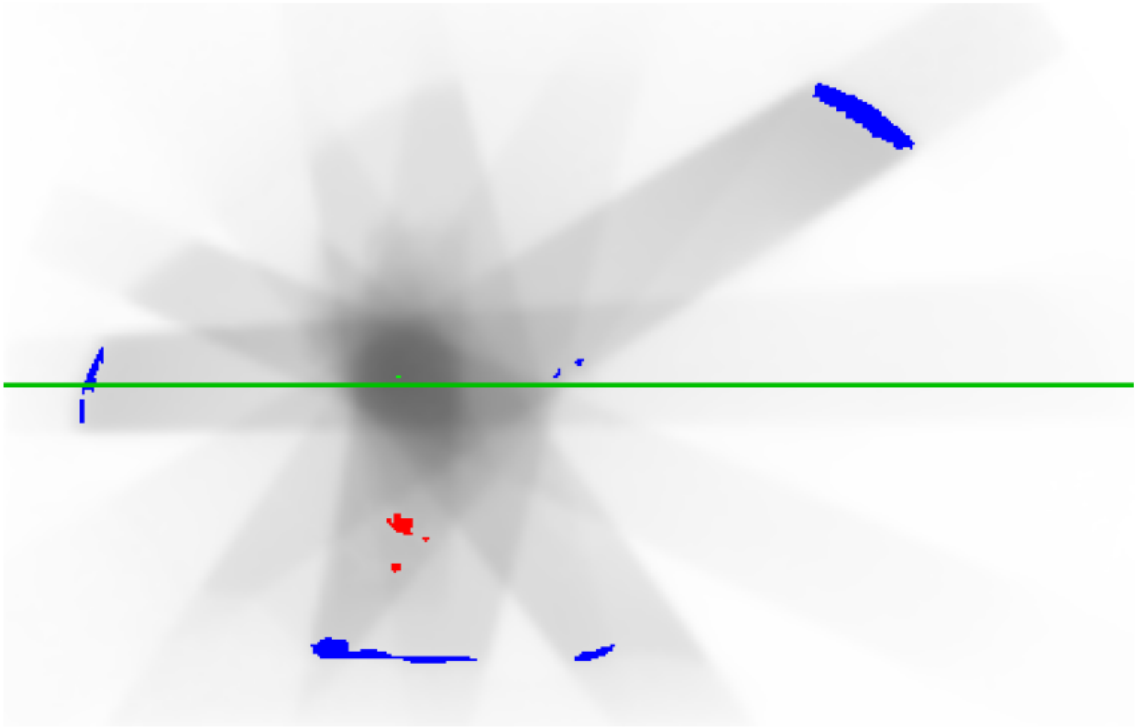

(a) A plane through the PTV in plan 2. The red and blue areas show regions where gamma is greater than 1, with the red showing calculated dose higher relative to Monte Carlo, and blue showing calculated dose lower relative to Monte Carlo.

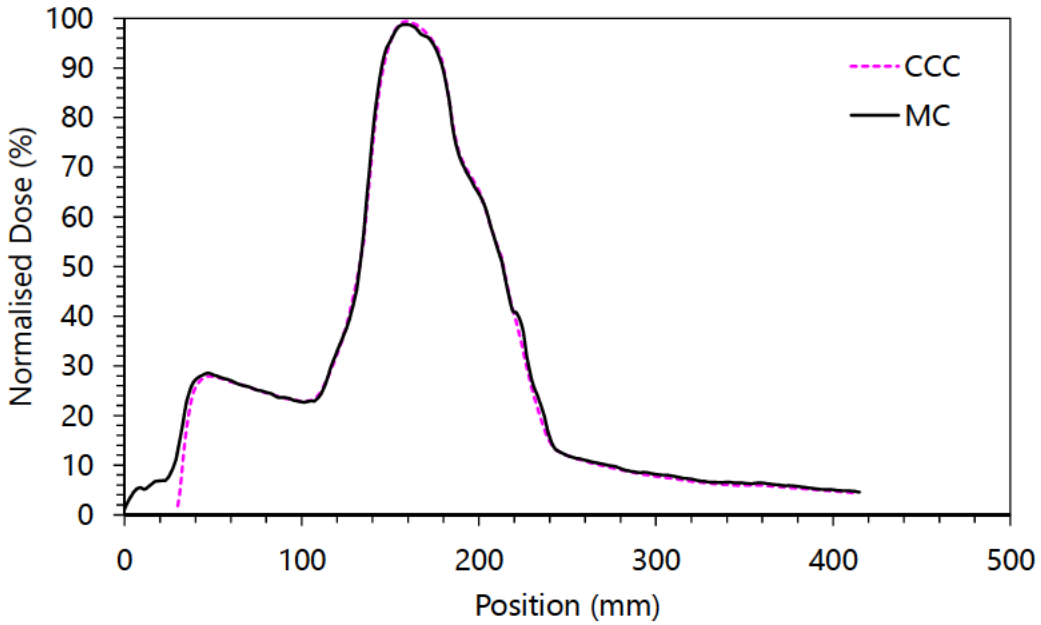

(b) A dose profile through the PTV in plan 2. The pink profile shows dose calculated by CCC. The black profile shows dose calculated by Monte Carlo.

Fig. 5.19: CCC vs Monte Carlo calculated dose for plan 2.

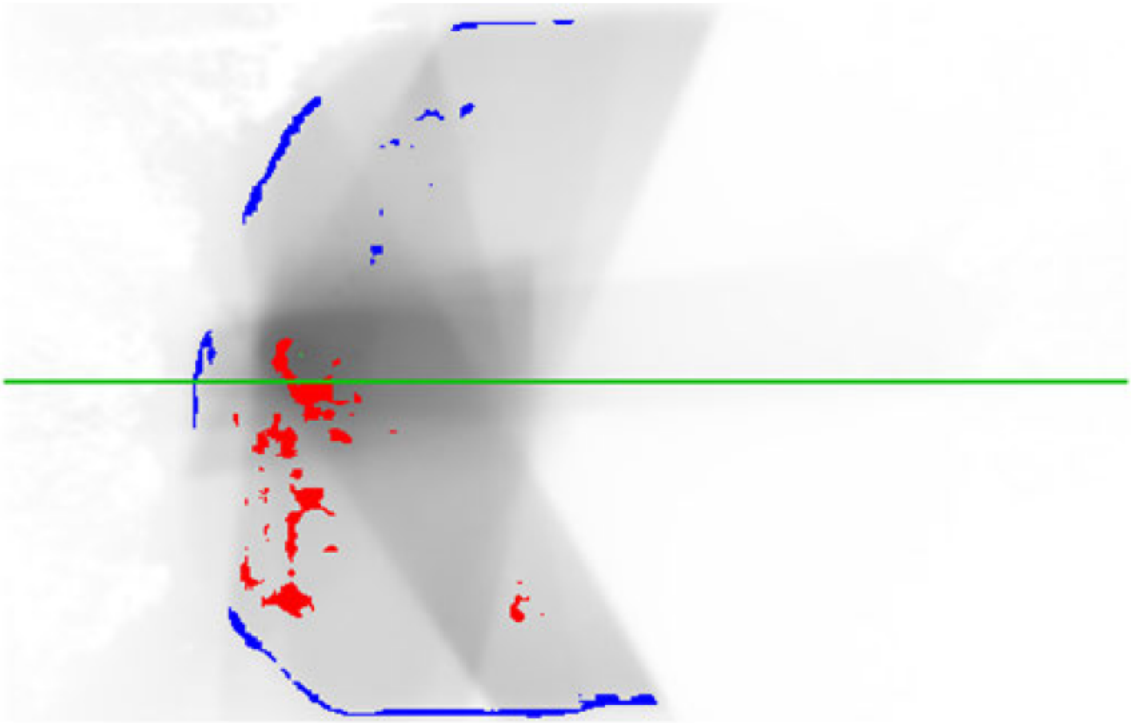

(a) A plane through the PTV in plan 3. The red and blue areas show regions where gamma is greater than 1, with the red showing calculated dose higher relative to Monte Carlo, and blue showing calculated dose lower relative to Monte Carlo.

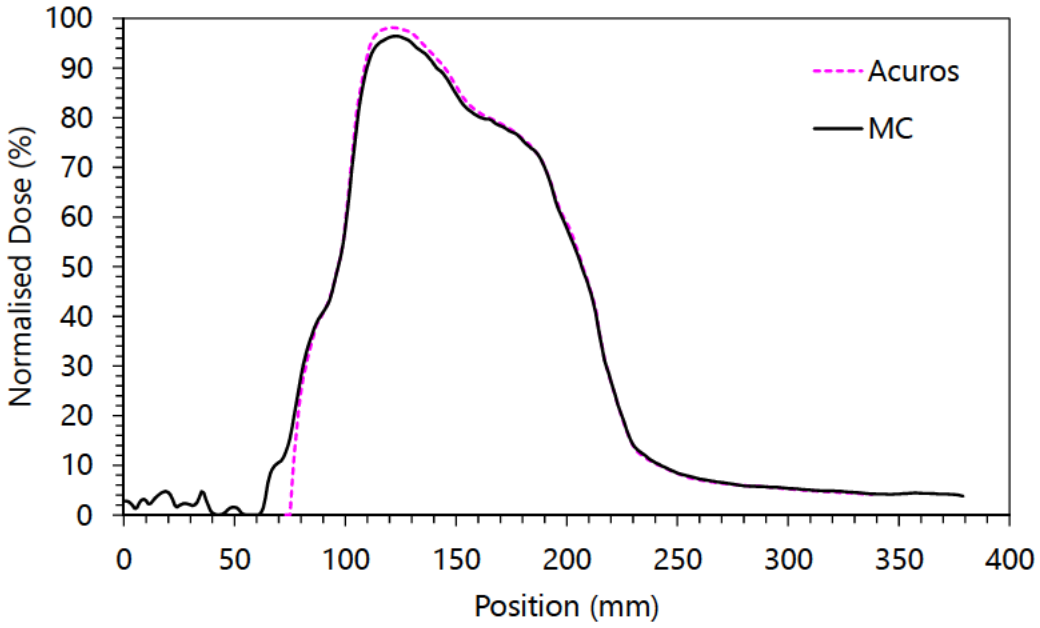

(b) A dose profile through the PTV in plan 3. The pink profile shows dose calculated by Acuros. The black profile shows dose calculated by Monte Carlo.

Fig. 5.20: Acuros vs Monte Carlo calculated dose for plan 3.

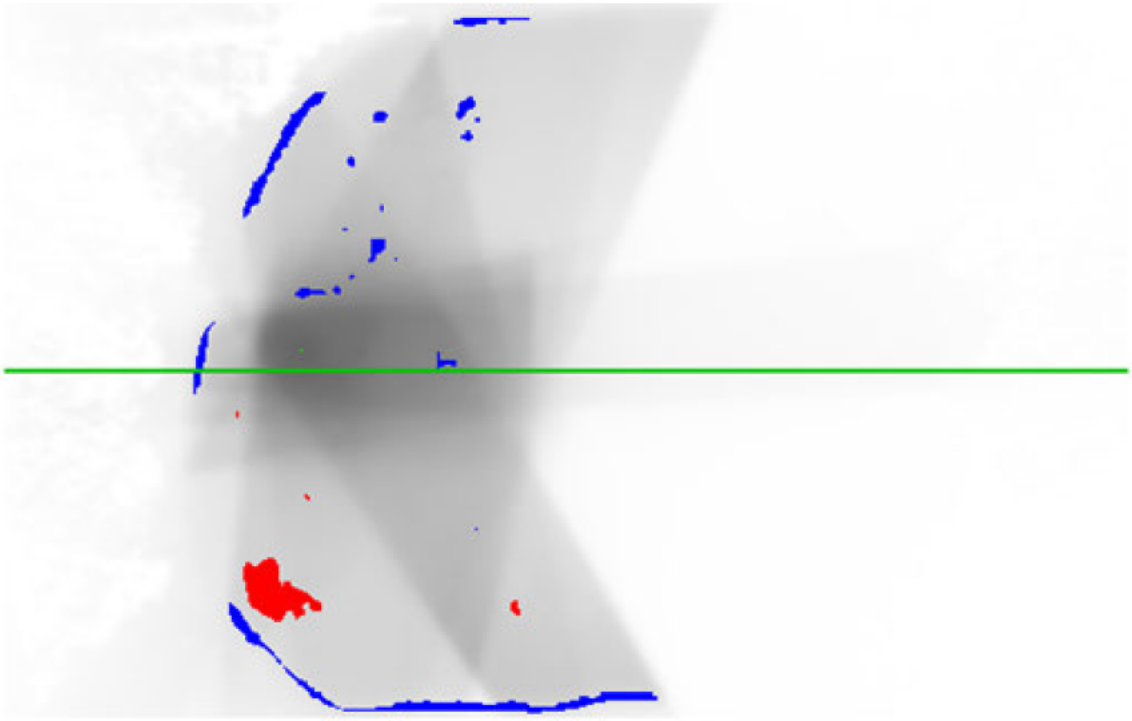

(a) A plane through the PTV in plan 3. The red and blue areas show regions where gamma is greater than 1, with the red showing calculated dose higher relative to Monte Carlo, and blue showing calculated dose lower relative to Monte Carlo.

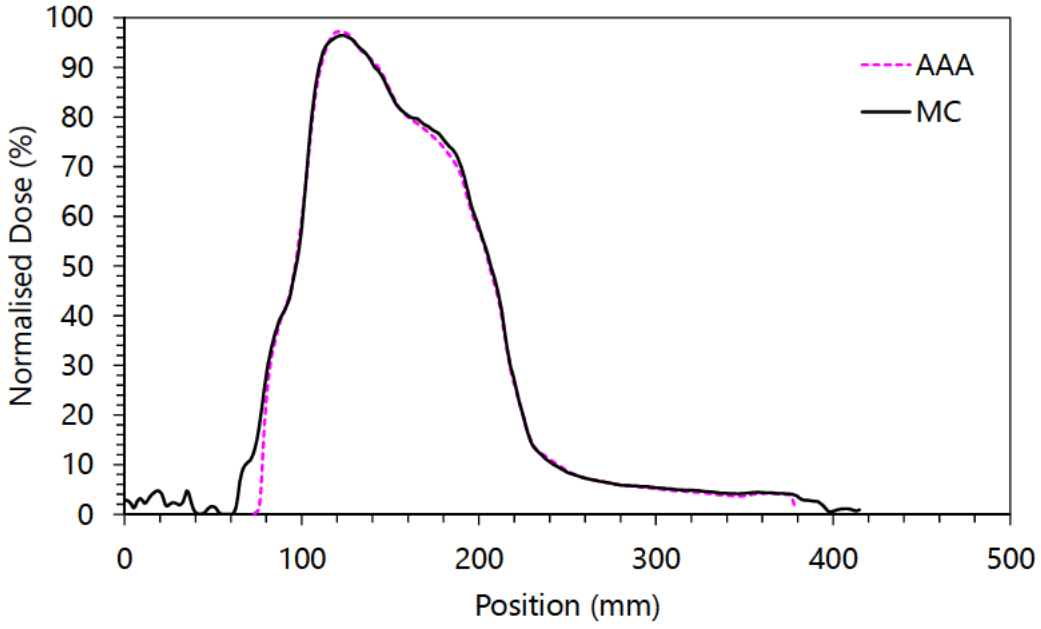

(b) A dose profile through the PTV in plan 3. The pink profile shows dose calculated by AAA. The black profile shows dose calculated by Monte Carlo.

Fig. 5.21: AAA vs Monte Carlo calculated dose for plan 3.

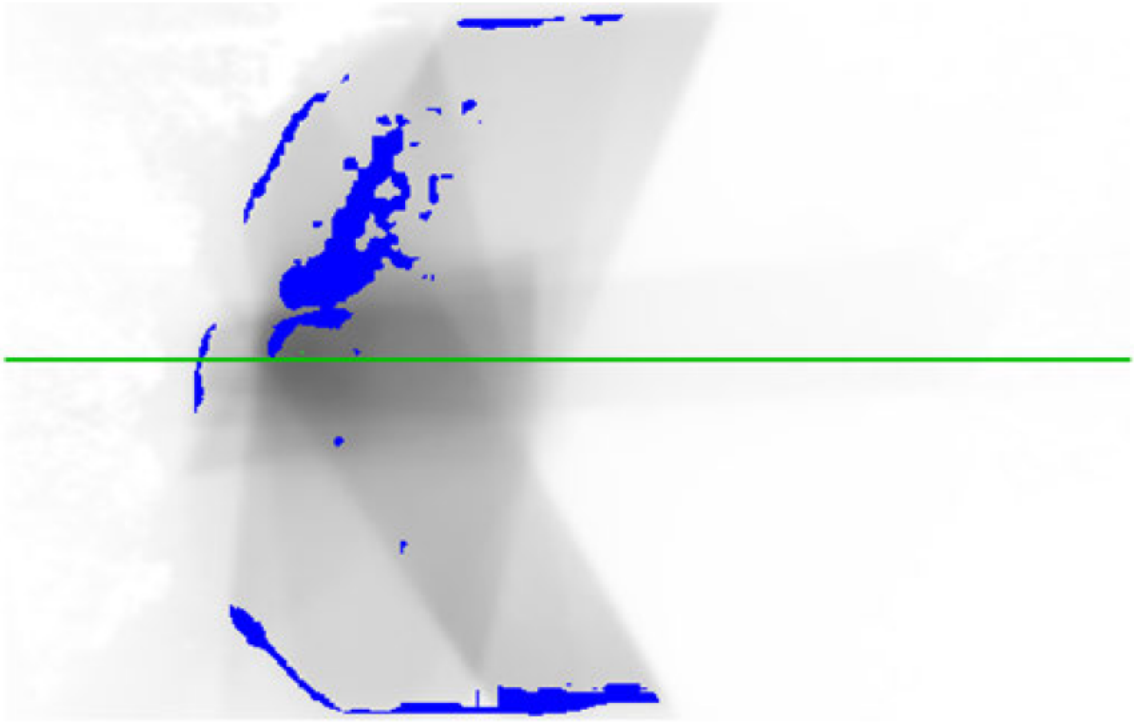

(a) A plane through the PTV in plan 3. The blue areas show regions where gamma is greater than 1 and the calculated dose is lower relative to Monte Carlo.

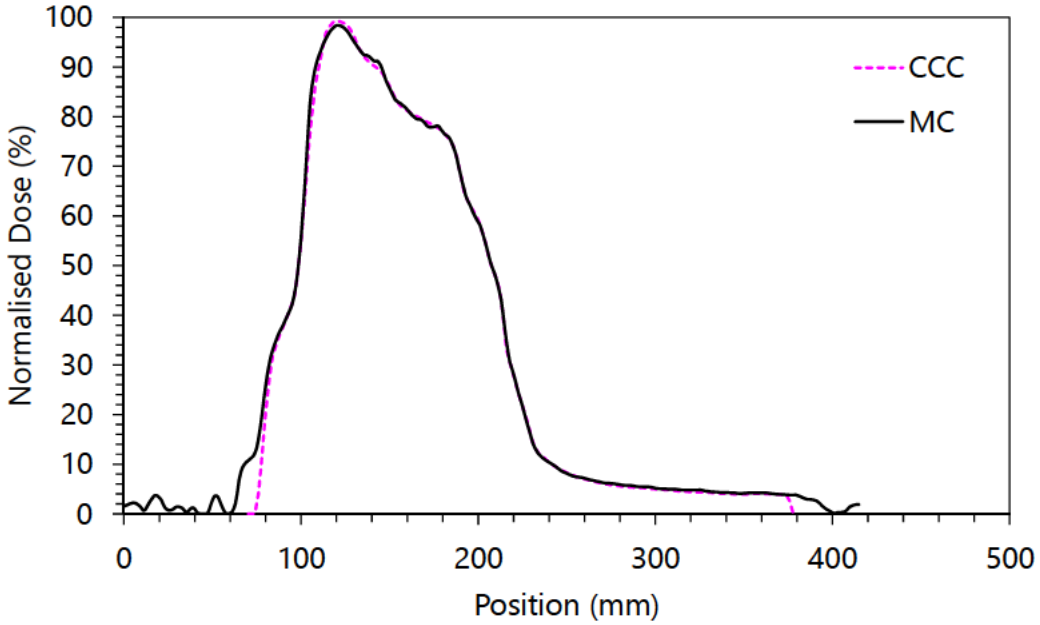

(b) A dose profile through the PTV in plan 3. The pink profile shows dose calculated by CCC. The black profile shows dose calculated by Monte Carlo.

Fig. 5.22: CCC vs Monte Carlo calculated dose for plan 3.

6. DISCUSSION AND CONCLUSION

6.1 Discussion

This thesis has examined the accuracy of the LBTE solver Acuros XB. When compared to measurements or dose distributions calculated by Monte Carlo, dose calculated using Acuros agreed more closer than that calculated using AAA in most cases.

In slab geometry tests, Acuros agrees much more closely to Monte Carlo dose calculations than AAA. As the thickness of the inhomogeneity decreases, each algorithm agrees more closely with the measured dose. This is in agreement with the literature and is an intuitive result. A counter-intuitive result is that as the field size decreases from 10 x 10 cm^2 to 3 x 3 cm^2, AAA calculations agree better with measured dose. Smaller fields in low density regions exhibit a loss of electronic equilibrium and so it is expected that they would be more difficult to model for most dose calculation algorithms. A possible explanation for this effect is that it is a result of two opposite errors in the dose calculation. In all cases, AAA overestimates the rebuild-up of dose in the region distal to lung. In the 3 x 3 cm^2 field, the algorithm is likely overestimating the loss of dose due to electronic equilibrium more significantly than at the other field sizes. Because of this underestimation of dose before the lung-water interface in the small field, the effect of the overestimation of the rebuild-up is reduced and the resulting dose is closer to measured than what would be expected. Further work, outside the scope of this thesis, could be undertaken to investigate this discrepancy.

The consistent overestimation of dose calculated by AAA distal to lung inhomogeneities could potentially result in lower tumour control probabilities for treatment sites distal to lung. The systematic offset is shown in this report by the TecDoc 1583 tests, with AAA calculating higher doses distal to lung in Case 2. This finding is mirrored by a national audit performed by the ACDS [Dunn *et al.*, 2015]. The

offset is also found in the slab inhomogeneity tests in this report. Dunn *et al.* [2015] speculates that the reason for the offset is that "AAA uses Gaussian functions to describe the mean heterogeneous effect in four lateral directions, instead of over 4π, as implemented in Acuros XB."

In calculations on CT datasets, Acuros had a higher average gamma pass rate than CCC and AAA when compared to the Monte Carlo calculation. This agrees with both Han *et al.* [2013], who compared the AAA and Acuros to film measurements in a thorax phantom, and Fogliata *et al.* [2011a], who compared AAA and Acuros to Monte Carlo in virtual phantoms using 2D gamma comparisons. In order to provide a statistically significant result, future work could involve calculations using a larger number of clinical plans. Future work could also include the use of MLCs in static or IMRT/VMAT fields.

There are some limitations in this study with respect to the comparison of the three dose calculation algorithms. Since this thesis compares three algorithms with three different beam models, it is difficult to differentiate when an algorithm has a better beam model or when it calculates radiation transport more accurately. To remedy this somewhat, many calculations were performed in simple slab geometry, for field sizes that agree well in water phantom calculations.

Another limitation is the effect of dose normalisation in Monte Carlo calculated dose. As there is some statistical variation in dose from voxel to voxel due to the finite number of particles simulated, dose normalisation to a single point may result in a large difference in isodoses and DVHs. Large numbers of histories were used in the Monte Carlo calculations to remove some of this uncertainty.

A final uncertainty in the dose comparisons made in this study is the conversion of dose from dose to the medium to dose to water. In the case of Monte Carlo, the dose in each voxel is scaled by an amount based on the material in that voxel. The number of materials is limited to four: air, lung, tissue and bone. While this likely encapsulates the majority of the materials present in a CT scan of a patient, the HU thresholds between these materials may not match those that Acuros uses. Stopping power ratios to water calculated by Siebers *et al.* [2000] are used in this thesis. These values are relatively depth-independent on the central beam axis but may differ in shielded regions where there is a larger proportion of low-energy scattered radiation.

6.2 Conclusion

Acuros XB has been shown to calculate dose in different geometries with comparable accuracy to Monte Carlo calculations. In the majority of cases presented here, Acuros dose distributions match Monte Carlo dose distributions more closely than AAA, however the difference is mostly small. In almost all cases where the algorithm computes radiation dose in or distal to lung, Acuros computes dose which matches measured and Monte Carlo calculated dose better than AAA.

Appendices

Appendix A

EXTENDED SLAB GEOMETRY RESULTS

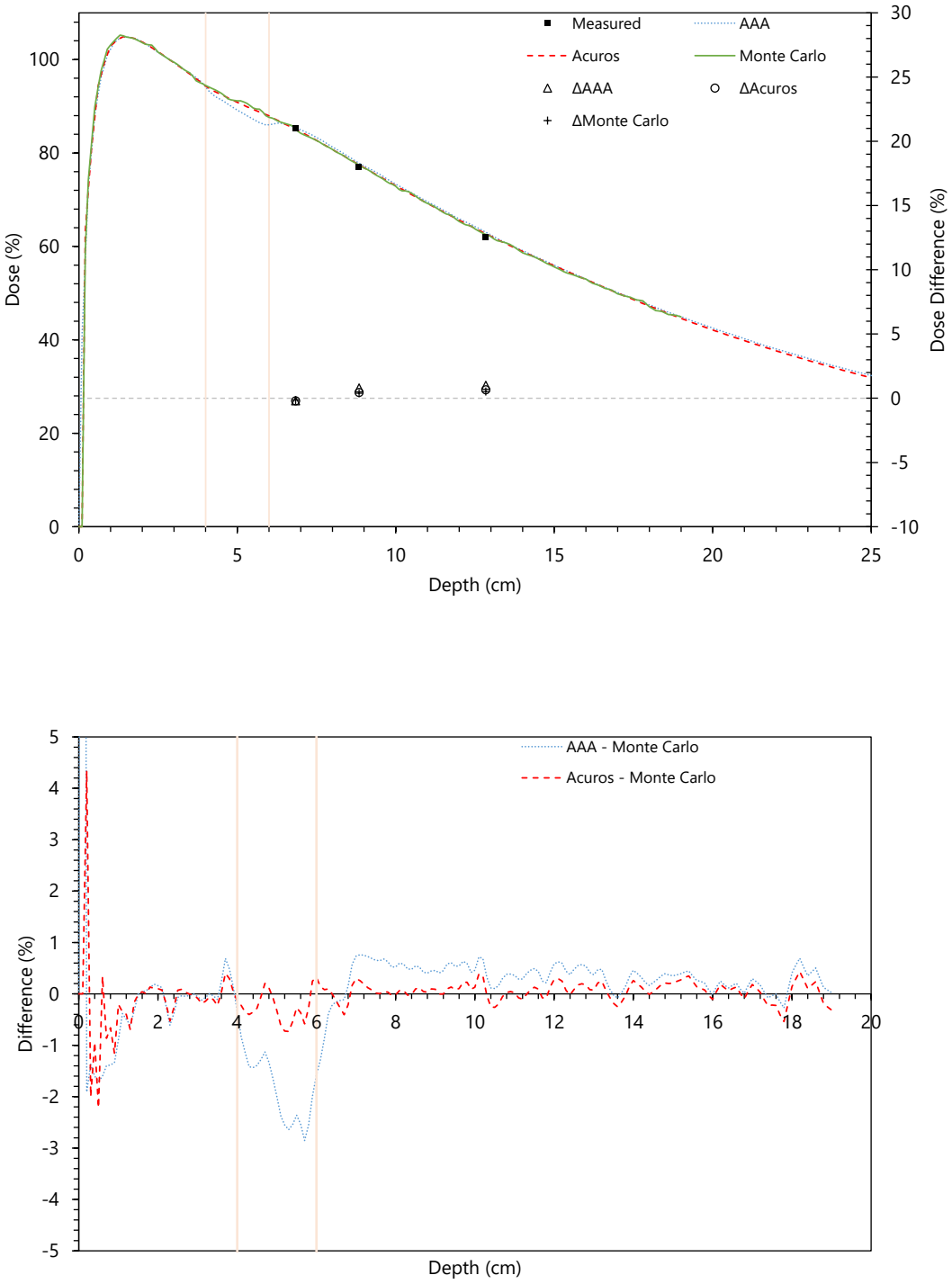

Fig. A.1: Slab geometry tests with a 10 x 10 cm field involving a 2 cm slab of lung.

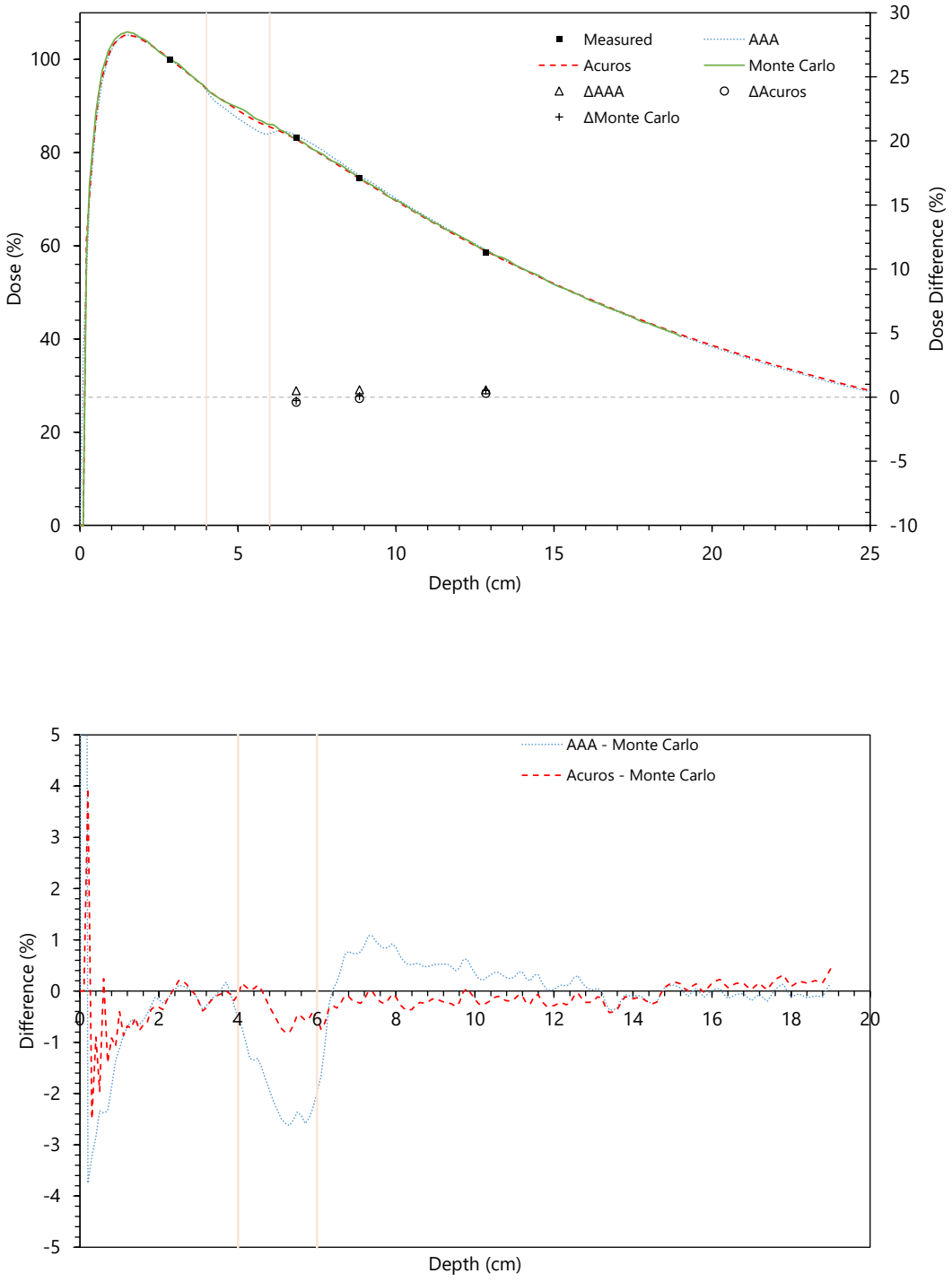

Fig. A.2: Slab geometry tests with a 5 x 5 cm field involving a 2 cm slab of lung.

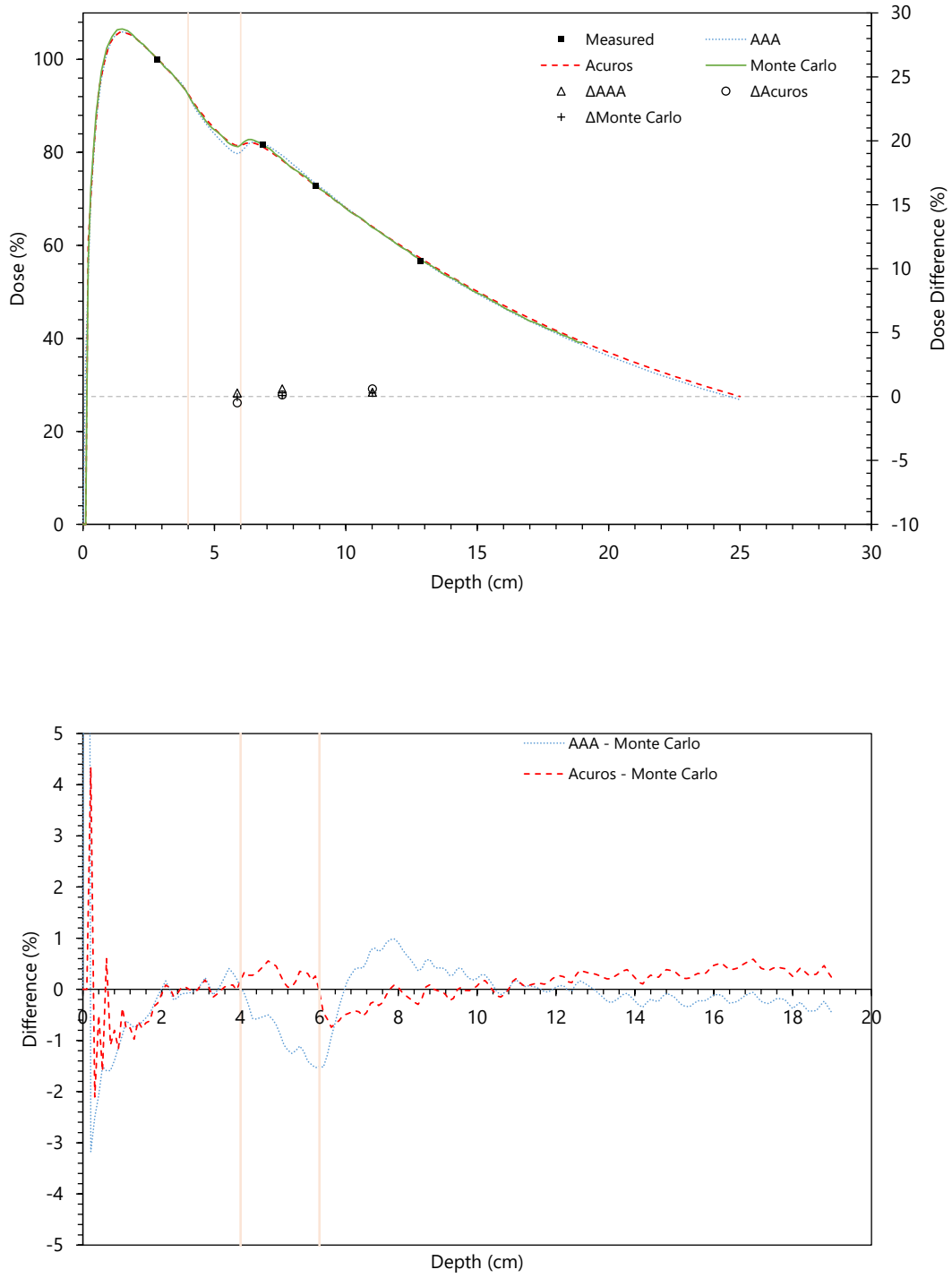

Fig. A.3: Slab geometry tests with a 3 x 3 cm field involving a 2 cm slab of lung.

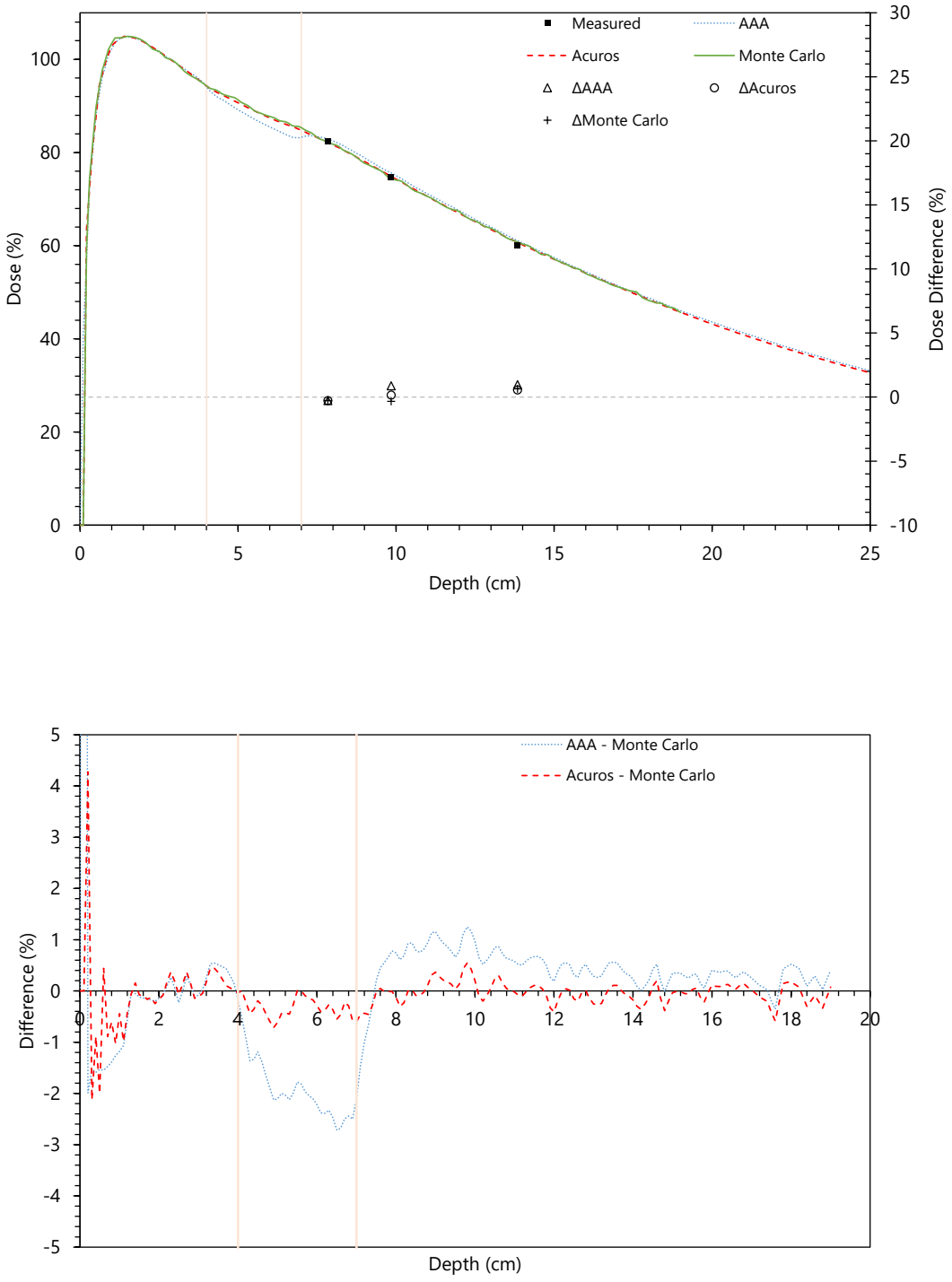

Fig. A.4: Slab geometry tests with a 10 x 10 cm field involving a 3 cm slab of lung.

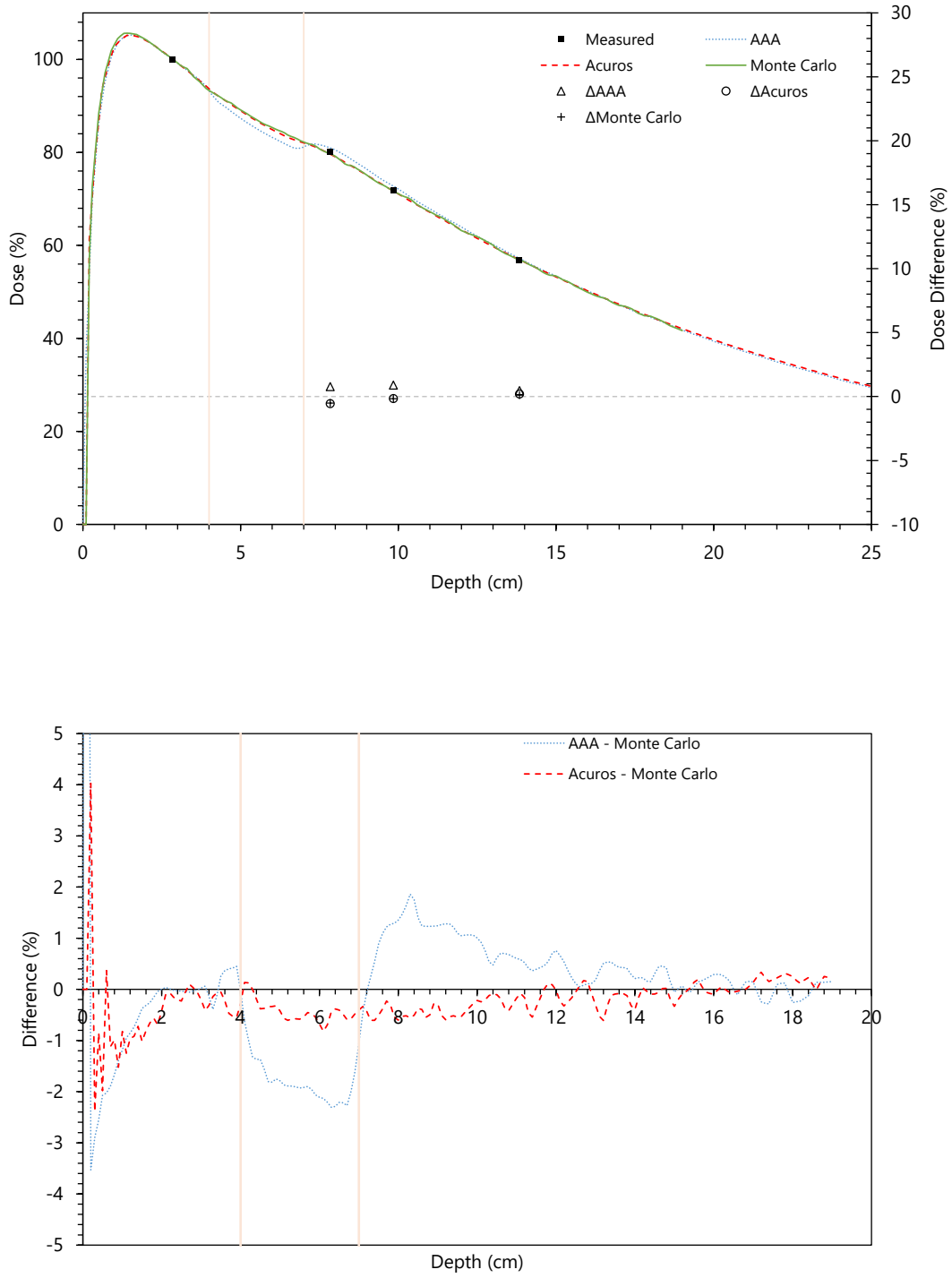

Fig. A.5: Slab geometry tests with a 5 x 5 cm field involving a 3 cm slab of lung.

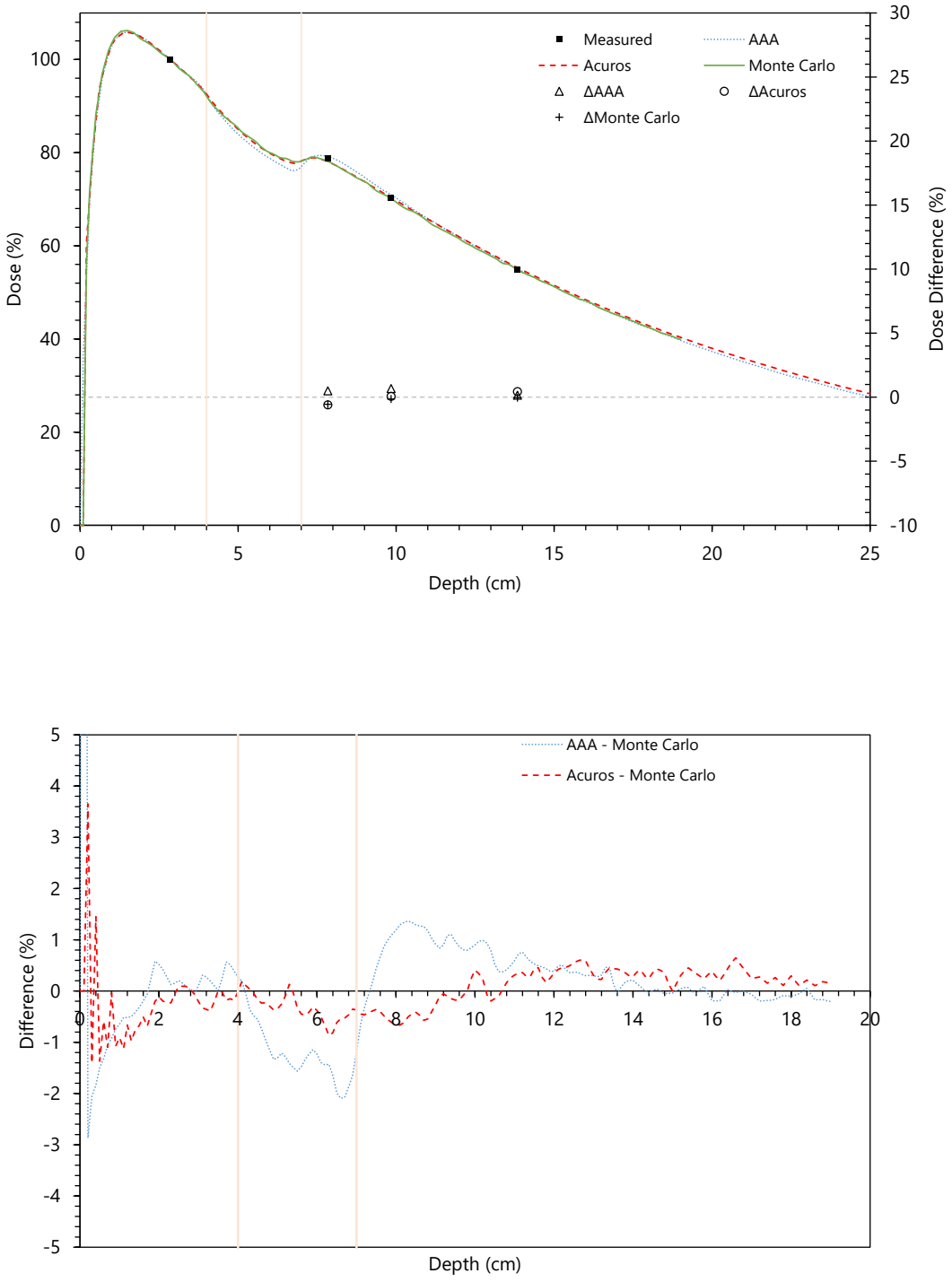

Fig. A.6: Slab geometry tests with a 3 x 3 cm field involving a 3 cm slab of lung.

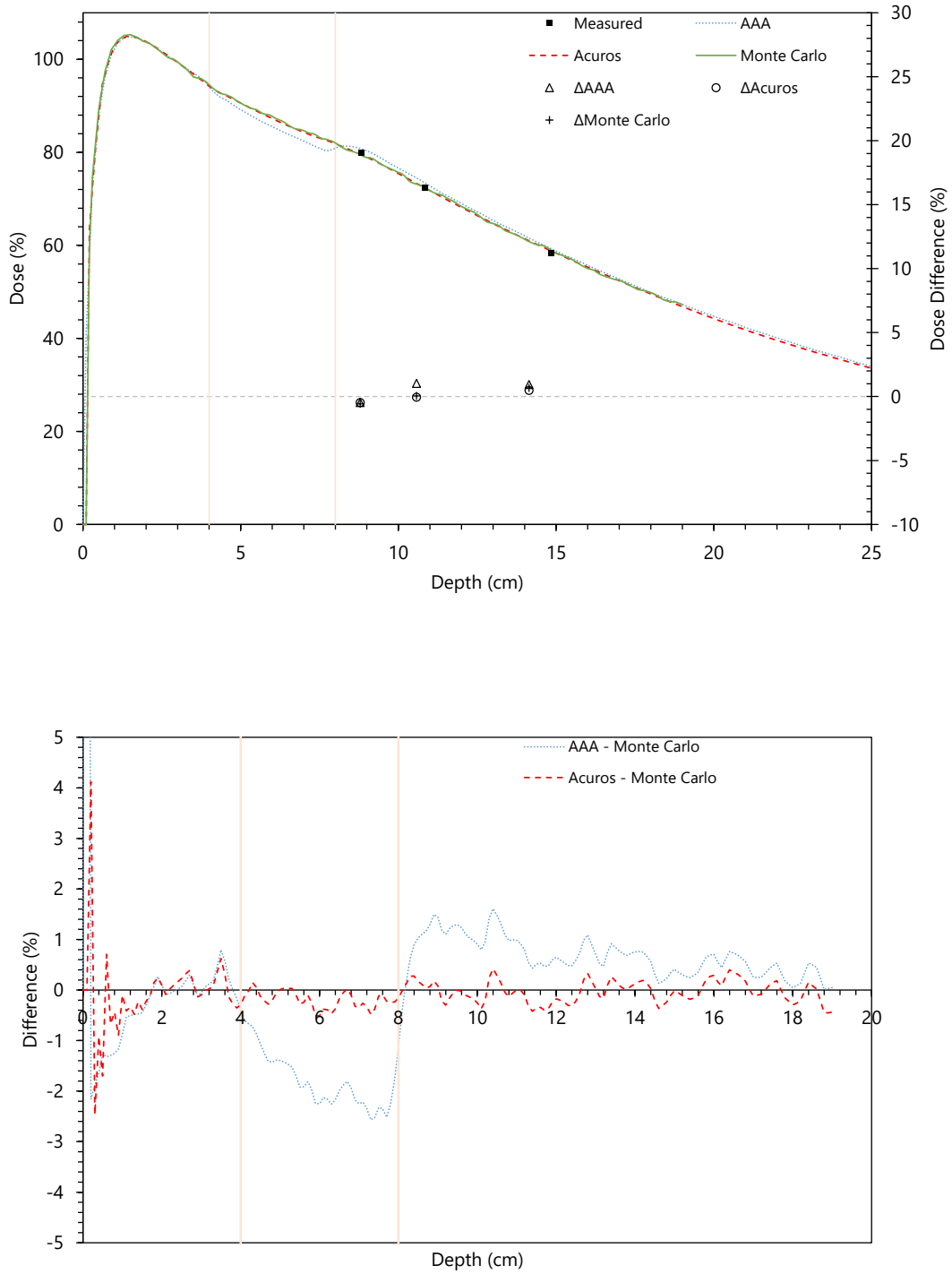

Fig. A.7: Slab geometry tests with a 10 x 10 cm field involving a 4 cm slab of lung.

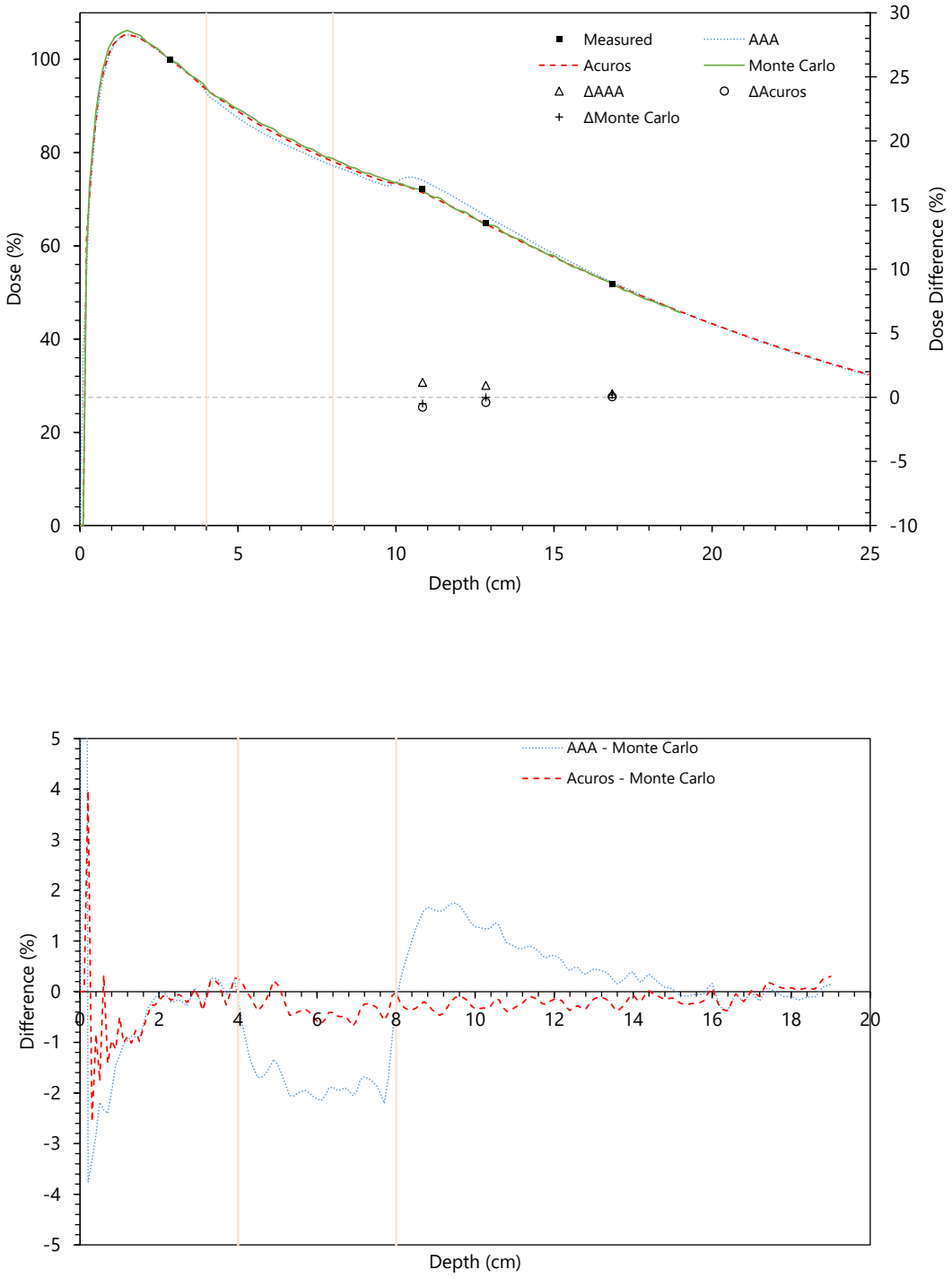

Fig. A.8: Slab geometry tests with a 5 x 5 cm field involving a 4 cm slab of lung.

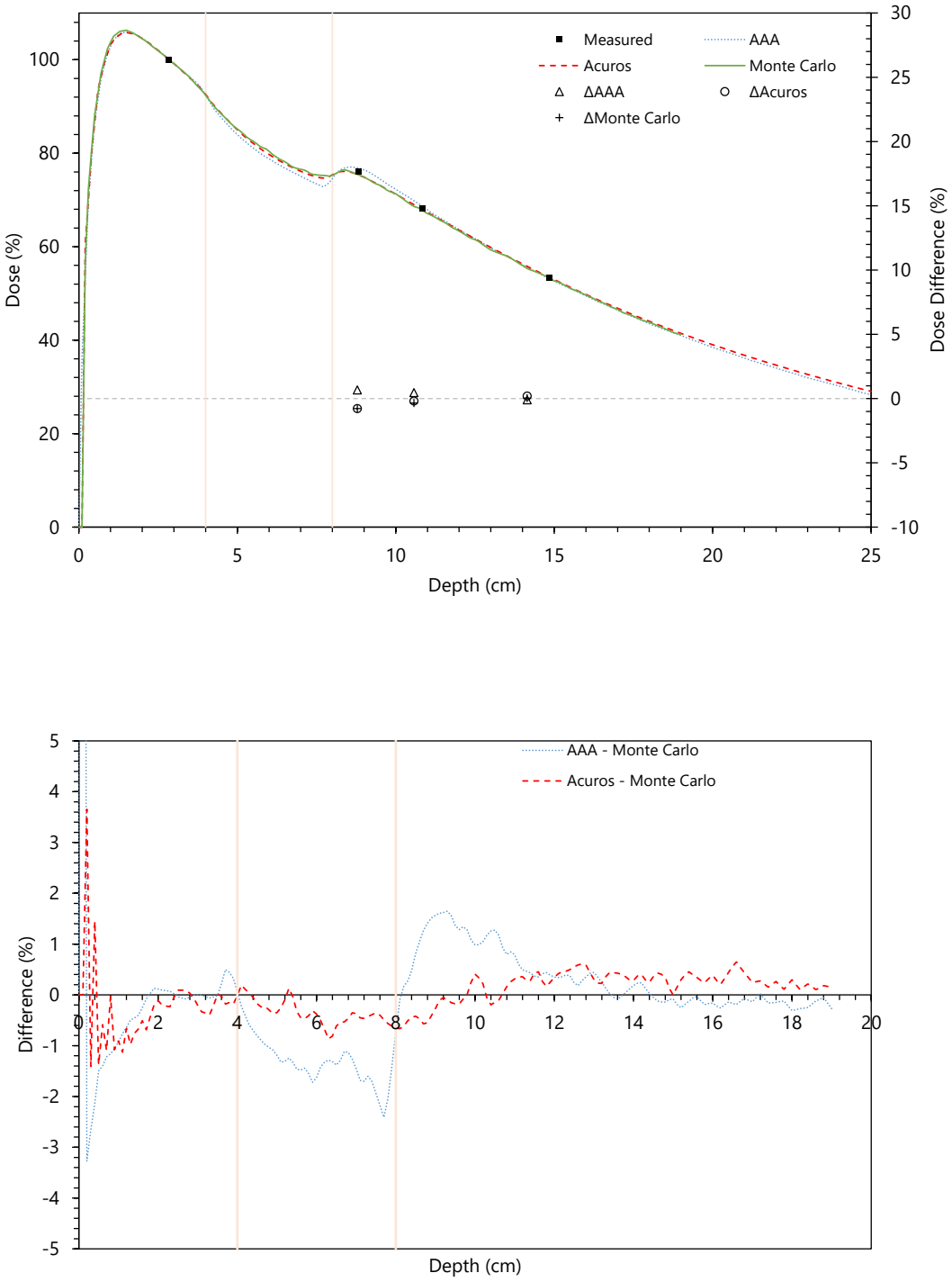

Fig. A.9: Slab geometry tests with a 3 x 3 cm field involving a 4 cm slab of lung.

Appendix B

TABLES FROM TECDOC 1583 TESTS

Below are the results from the verification tests based on TecDoc 1583. Note that, as per TecDoc 1583, the difference presented for each measurement point is normalised to the reference point in the plan.

B.1 AAA

Point	Expected (cGy)	Reading (nC)	Measured (cGy)	Difference (%)	Criteria(%)
1	241.2	7.802	242.26	-0.53	2
3	199	6.438	199.91	-0.46	2
5	169.7	5.501	170.82	-0.56	2
9	17.7	0.475	14.75	1.48	4
10	123.1	3.965	123.12	-0.01	3

Tab. B.1: AAA calculations vs point dose measurements in TecDoc 1583 Case 1.

Point	Expected (cGy)	Reading (nC)	Measured (cGy)	Difference (%)	Criteria(%)
1	169.3	5.232	162.47	4.21	2

Tab. B.2: AAA calculations vs point dose measurements in TecDoc 1583 Case 2.

Point	Expected (cGy)	Reading (nC)	Measured (cGy)	Difference (%)	Criteria
3	198.9	6.442	200.04	-0.57	2

Tab. B.3: AAA calculations vs point dose measurements in TecDoc 1583 Case 3.

Point	Expected (cGy)	Reading (nC)	Measured (cGy)	Difference (%)	Criteria(%)
5 F1	50.2	1.609	49.96	0.12	2
5 F2	49.7	1.617	50.21	-0.26	3
5 F3	50	1.557	48.35	0.84	3
5 F4	50	1.552	48.19	0.92	3
5 Sum	199.5	6.335	196.71	1.42	
6 F1	4.1	0.102	3.17	0.47	4
6 F2	5.6	0.1295	4.02	0.80	3
6 F3	30.2	1.027	31.89	-0.86	3
6 F4	64.8	2.117	65.74	-0.48	4
6 Sum	104.3	3.3755	104.82	-0.26	
10 F1	36.1	1.157	35.93	0.09	3
10 F2	70.6	2.325	72.20	-0.81	4
10 F3	3.6	0.114	3.54	0.03	4
10 F4	3.6	0.1125	3.49	0.05	3
10 Sum	113.9	3.7085	115.16	-0.64	

Tab. B.4: AAA calculations vs point dose measurements in TecDoc 1583 Case 4.

Point	Expected (cGy)	Reading (nC)	Measured (cGy)	Difference (%)	Criteria (%)
2	198.7	6.393	198.52	0.09	2
7	165	5.457	169.45	-2.24	4

Tab. B.5: AAA calculations vs point dose measurements in TecDoc 1583 Case 5.

Point	Expected (cGy)	Reading (nC)	Measured (cGy)	Difference (%)	Criteria (%)
3	199.3	6.331	196.59	1.38	3
7	101.7	3.464	107.56	-2.98	4
10	11.3	0.382	11.86	-0.29	5

Tab. B.6: AAA calculations vs point dose measurements in TecDoc 1583 Case 6.

Point	Expected (cGy)	Reading (nC)	Measured (cGy)	Difference (%)	Criteria (%)
5 (0)	66	2.105	65.36	0.34	2
5 (90)	61.7	1.956	60.74	0.51	4
5 (270)	61.5	1.959	60.83	0.36	4
5 (Sum)	189.2	6.02	186.93	1.21	

Tab. B.7: AAA calculations vs point dose measurements in TecDoc 1583 Case 7.

Point	Expected (cGy)	Reading (nC)	Measured (cGy)	Difference (%)	Criteria (%)
5 (90)	65.4	2.047	63.56	0.95	3
5 (270)	65.3	2.052	63.72	0.82	3
5 (30)	66	2.131	66.17	-0.09	3
5 (Sum)	196.7	6.23	193.45	1.68	

Tab. B.8: AAA calculations vs point dose measurements in TecDoc 1583 Case 8.

B.2 Acuros

Point	Expected (cGy)	Reading (nC)	Measured (cGy)	Difference (%)	Criteria (%)
1	240.5	7.802	242.27	-0.88	2
3	198.3	6.438	199.91	-0.81	2
5	168.6	5.501	170.82	-1.11	2
9	16	0.475	14.75	0.63	4
10	131.8	3.965	123.12	4.34	3

Tab. B.9: Acuros calculations vs point dose measurements in TecDoc 1583 Case 1.

Point	Expected (cGy)	Reading (nC)	Measured (cGy)	Difference (%)	Criteria (%)
1	162.40	5.23	162.46	-0.04	2

Tab. B.10: Acuros calculations vs point dose measurements in TecDoc 1583 Case 2.

Point	Expected (cGy)	Reading (nC)	Measured (cGy)	Difference (%)	Criteria (%)
3	198.2	6.442	200.04	-0.92	2

Tab. B.11: Acuros calculations vs point dose measurements in TecDoc 1583 Case 3.

Point	Expected (cGy)	Reading (nC)	Measured (cGy)	Difference (%)	Criteria (%)
5 F1	49.6	1.609	49.96	-0.18	2
5 F2	49.7	1.617	50.21	-0.26	3
5 F3	47.9	1.557	48.35	-0.23	3
5 F4	47.8	1.552	48.19	-0.20	3
5 Sum	195	6.335	196.71	-0.87	
6 F1	3.3	0.102	3.17	0.07	4
6 F2	4.2	0.1295	4.02	0.09	3
6 F3	32	1.027	31.89	0.06	3
6 F4	65.9	2.117	65.74	0.08	4
6 Sum	105.4	3.3755	104.82	0.30	
10 F1	38.6	1.157	35.93	1.36	3
10 F2	76.3	2.325	72.20	2.09	4
10 F3	3.7	0.114	3.54	0.08	4
10 F4	3.7	0.1125	3.49	0.11	3
10 Sum	122.3	3.7085	115.16	3.63	

Tab. B.12: Acuros calculations vs point dose measurements in TecDoc 1583 Case 4.

Point	Expected (cGy)	Reading (nC)	Measured (cGy)	Difference (%)	Criteria (%)
2	198.3	6.393	198.52	-0.11	2
7	166.6	5.457	169.45	-1.44	4

Tab. B.13: Acuros calculations vs point dose measurements in TecDoc 1583 Case 5.

Point	Expected (cGy)	Reading (nC)	Measured (cGy)	Difference (%)	Criteria (%)
3	198.9	6.331	196.59	1.17	3
7	106.7	3.464	107.56	-0.44	4
10	13.1	0.382	11.86	0.63	5

Tab. B.14: Acuros calculations vs point dose measurements in TecDoc 1583 Case 6.

Point	Expected (cGy)	Reading (nC)	Measured (cGy)	Difference (%)	Criteria (%)
5 (0)	65.6	2.105	65.36	0.13	2
5 (90)	59.5	1.956	60.74	-0.66	4
5 (270)	59.3	1.959	60.83	-0.82	4
5 (Sum)	184.4	6.02	186.93	-1.36	

Tab. B.15: Acuros calculations vs point dose measurements in TecDoc 1583 Case 7.

Point	Expected (cGy)	Reading (nC)	Measured (cGy)	Difference (%)	Criteria (%)
5 (90)	63.4	2.047	63.56	-0.08	3
5 (270)	63.3	2.052	63.72	-0.22	3
5 (30)	66	2.131	66.17	-0.09	3
5 (Sum)	192.2	6.23	193.45	-0.65	

Tab. B.16: Acuros calculations vs point dose measurements in TecDoc 1583 Case 8.

Appendix C

TOOLS FOR DOSE DISTRIBUTION COMPARISONS

C.1 Gamma

Low *et al.* [1998] introduced the γ value in 1998, and it is now a commonly used parameter for the comparison of two dose distributions. The γ value (gamma) incorporates both dose and spatial difference information into one calculation, Hence γ is useful in both high and low dose-gradient regions.

If $\vec{r_m}$ is a point in the measured dose distribution and $\vec{r_c}$ is a point in the calculated dose distribution, then a value of γ is obtained for each point $\vec{r_m}$ in the measured dose distribution.

For each $\vec{r_m}$, γ is defined as

$$\gamma(\vec{r_m}) = \min_{\vec{r_c}} \Gamma(\vec{r_m}, \vec{r_c}), \tag{C.1}$$

with

$$\Gamma(\vec{r_m}, \vec{r_c}) = \sqrt{\frac{|\vec{r_m} - \vec{r_c}|^2}{\Delta d_M^2} + \frac{\delta^2(\vec{r_m}, \vec{r_c})}{\Delta D_M^2}} \tag{C.2}$$

and

$$\delta(\vec{r_m}, \vec{r_c}) = \frac{D_m(\vec{r_m}) - D_c(\vec{r_c})}{D_m(\vec{r_{norm}})} \tag{C.3}$$

,

where Δd_M^2 and ΔD_M^2 are spatial and dose difference tolerances.

For comparing measured profiles and PDDs with those calculated by DOSXYZnrc, a program was written which performs a one dimensional gamma analysis on the two curves. The dose difference and distance tolerances used were 1% and 1 mm respectively.

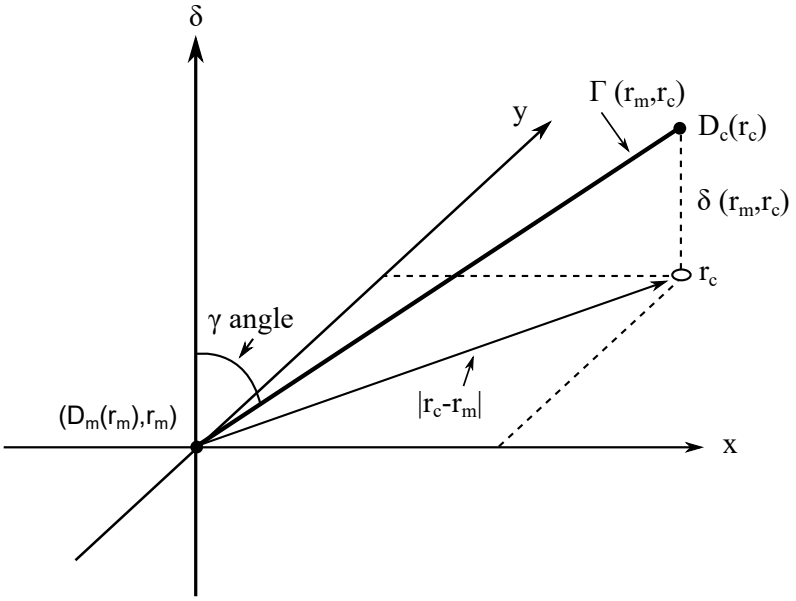

Fig. C.1: Geometric representation of the γ value $\gamma(\vec{r_c}, \vec{r_m})$ for $\vec{r_m}$ in the measured distribution and one point in the calculated distribution $\vec{r_c}$.

C.2 DicomViewer

For dose comparisons, it is useful to assess differences by looking at isodose lines drawn on a CT dataset or by looking at the difference in the calculation's Dose Volume Histograms (DVH). Most modern TPS have the ability to draw isodose lines and calculate DVH from a treatment plan. Comparing DOSXYZnrc calculated doses to doses calculated in TPS is difficult as the output of DOSXYZnrc calculations are in the .3ddose format. The format is described by [Walters *et al.*, 2005] and essentially lists the x, y and z voxel locations and the relative dose in each voxel. Non-commercial tools available for reading and writing .3ddose files are limited and so a program (called DicomViewer) was written for this study in order to properly compare EGSnrc doses to those from the TPS.

C.2.1 DICOM RT

The DICOM standard enables a standardised method of communicating diagnostic and therapeutic images and information. In radiation therapy, for example, the DICOM standard provides a way to transfer CT images, treatment plans, ROI contours and dose information from one software system to another. In DicomViewer, dose distribution, CT images and regions of interests are read from DICOM files.

The free and open source Fellow Oak DICOM library is used to read data from DICOM files.

Isodose lines

Isodose lines were drawn onto CT images through the Marching Squares algorithm Lorensen and Cline [1987]. The dose grid is sampled at a customisable grid spacing and given to the marching squares algorithm for dose drawing.

Dose volume histograms

A DVH is a convenient way to represent dose distribution through a region of interest. A differential DVH shows, for many dose intervals, the volume of a region of interest that has a dose in that interval. A cumulative DVH displays the volume of the region of interest that has a dose greater than or equal to a certain dose. DicomViewer calculates differential DVH via the following algorithm:

1. Find the dimensions of the cube surrounding the entire volume of the region of interest
2. Divide the cube into voxels of dimensions smaller than the size of the dose grid
3. For each voxel, determine whether the centre of the voxel is inside the region of interest. This is determined by first converting the slice on each polygon into a binary mask. If the centre of the voxel is not on the same slice as a polygon then a polygon is created from the interpolation of the surrounding slices, as described by Schenk *et al.* [2000]
4. If the centre of the voxel is inside the region of interest, interpolate the dose at the centre of the voxel and add the voxel volume to the relevant dose bin (Figure C.2).

Comparisons to Eclipse DVH calculation Multiple cumulative DVH curves calculated in Eclipse were compared to those calculated in DicomViewer. Complete agreement is not expected due to the difference in algorithm implementation, however good agreement was found for the calculations performed (Figure C.3).

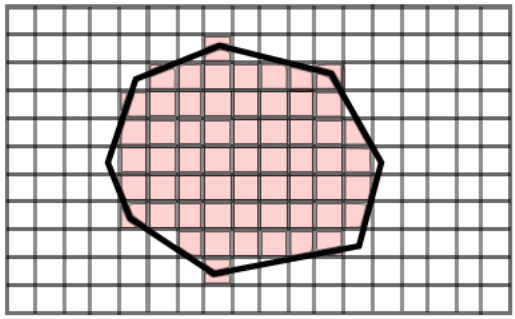

Fig. C.2: Sampling a polygon for the computation of the DVH. If the centre of the voxel is inside the region of interest, then the voxel volume is added to the relevant dose bin.

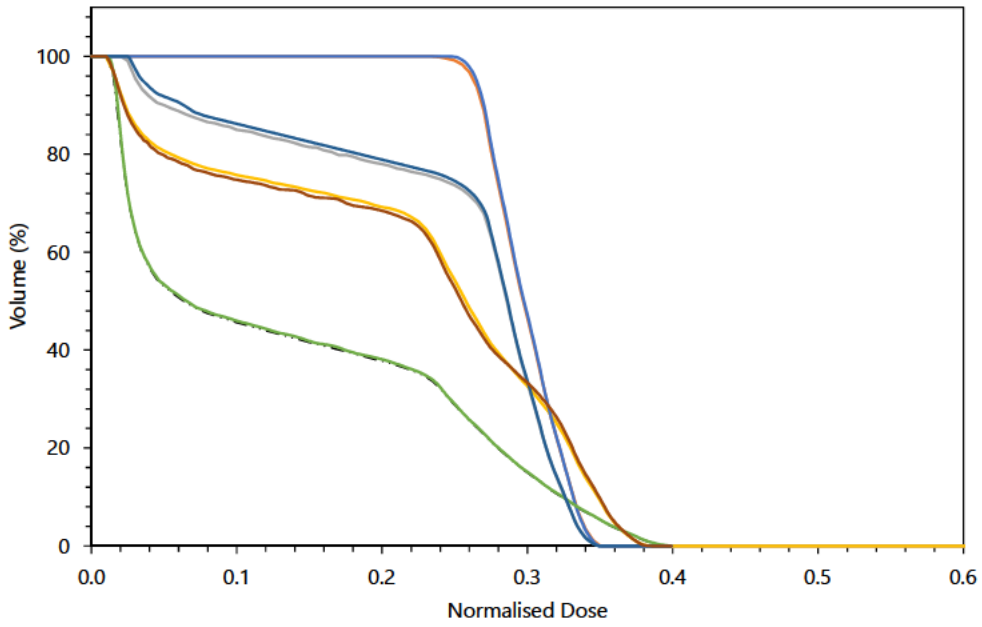

Fig. C.3: Comparisons between DVHs calculated with Eclipse and DicomViewer for multiple regions of interests.

C.3 DICOM to DOSXYZnrc geometry coordinate transformation verification

Calculations with different beam parameters were made with Eclipse and DOSXYZnrc to verify the transformations from DICOM coordinates to DOSXYZnrc discussed in Section 5.4. The results are presented below.

C.3.1 Geometry verification test 1

X1 (cm)	X2 (cm)	Y1 (cm)	Y2 (cm)	iso (cm)	θ_G	θ_T	θ_C	θ	ϕ	ϕ_coll
5	-2	8	0	(0, 0, 0)	0	0	0	90	270	270

Tab. C.1: Eclipse beam parameters and DOSXYZnrc cylindrical coordinates for verification test 1.

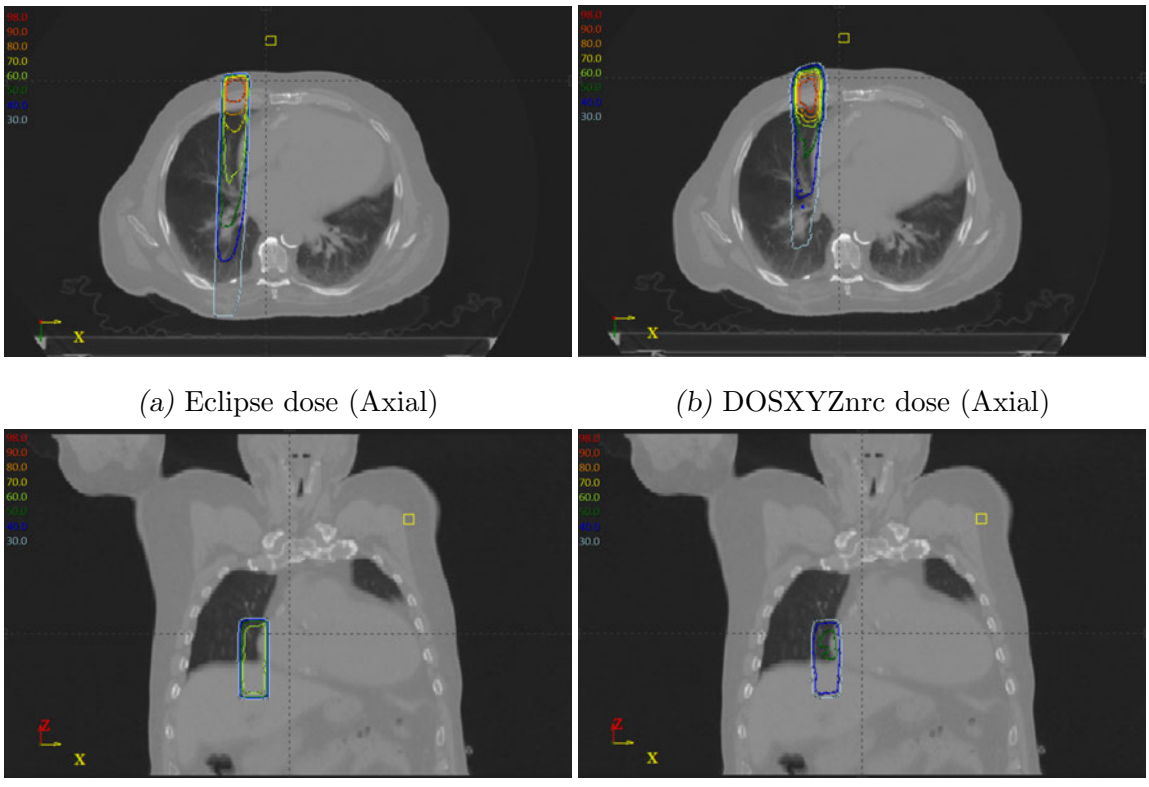

(a) Eclipse dose (Axial) *(b)* DOSXYZnrc dose (Axial)

(c) Eclipse dose (Coronal) *(d)* DOSXYZnrc dose (Coronal)

Fig. C.4: Dose distributions from geometry verification test 1.

C.3.2 Geometry verification test 2

X1 (cm)	X2 (cm)	Y1 (cm)	Y2 (cm)	iso (cm)	θ_G	θ_T	θ_C	θ	ϕ	ϕ_coll
5	-2	8	0	(0, 0, 0)	0	60	0	90	270	210

Tab. C.2: Eclipse beam parameters and DOSXYZnrc cylindrical coordinates for verification test 2.

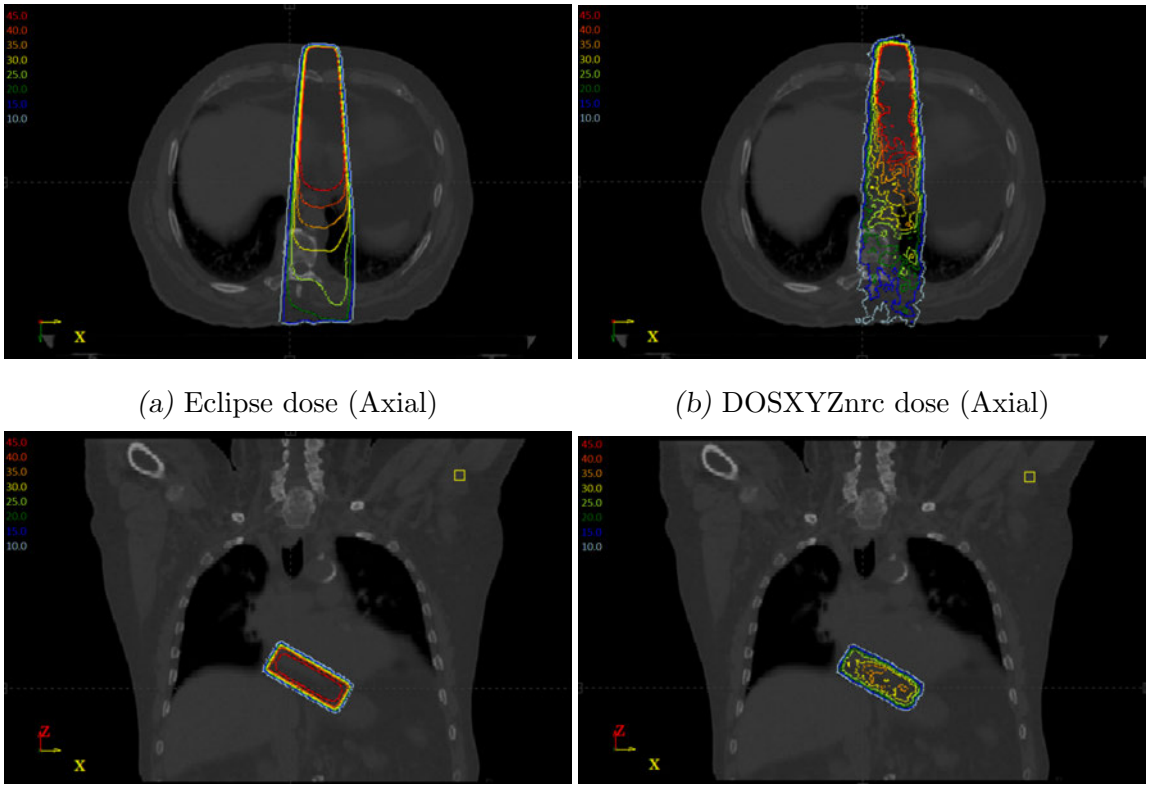

(a) Eclipse dose (Axial) *(b)* DOSXYZnrc dose (Axial)

(c) Eclipse dose (Coronal) *(d)* DOSXYZnrc dose (Coronal)

Fig. C.5: Dose distributions from geometry verification test 2.

C.3.3 Geometry verification test 3

X1 (cm)	X2 (cm)	Y1 (cm)	Y2 (cm)	iso (cm)	θ_G	θ_T	θ_C	θ	ϕ	ϕ_coll
5	-2	8	0	(0, 0, 0)	320	60	0	247.24	217	100

Tab. C.3: Eclipse beam parameters and DOSXYZnrc cylindrical coordinates for verification test 3.

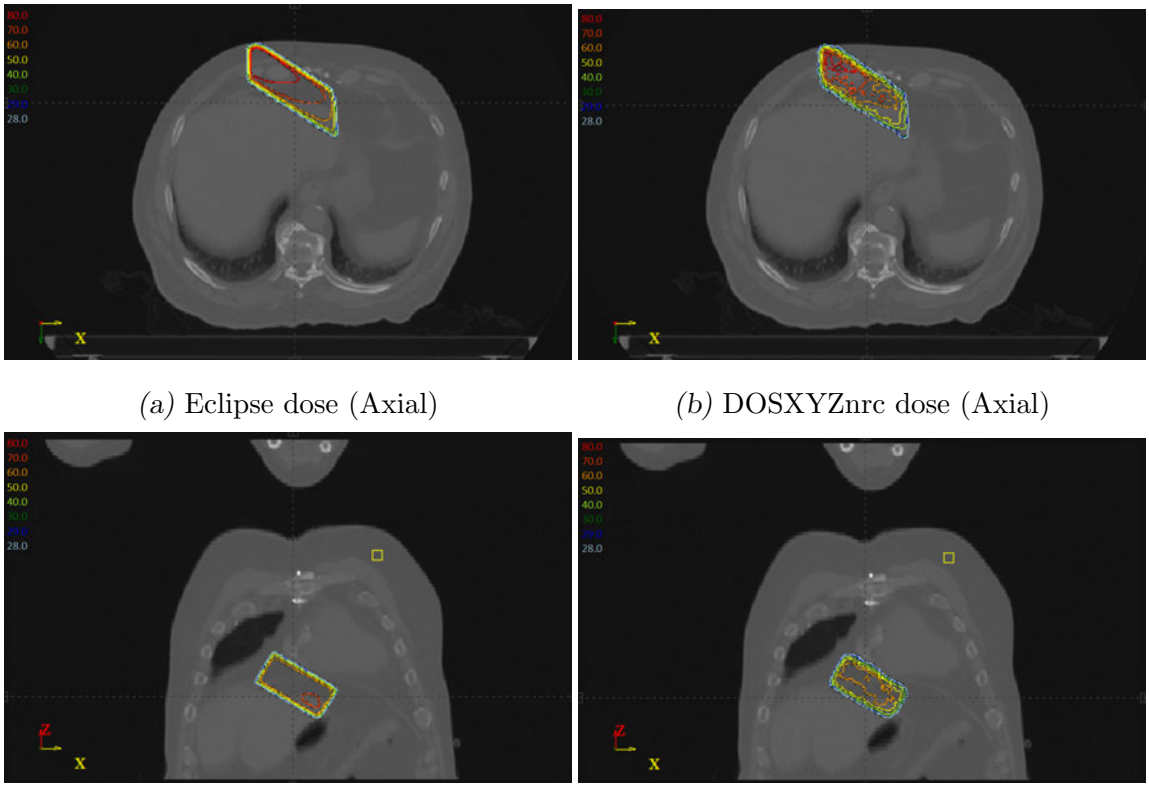

(a) Eclipse dose (Axial) *(b)* DOSXYZnrc dose (Axial)

(c) Eclipse dose (Coronal) *(d)* DOSXYZnrc dose (Coronal)

Fig. C.6: Dose distributions from geometry verification test 3.

C.3.4 Geometry verification test 4

X1 (cm)	X2 (cm)	Y1 (cm)	Y2 (cm)	iso (cm)	θ_G	θ_T	θ_C	θ	ϕ	ϕ_coll
-2	-5	-2	8	(0, 0, 0)	15	270	45	105	270	315

Tab. C.4: Eclipse beam parameters and DOSXYZnrc cylindrical coordinates for verification test 4.

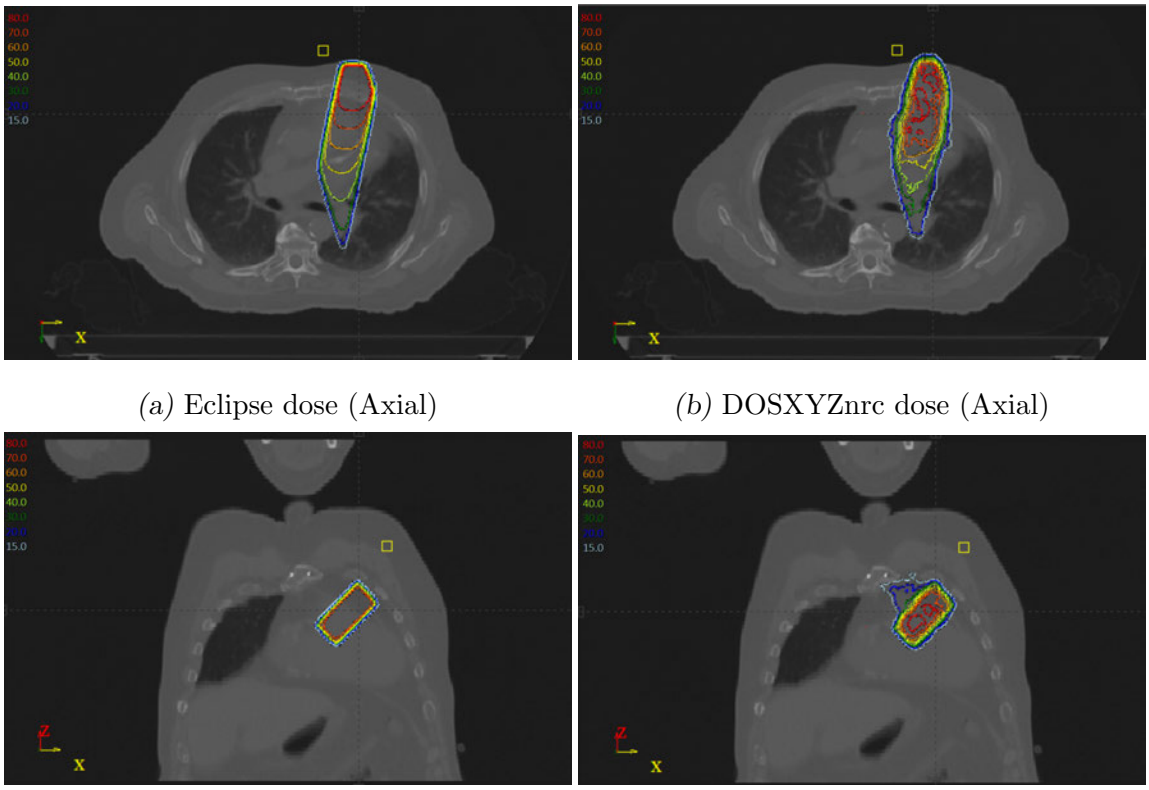

(a) Eclipse dose (Axial) *(b)* DOSXYZnrc dose (Axial)

(c) Eclipse dose (Coronal) *(d)* DOSXYZnrc dose (Coronal)

Fig. C.7: Dose distributions from geometry verification test 4.

C.3.5 Geometry verification test 5

X1 (cm)	X2 (cm)	Y1 (cm)	Y2 (cm)	iso (cm)	θ_G	θ_T	θ_C	θ	ϕ	ϕ_coll
-2	-5	-2	8	(-5,5,-3)	15	270	45	105	270	315

Tab. C.5: Eclipse beam parameters and DOSXYZnrc cylindrical coordinates for verification test 5.

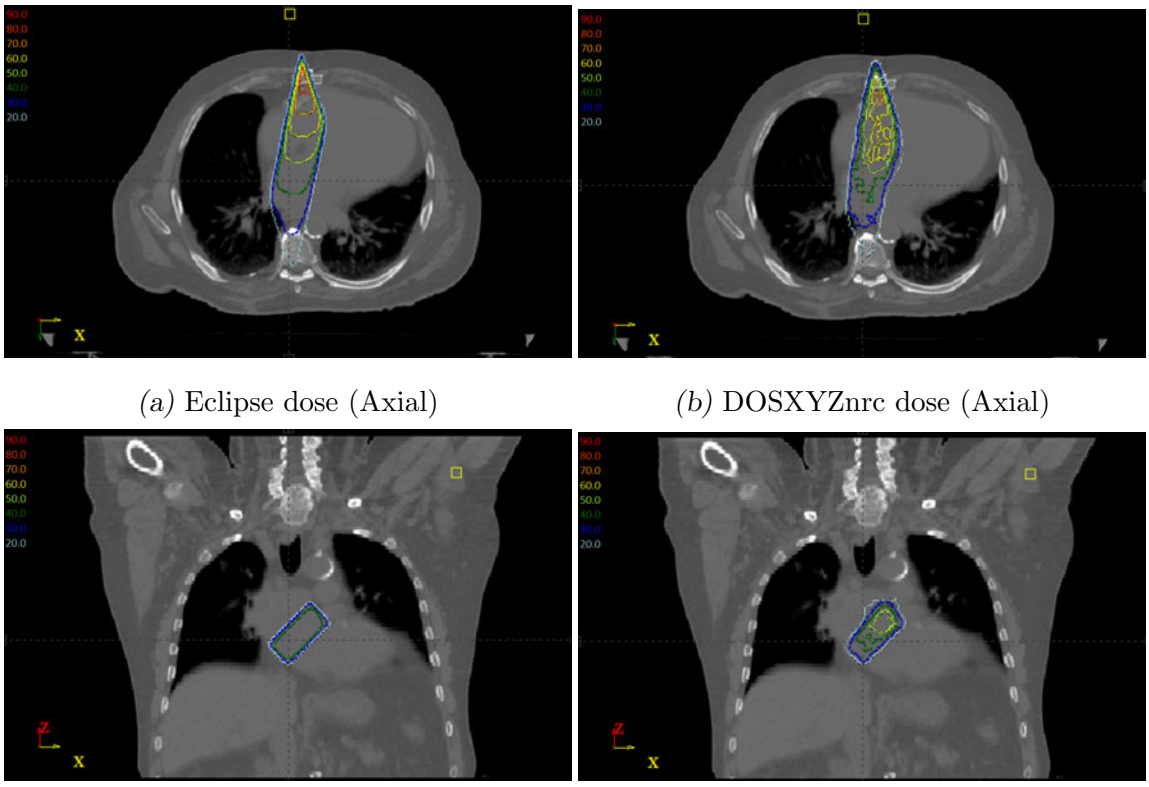

(a) Eclipse dose (Axial) *(b)* DOSXYZnrc dose (Axial)

(c) Eclipse dose (Coronal) *(d)* DOSXYZnrc dose (Coronal)

Fig. C.8: Dose distributions from geometry verification test 5.

C.4 Uncertainties

In this study, when a result has been presented as $a \pm b$, b represents $1.96 \times \sigma_{\bar{x}}$, where $\sigma_{\bar{x}}$ is the standard error of the mean $\bar{x}$ and is equal to $\sigma/\sqrt{(}n)$, where σ is the standard deviation of the set of results and n is the number of samples.

BIBLIOGRAPHY

Aarup, L. R., Nahum, A. E., Zacharatou, C., Juhler-Nøttrup, T., Knöös, T., Nyström, H., Specht, L., Wieslander, E. and Korreman, S. S. [2009], 'The effect of different lung densities on the accuracy of various radiotherapy dose calculation methods: Implications for tumour coverage', *Radiotherapy and Oncology* **91**(3), 405–414.

Andreo, P., Burns, D., Hohlfeld, K., Huq, M., Kanai, T., Laitano, F., Smyth, V. and Vynckier, S. [2001], 'TRS-398: Absorbed Dose Determination in External Beam Radiotherapy: An International Code of Practice for Dosimetry based on Standards of Absorbed Dose to Water', *International Atomic Energy Agency* **420**.

Baskar, R., Lee, K. A., Yeo, R. and Yeoh, K.-W. [2012], 'Cancer and radiation therapy: current advances and future directions', *International journal of medical sciences* **9**(3), 193.

Batho, H. F. [1964], 'LUNG CORRECTIONS IN COBALT 60 BEAM THERAPY', *Journal of the Canadian Association of Radiologists* **15**, 79–83.

Berger, M. J. [1963], 'Monte carlo calculation of the penetration and diffusion of fast charged particles', *Methods in Computational Physics* **1**, 135–215.

Berger, M. J. and Seltzer, S. M. [1982], *Stopping Powers and Ranges of Electrons and Positrons (2nd Ed.)*, National Bureau of Standards (USA).

Boyer, A. L. and Schultheiss, T. [1988], 'Effects of dosimetric and clinical uncertainty on complication-free local tumor control', *Radiotherapy and Oncology* **11**(1), 65–71.

Bragg, C. M. and Conway, J. [2006], 'Dosimetric verification of the anisotropic analytical algorithm for radiotherapy treatment planning', *Radiotherapy and Oncology* **81**(3), 315–323.

Bush, K., Gagne, I. M., Zavgorodni, S., Ansbacher, W. and Beckham, W. [2011], 'Dosimetric validation of Acuros® XB with Monte Carlo methods for photon dose calculations', *Medical Physics* **38**(4), 2208.

Dunn, L., Lehmann, J., Lye, J., Kenny, J., Kron, T., Alves, A., Cole, A., Zifodya, J. and Williams, I. [2015], 'National dosimetric audit network finds discrepancies in AAA lung inhomogeneity corrections', *Physica Medica* **31**(5), 435–441.

Failla, G. A., Wareing, T., Archambault, Y. and Thompson, S. [2010], 'Acuros XB advanced dose calculation for the Eclipse treatment planning system', *Palo Alto, CA: Varian Medical Systems* .

Fogliata, A., Nicolini, G., Clivio, A., Vanetti, E. and Cozzi, L. [2011*a*], 'Dosimetric evaluation of Acuros XB Advanced Dose Calculation algorithm in heterogeneous media', *Radiation Oncology* **6**(1), 1.

Fogliata, A., Nicolini, G., Clivio, A., Vanetti, E. and Cozzi, L. [2011*b*], 'On the dosimetric impact of inhomogeneity management in the Acuros XB algorithm for breast treatment', *Radiation Oncology* **6**(1), 1.

Fogliata, A., Nicolini, G., Clivio, A., Vanetti, E., Mancosu, P. and Cozzi, L. [2011], 'Dosimetric validation of the Acuros XB Advanced Dose Calculation algorithm: fundamental characterization in water', *Physics in Medicine and Biology* **56**(9), 2885–2886.

Fragoso, M., Kawrakow, I., Faddegon, B. A., Solberg, T. D. and Chetty, I. J. [2009], 'Fast, accurate photon beam accelerator modeling using BEAMnrc: A systematic investigation of efficiency enhancing methods and cross-section data', *Medical Physics* **36**(12), 5451.

Gibbons, J. P., Antolak, J. A., Followill, D. S., Huq, M. S., Klein, E. E., Lam, K. L., Palta, J. R., Roback, D. M., Reid, M. and Khan, F. M. [2014], 'Monitor unit calculations for external photon and electron beams: Report of the AAPM Therapy Physics Committee Task Group No. 71', *Medical physics* **41**(3).

Han, T., Followill, D., Mikell, J., Repchak, R., Molineu, A., Howell, R., Salehpour, M. and Mourtada, F. [2013], 'Dosimetric impact of Acuros XB deterministic ra-

diation transport algorithm for heterogeneous dose calculation in lung cancer', *Medical Physics* **40**(5), 051710.

Han, T., Mikell, J. K., Salehpour, M. and Mourtada, F. [2011], 'Dosimetric comparison of Acuros XB deterministic radiation transport method with Monte Carlo and model-based convolution methods in heterogeneous media', *Medical Physics* **38**(5), 2651.

Han, T., Mourtada, F., Kisling, K., Mikell, J., Followill, D. and Howell, R. [2012], 'Experimental validation of deterministic Acuros XB algorithm for IMRT and VMAT dose calculations with the Radiological Physics Center's head and neck phantom', *Medical Physics* **39**(4), 2193.

Hasenbalg, F., Neuenschwander, H., Mini, R. and Born, E. J. [2007], 'Collapsed cone convolution and analytical anisotropic algorithm dose calculations compared to VMC++ Monte Carlo simulations in clinical cases', *Physics in Medicine and Biology* **52**(13), 3679–3691.

Hoffmann, L., Jørgensen, M.-B. K., Muren, L. P. and Petersen, J. B. B. [2012], 'Clinical validation of the Acuros XB photon dose calculation algorithm, a grid-based Boltzmann equation solver', *Acta Oncologica* **51**(3), 376–385.

Johns, H. and Cunningham, J. [1983], 'The physics of radiology 4th ed', *Thomas Springfield, Illinois* .

Kan, M. W. K., Leung, L. H. T. and Yu, P. K. N. [2012], 'Verification and dosimetric impact of Acuros XB algorithm on intensity modulated stereotactic radiotherapy for locally persistent nasopharyngeal carcinoma', *Medical Physics* **39**(8), 4705.

Kawrakow, I. and Rogers, D. W. O. [2000], 'The EGSnrc code system', *NRC Report PIRS-701, NRC, Ottawa* .

Kawrakow, I., Rogers, D. W. O. and Walters, B. R. B. [2004], 'Large efficiency improvements in BEAMnrc using directional bremsstrahlung splitting', *Medical Physics* **31**(10), 2883.

Kawrakow, I. and Walters, B. R. B. [2006], 'Efficient photon beam dose calculations using DOSXYZnrc with BEAMnrc', *Medical Physics* **33**(8), 3046.

Kim, J.-H., Hill, R. and Kuncic, Z. [2012], 'An evaluation of calculation parameters in the EGSnrc/BEAMnrc Monte Carlo codes and their effect on surface dose calculation', *Physics in Medicine and Biology* **57**(14), N267–N278.

Klein, E., Chin, L., Rice, R. and Mijnheer, B. [1993], 'The influence of air cavities on interface doses for photon beams', *International journal of radiation oncology, biology, physics* **27**(2), 419.

Kroon, P. S., Hol, S. and Essers, M. [2013], 'Dosimetric accuracy and clinical quality of Acuros XB and AAA dose calculation algorithm for stereotactic and conventional lung volumetric modulated arc therapy plans', *Radiation Oncology* **8**(1), 1.

Lag, R., Harkins, D., Krapcho, M., Mariotto, A., Miller, B., Feuer, E., Clegg, L., Eisner, M., Horner, M., Howlader, N. and others [1975], 'Seer cancer statistics review', *Bethesda, National Cancer Institute* pp. 1975–2003.

Liu, H.-W., Nugent, Z., Clayton, R., Dunscombe, P., Lau, H. and Khan, R. [2014], 'Clinical impact of using the deterministic patient dose calculation algorithm Acuros XB for lung stereotactic body radiation therapy', *Acta Oncologica* **53**(3), 324–329.

Lloyd, S. A. M. and Ansbacher, W. [2013], 'Evaluation of an analytic linear Boltzmann transport equation solver for high-density inhomogeneities', *Medical Physics* **40**(1), 011707.

Lorensen, W. E. and Cline, H. E. [1987], Marching cubes: A high resolution 3d surface construction algorithm, ACM Press, pp. 163–169.

Low, D. A., Harms, W. B., Mutic, S. and Purdy, J. A. [1998], 'A technique for the quantitative evaluation of dose distributions', *Medical Physics* **25**(5), 656.

Metcalfe, P., Kron, T., Hoban, P. and Metcalfe, P. [2007], *The physics of radiotherapy x-rays and electrons / by Peter Metcalfe, Tomas Kron, and Peter Hoban*, Medical Physics Pub, Madison, Wis.

Mißlbeck, M. and Kneschaurek, P. [2012], 'Comparison between Acuros XB and Brainlab Monte Carlo algorithms for photon dose calculation', *Strahlentherapie und Onkologie* **188**(7), 599–605.

Mohammed, M., Chakir, E., Boukhal, H., Saeed, M. and El Bardouni, T. [2016], 'Evaluation of variance reduction techniques in BEAMnrc Monte Carlo simulation to improve the computing efficiency', *Journal of Radiation Research and Applied Sciences* .

Ojala, J., Kapanen, M., Sipilä, P., Hyödynmaa, S. and Pitkänen, M. [2014], 'The accuracy of Acuros XB algorithm for radiation beams traversing a metallic hip implant—comparison with measurements and Monte Carlo calculations', *Journal of Applied Clinical Medical Physics* **15**(5).

Papanikolaou, N., Battista, J., Boyer, L., Kappas, C., Klein, E., Mackie, R., Sharpe, M. and Van Dyk, J. [2004], Tissue inhomogeneity corrections for megavoltage photon beams, Technical Report 85, AAPM Task Group 65.

Rana, S. and Rogers, K. [2013*a*], 'Dosimetric evaluation of Acuros XB dose calculation algorithm with measurements in predicting doses beyond different air gap thickness for smaller and larger field sizes', *Journal of Medical Physics* **38**(1), 9.

Rana, S. and Rogers, K. [2013*b*], 'Dosimetric evaluation of Acuros XB dose calculation algorithm with measurements in predicting doses beyond different air gap thickness for smaller and larger field sizes', *Journal of Medical Physics* **38**(1), 9.

Rana, S., Rogers, K., Lee, T., Reed, D. and Biggs, C. [2013*a*], 'Dosimetric impact of Acuros XB dose calculation algorithm in prostate cancer treatment using RapidArc', *Journal of Cancer Research and Therapeutics* **9**(3), 430.

Rana, S., Rogers, K., Lee, T., Reed, D. and Biggs, C. [2013*b*], 'Verification and Dosimetric Impact of Acuros XB Algorithm for Stereotactic Body Radiation Therapy (SBRT) and RapidArc Planning for Non-Small-Cell Lung Cancer (NSCLC) Patients', *International Journal of Medical Physics, Clinical Engineering and Radiation Oncology* **02**(01), 6–14.

Rogers, D. W. O., Walters, B., Kawrakow, I. and others [2009], 'BEAMnrc users manual', *NRC Report PIRS* **509**, 12.

Rong, Y., Mubata, C., Chisela, W., Jaradat, H., Tewatia, D. and Paliwal, B. [2006],

'SU-FF-T-448: Validation of a New Photon Dose Calculation Model—Analytical Anisotropic Algorithm', *Medical Physics* **33**(6), 2148.

Schenk, A., Prause, G. and Peitgen, H.-O. [2000], Efficient semiautomatic segmentation of 3d objects in medical images, *in* 'MICCAI', Vol. 1935, Springer, pp. 186–195.

Schmitz, R. M., Telfer, O., Townson, R. W. and Zavgorodni, S. [2014], 'Generalized coordinate transformations for Monte Carlo (DOSXYZnrc and VMC++) verifications of DICOM compatible radiotherapy treatment plans', *arXiv preprint arXiv:1406.0014* .

Sheikh-Bagheri, D. and Rogers, D. W. O. [2002], 'Sensitivity of megavoltage photon beam Monte Carlo simulations to electron beam and other parameters', *Medical Physics* **29**(3), 379.

Siebers, J. V., Keall, P. J., Nahum, A. E. and Mohan, R. [2000], 'Converting absorbed dose to medium to absorbed dose to water for Monte Carlo based photon beam dose calculations', *Physics in Medicine and Biology* **45**(4), 983.

Sievinen, J., Ulmer, W., Kaissl, W. *et al.* [2005], 'Aaa photon dose calculation model in eclipse', *Palo Alto (CA): Varian Medical Systems* **118**, 2894.

Sontag, M. R. [1977], 'Corrections to absorbed dose calculations for tissue inhomogeneities', *Medical Physics* **4**(5), 431.

Stathakis, S., Esquivel, C., Quino, L. V., Myers, P., Calvo, O., Mavroidis, P., Gutiérrez, A. N. and Papanikolaou, N. [2012], 'Accuracy of the Small Field Dosimetry Using the Acuros XB Dose Calculation Algorithm within and beyond Heterogeneous Media for 6 MV Photon Beams', *International Journal of Medical Physics, Clinical Engineering and Radiation Oncology* **01**(03), 78–87.

Tsuruta, Y., Nakata, M., Nakamura, M., Matsuo, Y., Higashimura, K., Monzen, H., Mizowaki, T. and Hiraoka, M. [2014], 'Dosimetric comparison of Acuros XB, AAA, and XVMC in stereotactic body radiotherapy for lung cancer', *Medical Physics* **41**(8), 081715.

Van Dyk, J. [1999], *The modern technology of radiation oncology: a compendium for medical physicists and radiation oncologists*, Medical Physics Pub, Madison, Wis.

Varian [2014], 'Using Varian Photon Beam Source Model for Dose Calculation of small fields'.

Varian [2015], 'Eclipse photon and electron algorithms reference guide'.

Vassiliev, O. N., Wareing, T. A., McGhee, J., Failla, G., Salehpour, M. R. and Mourtada, F. [2010], 'Validation of a new grid-based Boltzmann equation solver for dose calculation in radiotherapy with photon beams', *Physics in Medicine and Biology* **55**(3), 581–598.

Vatnitsky, S. M. and International Atomic Energy Agency [2008], *Commissioning of radiotherapy treatment planning systems: testing for typical external beam treatment techniques : report of the Coordinated Research Project on Development of Procedures for Quality Assurance of Dosimetry Calculations in Radiotherapy.*, International Atomic Energy Agency, Vienna. OCLC: 233540719.

Walters, B., Kawrakow, I., Rogers, D. W. O. and others [2005], 'DOSXYZnrc users manual', *NRC Report PIRS* **794**.

Young, M. E. J. and Gaylord, J. D. [1970], 'Experimental tests of corrections for tissue inhomogeneities in radiotherapy', *The British Journal of Radiology* **43**(509), 349–355.